Ore Geology Reviews 142 (2022) 104736

Contents lists available at ScienceDirect

Ore Geology Reviews

journal homepage: www.elsevier.com/locate/oregeorev

New insights on the Escoural Orogenic gold district (Ossa-Morena Zone, SW Iberia): Geochemistry, fluid inclusions and stable isotope constraints from the Monfurado gold prospect

Miguel Maia [a,b,*], José Roseiro [a,b], Pedro Nogueira [a,b], Fernando Noronha [c,d], Mercedes Fuertes-Fuente [f], Antonia Cepedal [f], José Mirão [a,e]

[a] Departamento de Geociências, Escola de Ciências e Tecnologias da Universidade de Évora, Rua Romão Ramalho 59, 7000-761 Évora, Portugal
[b] Instituto de Ciências da Terra (ICT), Polo da Universidade de Évora, Rua Romão Ramalho 59, 7000-761 Évora, Portugal
[c] Departamento de Geociências, Ambiente e Ordenamento de Território, Faculdade de Ciências da Universidade do Porto, Rua do Campo Alegre 687, 4169-007 Porto, Portugal
[d] Instituto de Ciências da Terra (ICT), Pólo da Universidade do Porto, Rua do Campo Alegre 687, 4169-007 Porto, Portugal
[e] Laboratório HERCULES, Largo Marquês de Marialva 8, 7000-809 Évora, Portugal
[f] Departamento de Geología, Universidad de Oviedo, c/ Jesús Arias de Velasco s/n, 33005 Oviedo, Spain

ARTICLE INFO

Keywords:
Orogenic gold
Vectoring gold exploration
Sulfide geochemistry
Fluid-rock interactions
SW Iberian Massif

ABSTRACT

The Escoural gold district belongs to the Montemor-Ficalho metallogenic belt which is part of the Portuguese section of Ossa-Morena Zone (OMZ), at the SW of Iberia. The Escoural gold district includes twelve gold prospects and/or deposits largely controlled by the NW-SE Montemor-o-Novo Shear Zone (MNSZ) and associated fault zones, extending for approximately 30 km. Ubiquitously, gold-arsenopyrite-loellingite assemblages hosted in quartz-sericite-chlorite veins are found in most deposits, although, in the Monfurado prospect, the gold-bearing assemblages are more complex. This prospect is located in the vicinity of a Cambrian SEDEX-VMS iron deposit, from which massive and disseminated iron-ores hosted in marbles and calcsilicate rocks, were exploited. The interplay of the gold mineralizing processes with the iron-rich host rocks has favored gold deposition at the Monfurado prospect. Selected samples from six drill cores allowed to define two mineralizing events: the pre-ore and ore stages. Two types of gold mineralization characterize the ore-stage: i) massive sulfide horizons in which gold (Au = 85.6–86.3 wt%; Ag = 13.1–13.6 wt%) is hosted in arsenopyrite and pyrite or, seldomly, gold particles (Au = 91.8 wt%; Ag = 7.1 wt%) found in an arsenopyrite-rich layer; and ii) quartz-chlorite-pyrite veins crosscutting acid metavolcanic rocks with rhyolite-rhyodacite affinities, in which gold (Au = 80.5–82.9 wt%; Ag = 16.8–18.7 wt%) is found as fracture filling in pyrite, sometimes accompanied by Bi-Te phases. Arsenopyrite geothermometer suggests that for type i the overall deposition temperature falls within the range of 188 °C to 372 °C. Type ii mineralization lacks arsenopyrite, and for this reason, thermodynamic constraints were gathered from fluid inclusions and chlorite geothermometer. CH_4-rich fluid inclusions are ubiquitous in transgranular fluid inclusion planes, suggesting that reduced fluids percolated the rocks that host type ii mineralization. The reduced fluids support the transport of gold in sulfide complexes, such as $AuHS^-$ and $Au(HS)^-_2$. Furthermore, secondary H_2O-NaCl fluid inclusions (Lw_2) were found, with mean salinities of 6.0 eq. w (NaCl) and mean homogenization temperature of 226 °C, with corresponding pressures of 3.0 MPa, thus suggesting late hydrostatic regimes. Chlorite geothermometer results are in the range of 229 °C and 309 °C, agreeing with the fluid inclusion homogenization temperatures for Lw_2 fluids.

Sulfur isotope ($\delta^{34}S$) analysis of representative sulfide phases collected from both mineralization types, revealed signatures ranging from 8.5 ‰ and 10.6 ‰, indicating a single sulfur source. The gathered results suggest that although fluid transport is structurally controlled by MNSZ activity, the sulfidation reactions promoted by fluid-rock interactions are the main control on gold deposition from type i mineralization. It is further suggested that a coeval gold-event can lead to the deposition of two different types of mineralization, related to distinct gold deposition mechanisms.

* Corresponding author at: Departamento de Geociências, Escola de Ciências e Tecnologias da Universidade de Évora, Rua Romão Ramalho 59, 7000-761 Évora, Portugal.
E-mail address: mcmaia@uevora.pt (M. Maia).

https://doi.org/10.1016/j.oregeorev.2022.104736
Received 8 September 2021; Received in revised form 6 December 2021; Accepted 29 January 2022
Available online 3 February 2022

The tectonic and geodynamic settings in which the Escoural gold district developed correlate it to worldwide Palaeozoic orogenic gold deposits, with the Monfurado prospect being an example of the complexity of such geological settings.

1. Introduction

The characterization of orogenic gold deposits and the identification of suitable vectoring tools to locate the most favorable locations for ore deposition, are challenging tasks for gold exploration projects. Their success depends on the significant understanding of the geodynamic and metallogenic settings that control the genesis of such deposits, as well as, clearly identifying the mineralization style. Such knowledge is highly reliable on the current accepted orogenic gold models but comparing such models to local field exploration data is extremely challenging and may sometimes lead to demotivating results.

The diverse ore-emplacement mechanisms described for this kind of deposit depends on factors such as time (geological age) and space (geological settings). Although, the collection of multidisciplinary data from orogenic gold deposits can ultimately allow the definition of successful exploration vectors.

We focus our research on developing an approach that can beneficiate gold exploration in SW Iberia, targeting the mechanisms behind gold transport and deposition, and the structural controls in the Escoural gold district.

The above-mentioned time and space dilemma generate prolific discussions and a fair amount of uncertainty regarding the conditions in which orogenic gold deposits form (Goldfarb and Groves, 2015; Wyman et al., 2016; and Gaboury, 2019). However, many physical and chemical conditions are shared by different orogenic gold deposits, such as the involvement of metamorphic fluids in gold transport, in relatively reduced conditions, and driven by regionally expressive crustal anisotropies. It is generally accepted that gold is transported in $AuHS^{-}$ and $Au(HS)^{-}_{2}$ complexes, and therefore sulfur activity in the system plays a major role in controlling the transport-deposition mechanisms (Lindgren, 1907, 1933; Goldfarb et al., 2005; Phillips and Powell, 2010; Goldfarb and Groves, 2015).

The separation of gold from the sulfur compounds can be promoted by the oxidation of the transporting fluid (Hodkiewicz et al., 2009; LaFlamme et al., 2018a, 2018b). Hence, comprehending the geochemical conditions that could trigger oxidation is of uttermost importance for understanding the mechanisms that lead to gold accumulation. Several authors have identified a fair amount of processes that contribute to the fluid oxidation, such as i) fluid mixing from different sources (Uemoto et al., 2002; Bateman and Hagemann, 2004; Melfos et al., 2019); ii) cyclic fracturing causing pressure fluctuations in the fluid (Sibson et al., 1975; Hodkiewicz et al., 2009; Peterson and Mavrogenes, 2014; Voisey et al. 2020); iii) fluid-rock interactions, such as, carbonation and sulfidation (Phillips, 1986; Phillips and Hughes, 1996; Palin and Xu 2000; Goldfarb et al., 2005; Goldfarb and Groves, 2015; Petrella et al., 2020) or even iv) devolatilization by metamorphic fluids as discussed by Phillips and Powell (2010).

Several gold deposits with genetic links to large shear zones are found throughout the Iberian Massif. Such deposits developed in the late stages of collisional event of the Variscan orogeny, in both orogenic and intrusion-related systems (e.g. Cepedal et al., 2013, 2018; D'Angelico et al., 2016; de Oliveira et al., 2007; Fuertes-Fuentes et al., 2016; MacKenzie et al., 2019; Martinez-Abad et al., 2015; Neiva et al., 2019; Noronha et al., 2000; Ribeiro et al., 1993; Rodríguez-Terente et al., 2018; Vallance et al., 2003; Mortensen et al., 2014; Leal et al., 2022). In the north of Portugal, these deposits are found hosted in metasedimentary sequences (e.g. Tresminas or Valongo areas) and granitic units (e.g. the Penedono, Grovelas, or Castromil deposits), spatially associated with Variscan shear ductile–brittle structures. In such deposits the nature of the mineralizing hydrothermal solutions was identified as related with metamorphic fluids, displaying variable contribution of meteoric water to the system but without a recognizable input of magmatic fluids. Additionally, host rocks were identified as being the main source of metals and ligands to the mineralizing system, and the pronounced tectonism and associated structures, mostly shear zones and faults, served as pathways for fluid circulation (e.g. Noronha et al., 2000; Vallance et al., 2003; D'Angelico et al., 2016). Despite the extended time–space distribution, diverse metal sources, and the variety of ore-forming fluids, these deposits exhibit similarities, such as i) evidence of successive shearing with recurrent reactivation, ii) geodynamic settings that contributed to complex polyphasic fluid percolation; and iii) a typical gold-arsenopyrite ore-stage assemblage (e.g. Noronha et al., 2000; Fuertes-Fuentes et al., 2016).

Gold deposits located on northern Iberia have been recently targeted for numerous multidisciplinary studies (Cepedal et al., 2013, 2018; D'Angelico et al., 2016; Fuertes-Fuentes et al., 2016; MacKenzie et al., 2019; Martinez-Abad et al., 2015; Neiva et al., 2019; Noronha et al., 2000; Rodríguez-Terente et al., 2018; Vallance et al., 2003; Mortensen et al., 2014; Leal et al., 2022). On the contrary, at the SW of the Iberian Massif, particularly in Ossa-Morena Zone (OMZ), the characterization of gold deposits is not so well constrained. In this region, gold mineralization appears to be restricted to large Variscan shear zones with strike-slip kinematics. These geological settings are found at the São Martinho and Mosteiros deposits (De Oliveira et al., 2007) and at the numerous deposits and occurrences of the Escoural gold district, which are mainly hosted in Neoproterozoic to Lower Cambrian metasedimentary and metavolcanic units.

Because of this, identify and understand the mechanisms that promoted the gold precipitation is the main objective of this research, aiming to contribute to the comprehension of the Escoural gold district.

Herein a comprehensive study of the Monfurado gold prospect, part of the puzzling Escoural gold district, is provided. A wide range of techniques, including, mineralogical, geochemical, sulfur isotope, and fluid inclusion studies were employed, thus allowing to infer the sources of metals, fluid pathways, and fluid-rock interactions capable of triggering the mechanisms responsible for the anomalous gold concentrations in the area.

2. Geological settings

2.1. Geodynamic context of Iberia

The Iberian Massif represents the westernmost section of the European Variscides, and comprises a set of geological units formed during Palaeozoic that can be described in three different stages: i) the Cambrian-Early Ordovician rift stage, responsible for the separation of the Avalonia terrane at the northern Gondwana margin, forming the Rheic Ocean; ii) the Ordovician – Devonian passive margin stage, and iii) the middle-Devonian to Carboniferous subduction and posterior Gondwana-Laurussia oblique collision resulting in the closure of the Rheic Ocean and edification of Pangea (e.g. Franke, 2000; 2014 Matte, 2001; Nance et al., 2010; 2012; Pereira et al., 2012; Pereira et al., 2017; Franke et al., 2017; Kroner et al., 2020).

The Cambrian-Early Ordovician rift stage at the northern Gondwana margin promoted the formation of several sedimentary basins in horst-graben structures, together with bimodal volcanic activity, which is well expressed throughout Iberia. The earlier expressions of rift-related volcanism are mainly restricted to the near-axis region in the southern domains, and late-stage assemblages are found widespread throughout the Iberian Massif (Chichorro et al., 2008; Sánchez-García et al., 2008;

Sánchez-Garcia et al., 2010; Sánchez-García et al., 2014; Sánchez-García et al., 2019, and references therein; Castro et al., 2020). The rift stage ended with the complete detachment of Avalonia, which drifted away from northern Gondwana, and gave birth to the Rheic Ocean during the Early Ordovician ages (ca 480 Ma; Pedro et al., 2010; Ribeiro et al., 2010). The Early Ordovician rift-drift transition set Iberia into a wide passive margin stage that persisted until Lower Devonian (e.g. Dias et al., 2016; Gutiérrez-Marco et al., 2019).

The subsequent compressional stage begins with an accretion and subduction period followed by the transcurrent collisional episode that presumably occurred before Visean times (Dallmeyer et al., 1993; Jesus et al., 2007; Jesus et al., 2016; Pin et al., 2008; Pereira et al., 2012). This period is characterized by i) extreme tectonism near the Avalonia-Gondwana suture zone; ii) orogenic metamorphism with considerable variations of the P-T regime; iii) the emplacement of parautocthonous and allochthonous terranes in the inner autochthon domains of the Iberian Massif, namely obduction of ophiolite fractions with the exhumation of high-pressure units, and iv) subduction and syn-collision magmatism (e.g. Quesada et al., 1994; Quesada et al., 2019; Pedro, 1996; 2004; Pedro et al., 2010; Fonseca et al., 1999; Leal, 2001; Dias et al., 2002; Araújo et al., 2005; Valle Aguado et al., 2005; Moita et al., 2005a; Ribeiro et al., 2007; 2010; Jesus et al., 2007; Jesus et al., 2016; Rosas et al., 2008; Moita et al., 2009; Rubio Pascual et al., 2013; Dias et al., 2016; Azor et al., 2019).

Three main stages of deformation characterize the Variscan orogen, starting with D_1 which correspond to subduction-related crustal thickening as a result of thrust sheet stockpiling and recumbent or overturned folds that affect all units before Devonian ages; D_2 characterized by decompression and/or orogenic collapse and extension, and D_3 correspondent to a post-collisional thickening stage, implying vertical folds, ductile shears and strike-slip faults (Azor et al., 2019 and references therein).

2.2. Ossa-Morena Zone

The variety of tectonic-metamorphic and magmatic events that affected the Iberian Massif during the Variscan Cycle is expressed by a well-defined tectono-stratigraphic zonation (Lotze, 1945; Julivert et al., 1972; Ribeiro et al., 1995; 2007; Murphy et al., 2016; Simancas, 2019). In SW Iberia, the Rheic suture zone divides two important tectonic-stratigraphic units: the Ossa-Morena Zone, which represents the northernmost autochthonous terrane of Gondwana, and the South Portuguese Zone (SPZ), interpreted to embody a remnant of Avalonia separated in Cambrian - Early Ordovician times and posteriorly accreted during the collisional stages of the Variscan orogeny.

The OMZ comprises a thick sequence of variably metamorphosed rocks with ages ranging from Neoproterozoic to Carboniferous, packed with debris presumably resulting from the dismantlement of a pre-existing Cadomian arc (Apalategui et al., 1990; Oliveira et al., 1991; Araújo et al., 2013). The base sequence is characterized by the Lower Cambrian basal conglomerate and a calcite-dolomite carbonate formation, discordantly settled on top of the Neoproterozoic metasedimentary basement (locally named *Série Negra*), followed by a succession of siliciclastic strata culminated by syn-orogenic flysch, deposited from Middle-Upper Devonian to Lower Carboniferous (Oliveira et al., 1991; Piçarra, 2000; Robardet and Gutiérrez-Marco, 2004; Borrego, 2009; Gutiérrez-Marco et al., 2019). The Cambrian-Early Ordovician rift events are accompanied by the emplacement of a series of acid-intermediate and basic volcanic rocks intercalated in the carbonate and detrital units of Lower-Middle Cambrian age (Chichorro et al., 2008; Sánchez-García et al., 2008; Sánchez-Garcia et al., 2010; Sánchez-García et al., 2014; Sánchez-García et al., 2019).

The subduction and collisional episodes promoted the thrusting of ophiolitic and bordering units of the Iberian Terrane to the inner domains of the OMZ, as well as the exhumation of high-pressure rocks (e.g. the Moura Phyllonitic Complex; Araújo et al., 2005; Moita et al., 2005a; Rosas et al., 2008; Pedro et al, 2010; Ribeiro et al., 2010), and the emplacement of the Pulo do Lobo Terrane, an accretionary wedge overlaying the SPZ (e.g. Quesada et al., 1994). Additionally, several bimodal igneous suites were installed in the OMZ during different stages of the collisional event (Pereira et al., 2003; Pereira et al., 2007; Pereira et al., 2008; Jesus et al., 2007; Jesus et al., 2016; Moita et al., 2005b; Moita et al., 2009; Dias da Silva et al. 2018; Ribeiro et al. 2019). The Variscan tectonic-metamorphic and magmatic events kept high-thermal regional regimes in Iberia and promoted the circulation of magmatic, metamorphic, and hydrothermal fluids responsible for the generation of some of the ore deposits widespread throughout OMZ.

2.3. The Montemor-o-Novo - Ficalho metallogenic belt

The Montemor-o-Novo – Ficalho metallogenic belt (Mateus et al., 2013; Tornos et al., 2004) is part of the Montemor-Ficalho lithostratigraphic Sector (Oliveira et al., 1991) delimited at North by the Estremoz-Barrancos Sector and at South by the Beja Igneous Complex. This belt displays an extremely complex evolution, evidenced by its structural, geological, and metallogenic features. The commodities are diverse, including Fe, Cu, Pb, Zn, and Au, and are represented by several ore assemblages hosted in diverse geological settings. Hence, several models are invoked to explain their occurrence, such as the SEDEX-VMS iron ores (Montemor-o-Novo iron deposits; Salgueiro, 2011); Zn-Pb deposits (Preguiça-Vila Ruiva and Enfermarias deposits; Barroso et al., 2003; Martins et al., 2003), or Skarn deposits (Orada, Azenhas, and Alvito Fe deposits; Carvalho, 1971, Oliveira, 1986; Matos et al., 1998, Caldeira et al., 2007; Salgueiro et al., 2010a, Salgueiro et al., 2010b; Mateus et al., 2005; Mateus et al., 2013; Maia et al., 2022).

Throughout the 18th and early 19th century this area was an important mining district with operations focusing on eight iron ore bodies (Andrade et al., 1949). The deposits are mainly composed of massive magnetite-pyrite (±chalcopyrite) and are hosted in Cambrian-Lower Ordovician units, for which recent studies suggest a Cambrian SEDEX-VMS continuum model (Salgueiro, 2011).

Aside from the iron ores found in the Montemor-o-Novo area, several gold deposits have been targeted during the last decades, forming what is here described as the Escoural gold district. This district was the focus of several gold-exploration projects and scientific research, providing first descriptions of the gold endowment in the Escoural gold district deposits (Ribeiro et al., 1993). These earlier studies presented the first proposal that classified the deposits as Orogenic gold (Inverno, 2001). More recently, Lopes (2015) and Lopes et al. (2015) provided petrographic and isotopic (Sr-Nd) studies of host lithologies.

The calculated resources for the Escoural gold district reached 4.45 million tons of ore with a mean gold grade of 2.81 g/ton, translating into 440 000 oz/12.5 tons of Au (Faria et al., 1997; Mateus et al., 2013; Lopes, 2015 and references therein), in which 45% are inferred mineral resources, 46% indicated and 9% measured. Previous authors tried to frame the ore deposition conditions, emphasizing on the sedimentary, structural, and geochemistry settings, whereas a multi-technique approach to the ores, as the one herein proposed, has never been endeavored.

2.4. Escoural gold district

The Escoural gold district is part of the Évora Massif, which is subdivided into three units: i) the high-grade metamorphic terrains, ii) the Montemor-o-Novo Shear Zone and iii) the Évora mid-grade metamorphic terrains (Pereira et al., 2003; Pereira et al., 2006; Chichorro, 2006; Moita et al., 2009).

This gold district is structurally controlled by the wide (2–10 km) ductile NW-SE upper Carboniferous Montemor-o-Novo Shear Zone (MNSZ), which extends for over 30 km and hosts 12 known deposits (Fig. 1**a**). Greenschist to amphibolitic facies metamorphism is ubiquitous in the area (Fig. 1**b**), and deformation is outlined by intense

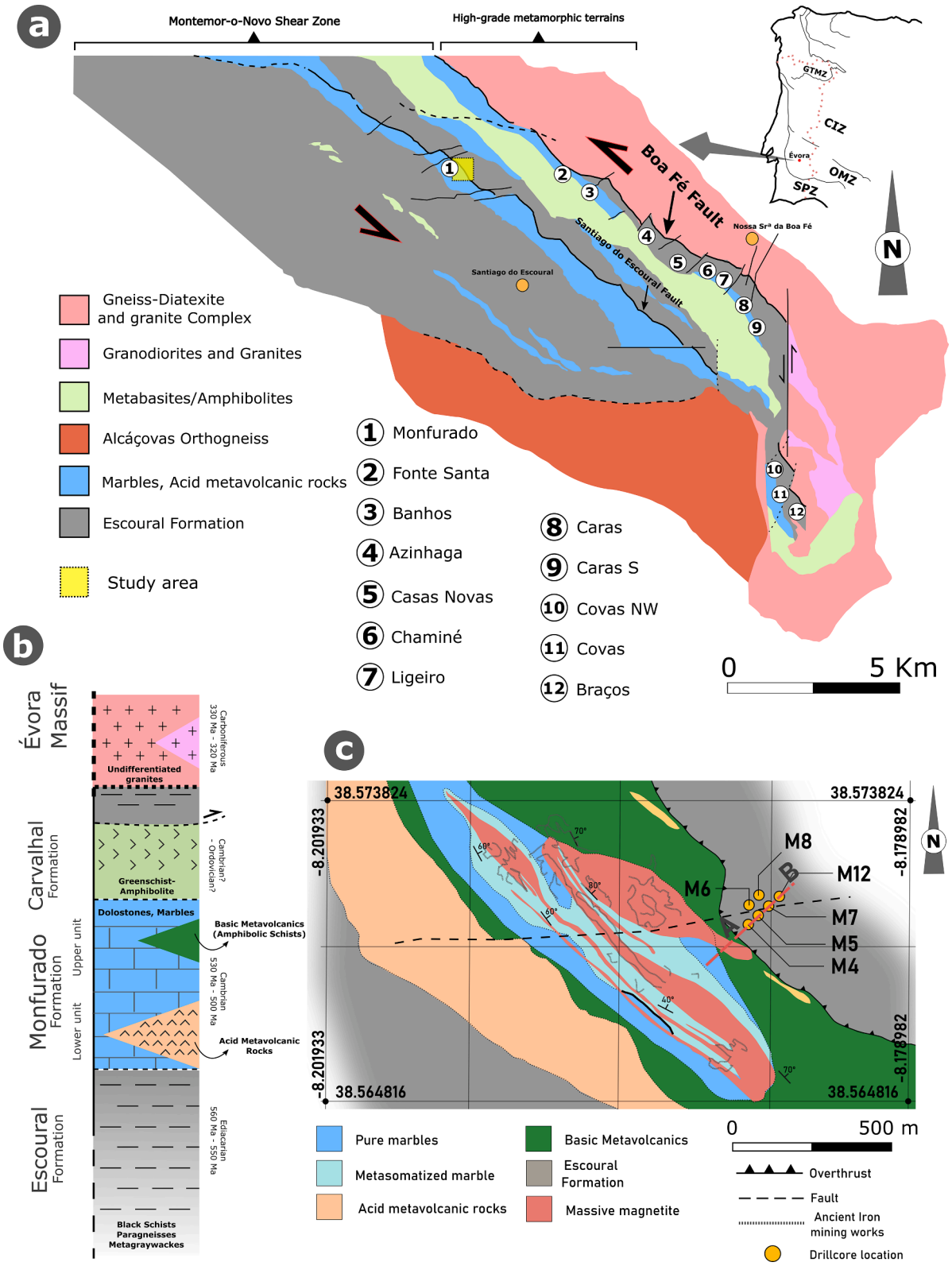

Fig. 1. **a.** Location of the study area in the Iberian terrane and geological map of the Montemor-o-Novo area (adapted from Chichorro, 2006), with representation of the main geological formations. The numbered circles (1–12) represent the twelve gold prospects of the Escoural Gold district. The Monfurado prospect area is marked in the regional map by the yellow rectangle. The orange circles represent the closest villages to the deposits, the *Santiago do Escoural* and *Nossa Senhora da Boa Fé*. **b.** Stratigraphic chart representative of the main formations observed in the Montemor-o-Novo and Santiago do Escoural areas (adapted from Carvalhosa and Zbyszewski, 1994; Chichorro, 2006). **c.** Geological map of the Monfurado prospect area (adapted from Andrade et al., 1949; Serviço de Fomento Mineiro, 1977), with location of the sampled drill cores performed in the vicinity of the ancient Monges iron mine. The A-B profile (red dashed line) corresponds to the geological section from drill cores M4 to M12 presented in Fig. 3.

mylonitization that allowed to constrain the ages through which MNSZ was active (356 – 322 Ma; Pereira et al., 2015 and references therein). Most of the gold prospects (2–12 in Fig. 1**a**) occur near the contact between the MNSZ and the high-grade metamorphic terrains, structurally controlled by the Boa Fé fault zone (Fig. 1**a**), with exception of the Monfurado gold prospect which is located in the vicinity of the Santiago do Escoural fault. The units affected by the MNSZ can be defined as follow:

1. Escoural Fm. (Neoproterozoic): A metasedimentary formation, locally designated as *Série Negra*, mainly composed of biotitic schists and quartz-feldspar paragneiss, resulting from the dismantlement of a Cadomian-Avalonian magmatic arc with ages ranging from 560 to 550 Ma (Chichorro, 2006).
2. Monfurado Fm. (Lower Cambrian): This formation is individualized in two units (Chichorro, 2006), adopted subsequently by other authors (e.g. Salgueiro, 2011). The Lower unit is characterized by acid volcanism that is emplaced in the calcite-dolomite carbonate formations during the rift-related volcanic events (522.3 ± 5 Ma; Chichorro et al., 2008), with metamorphism and deformation superimposed during the Variscan orogeny. The acid metavolcanics are locally referred to as Escoural Leptinites and display affinities to rhyodacites and rhyolites (Sánchez-García et al., 2003; Sánchez-García et al., 2019, Chichorro, 2006). The Upper unit corresponds to the transition to an intermediate/basic volcanism, composed of amphibolites and amphibolic schists.
3. Carvalhal Fm. (Middle–Upper Cambrian): Mainly composed of basic metavolcanic rocks affected by greenschist to amphibole facies metamorphism and strongly deformed by the MNSZ activity. The Carvalhal Fm. is divided into two units, a Lower unit in which amphibolites (E-MORB) predominate, with intercalations of calcsilicate rocks (Carvalhosa, 1983; Carvalhosa and Zbyszewski, 1994) and an Upper unit composed of phyllites and metabasites with N-MORB signatures.

2.4.1. *The Monfurado gold prospect*

The Monfurado prospect is located at the NW of the Escoural gold district (Fig. 1**a**) and was one of the twelve targeted areas for mineral exploration. The Monfurado prospect is found near the ancient Monges iron mine (Fig. 1**c**; Andrade et al., 1949), north of the Santiago do Escoural village and mainly hosted by two geological units: the Escoural Fm. and Monfurado Fm (Lower and Upper units), described above (Fig. 1).

A drilling campaign (11 drill holes) was performed in 2012 by the COLT Resources exploration company to assess the Monfurado gold prospect potential. Outcrops are scarce, and the area is covered by a thin regolith. Therefore, the log interpretation provided by the company and later reinterpreted for this work, was essential to identify the main geological and structural controls over gold mineralization.

Drill core logs show a monocline structure generally dipping towards NE. The Escoural Fm. is found at the top of the logs (Fig. 2**;** Fig. 3), and it is differentiated by paragneisses and thin amphibolic schist intercalations. The contact between the Escoural Fm. and the Monfurado Fm. units is marked by tectonism that is interpreted as an overthrust (Araújo, 1995). The Upper unit of the Monfurado Fm. is composed by amphibolic schists (basic metavolcanic unit; Fig. 1**b, c;** Fig. 2) usually interbedded with pristine marbles. This unit transits to calcite-dolomite carbonated lithotypes at depth, ranging from pure marbles to calcsilicate metasomatized rocks. The transition to the acid metavolcanic rocks is marked by an abrupt contact and is evidenced by the presence of orthogneisses and sparse metacherts. The acid metavolcanic rocks are intensely fractured with several generations of veins, although two main types are consistent throughout the studied drill core samples and can be divided in i) thin quartz + tourmaline veins (<1–2 cm) perpendicular to

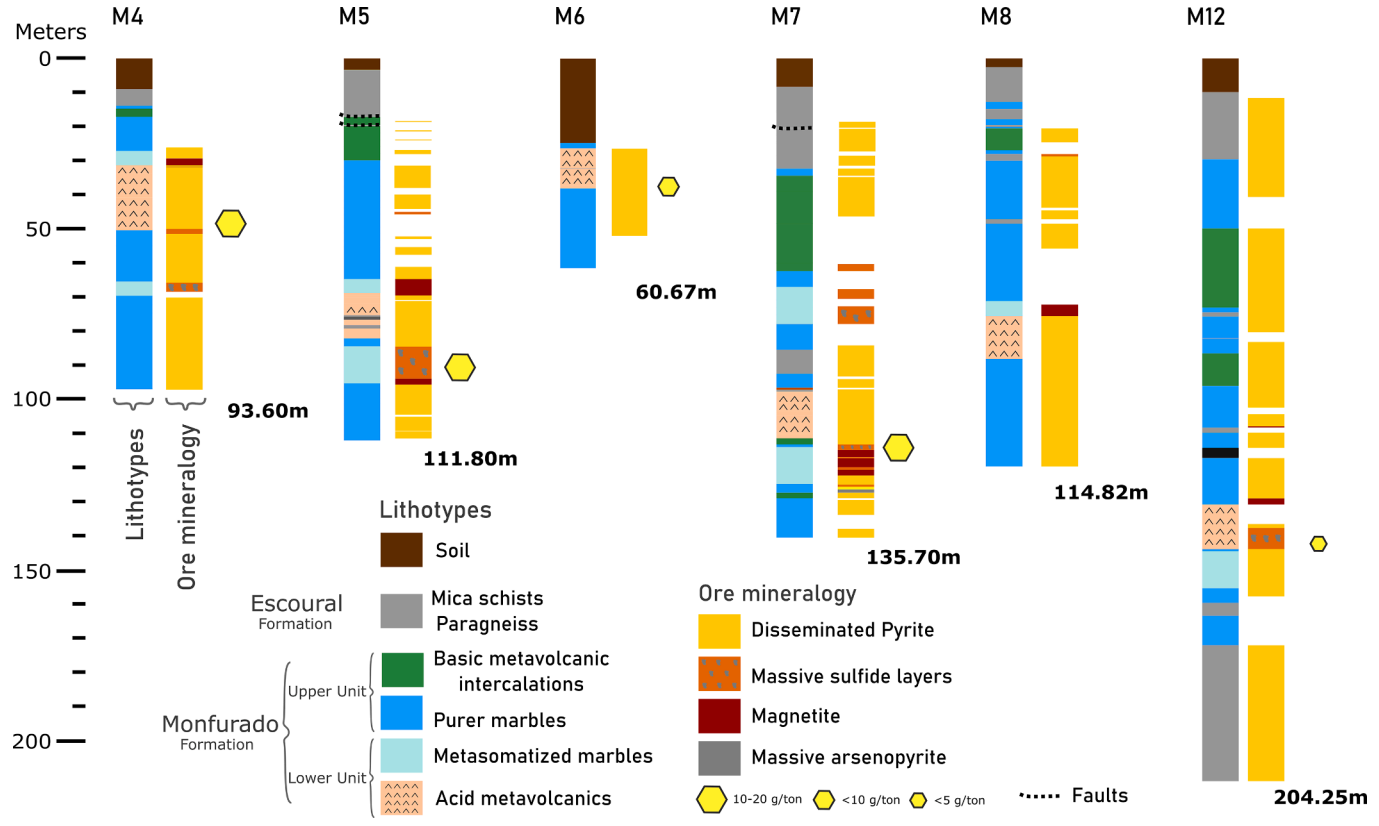

Fig. 2. Log representation of the six studied drill cores, with individualization between lithology and ores. The yellow hexagons on the side of the drill cores refer to the range of the highest reported punctual gold grades (g/ton) on the respective drill core.

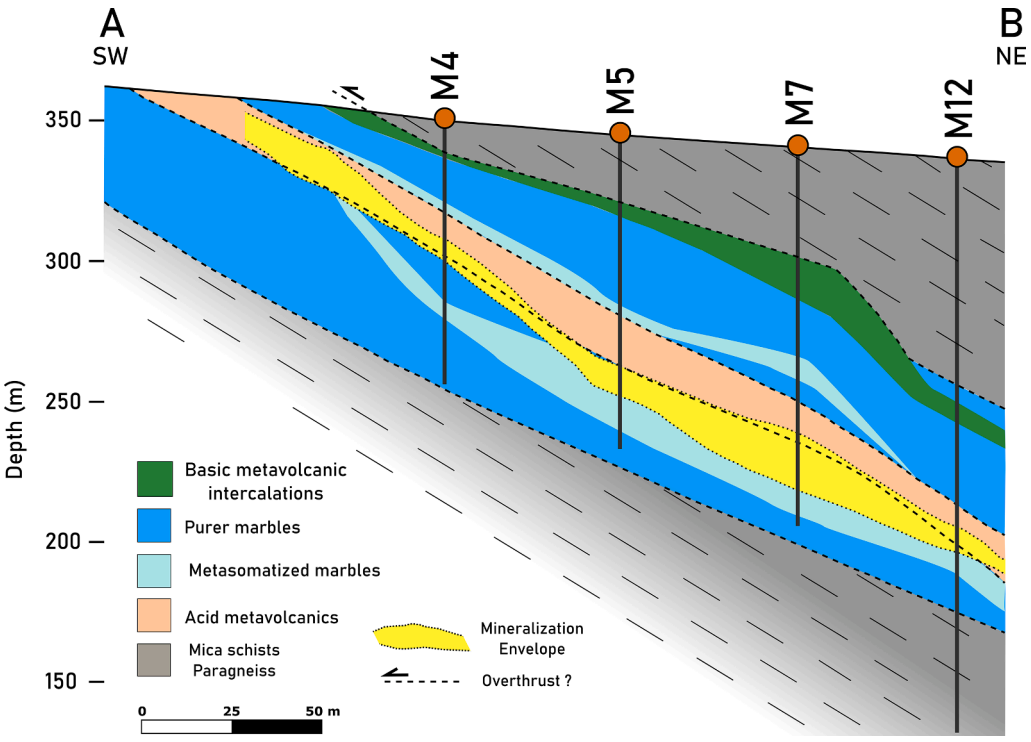

Fig. 3. Interpretative section (adapted from COLT Resources unpublished reports) of four of the six studied drill cores in a SW-NE profile from M4 to M12 drill cores, as displayed by the A-B profile marked in Fig. 1c. The mineralized envelope refers to gold grades above 0.2 g/ton.

bedding with sections of high density (4 veins/meter), and ii) sparse thicker quartz-feldspar-chlorite veins (up to 5 cm) parallel to bedding cross-cutting the latter veins.

In some of the deeper sections of the cores, another transition to the Monfurado Fm. is observed hosting the richer ore sections (c.f. Fig. 2), mainly composed of massive sulfide layers with pyrrhotite and disseminated arsenopyrite. The Monfurado Fm. is identified as an important fluid pathway due to its intense mineralization, represented by massive layers of sulfides mainly composed of pyrrhotite, pyrite and arsenopyrite in which the higher gold grades are found. The massive sulfide layers are hosted in a carbonate iron-rich unit, in sections immediately below the acid metavolcanic rocks (Fig. 2).

Massive magnetite sections are observed throughout the drill cores, and pyrite is ubiquitous in all lithologies, mostly found in a disseminated form but locally occurring as massive layers.

The geochemical analysis of continuous log sections of 1 m length, provided by COLT Resources company shows that the distribution of gold grades is controlled by i) the presence of massive sulfide layers with disseminated arsenopyrite hosted in calcsilicate units, ii) quartz-chlorite-pyrite veins that crosscut the acid metavolcanic rocks. Interesting gold grades along the drill cores are shown in Fig. 2, and the mineralized envelope is defined in Fig. 3.

3. Sampling and analytical methods

3.1. Sampling

A total of 133 samples were collected at different depths from six of the eleven drill cores (M4; M5; M6; M7; M8; M12; Fig. 1**c**; Fig. 2) and are representative of the host rock lithologies and main mineralized sections. Sampling also focused on altered host rocks to identify the extent of alteration related with the mineralizing event, as well as with the regional metamorphism. The sampling resulted in the preparation of 143 polished thin sections and 62 polished cross-sections for petrographic and mineralogical studies, 8 milled samples for whole-rock geochemistry, 15 double polished thick sections for the fluid inclusion study, and 11 sulfide concentrates for sulfur isotope geochemistry.

3.2. Optical and scanning electron microscopy

Polished cross-sections and polished thin sections were observed under an optical microscope to identify the main mineral phases and establish the ore paragenesis. Scanning electron microscopy with energy dispersive spectroscopy (SEM-EDS) analysis and image acquisition were performed using a VP-SEM-EDS Hitachi S3700N with a Bruker Xflash 5010SDD X-ray spectrometer at the HERCULES Laboratory of the University of Évora -Portugal-, and an MEB JEOL-6100 SEM-EDS at the Technical and Scientific Services of the University of Oviedo - Spain. All the mineralogical abbreviations adopted through this manuscript follow the proposals from Whitney and Evans (2010).

3.3. Electron probe microanalysis (EPMA)

In-situ arsenopyrite, pyrite, gold, chlorite, tourmaline, and feldspar analysis were performed using a CAMECA SX100 electron probe microanalyzer (EPMA) at the Technical and Scientific Services of the University of Oviedo (Spain). The analytical conditions were selected as follows: i) for arsenopyrite and pyrite a ~ 5 μm beam diameter was used, with an acceleration voltage of 20 kV and a 20 nA current for As, S, and Fe quantification, and a 20 kV acceleration voltage and 100nA current was used for Au quantification; ii) for gold particle analysis a ~ 5 μm beam was used to analyze the larger Au grains with an acceleration voltage of 20 kV and a current of 20 nA, and iii) for silicates and acceleration voltage of 15 kV and a 15 nA current was used.

The standards used for S, As, Fe were arsenopyrite, for Au, Cu, Se, Fe, Bi, Ag, and Hg the standards were pure gold, pure copper, pure selenium, pure iron, pure bismuth, silver telluride, and mercury sulfide respectively. All raw data including the limits of detection (LOD) for each element is disclosed in **Supplementary Material B**.

3.4. Fluid inclusion studies

Fluid inclusion (FI) studies were performed at the Geoscience Department of the University of Évora using a LINKAM THMSG600 microthermometry stage coupled to a Nikon Eclipse 50Ipol microscope with a 100x long focus objective lens. Microthermomety cooling runs were performed using a 1 °C to 10 °C/min rates to ensure a cooling that allows the observation of the different phase changes, such as the first CH_4 melting temperatures (Tm_{CH4}), CO_2 melting temperature (Tm_{CO2}), eutectic temperature (Te), and ice melting temperature (Tm_{ice}). The heating runs were performed using a 5 °C/min to 30 °C/min step heating, assuring the accuracy of measurements of ± 0.3 °C and allowing to register CO_2 homogenization temperatures (Th_{CO2}) and final homogenization temperatures (Th).

Fluid inclusion salinities were calculated using the Tm_{ice} (Bodnar and Vityk, 1994) and Tm_{chl} when CO_2 was present, and when correct observation of this phase transition was possible. To constrain the P-T-V-x conditions of the fluids in the H_2O-NaCl system, the AqSo_NaCl Software (Bakker, 2018) was used, and for the H_2O-CH_4 system, the BULK package was used (Bakker, 2003).

3.5. Sulfur isotope geochemistry

Samples for sulfur isotope analysis were separated under the

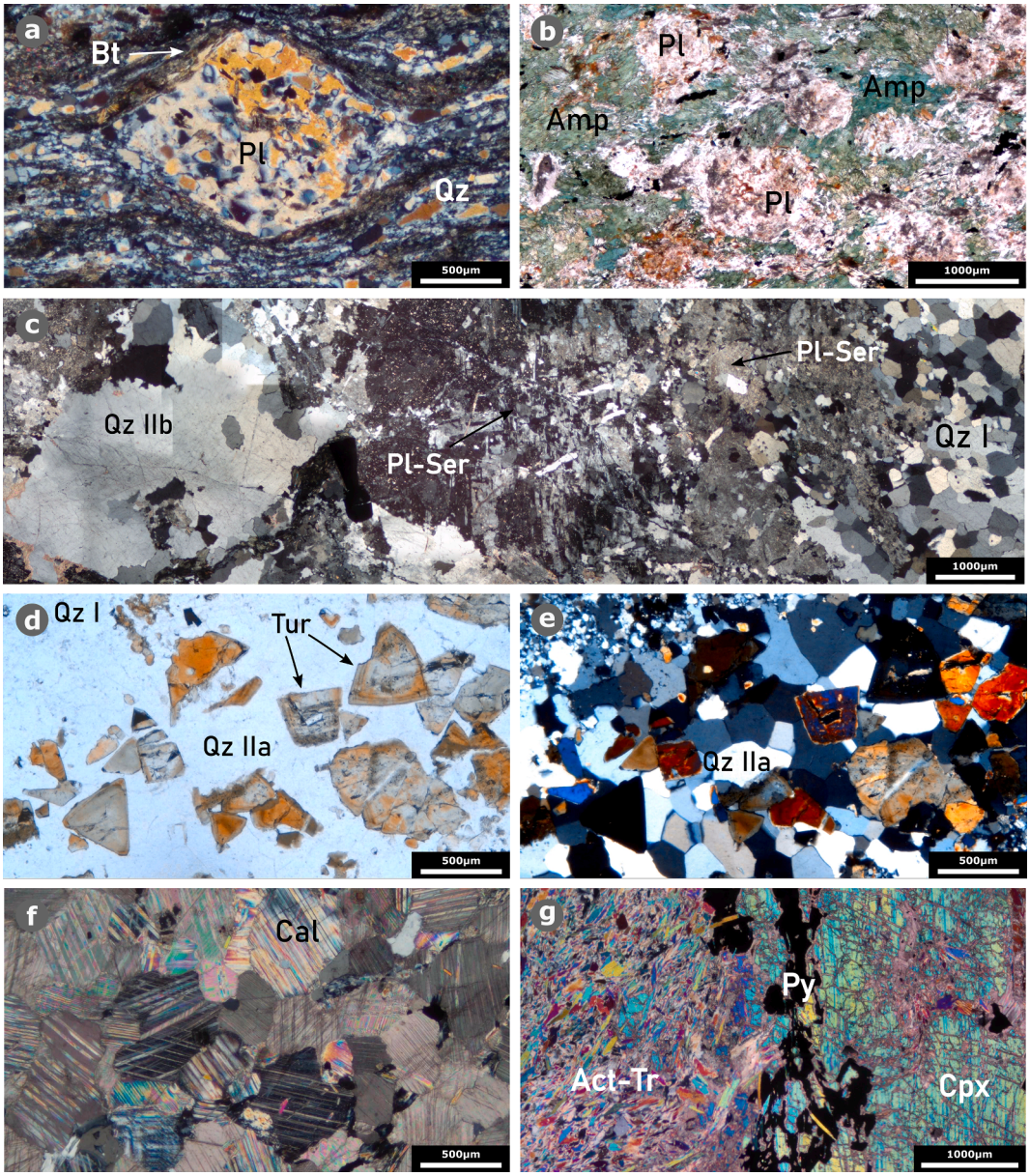

Fig. 4. Representative petrography of host-rock thin sections is shown from (a.) to (g.). **a.** Example of macroscopic scale structures of the Paragneiss from the Escoural Fm., in which deformation is outlined by large plagioclase porphyroclasts surrounded by aligned plates of biotite and quartz ribbon structures. **b.** Composite image of microphotographs at x2 magnification, exemplifying the textures and mineral paragenesis of the basic metavolcanics (amphibolite?) of the Monfurado Fm. with relics of oval plagioclase surrounded by green hornblende. **c.** Composite microphotograph (x2 magnification) of the acid metavolcanic rocks from the Lower unit of the Monfurado Fm. This thin section outlines the quartz-feldspar matrix, with large porphyroclasts of plagioclase intensely sericitized (Pl-Ser). The volcanic matrix is crosscut by late quartz veins (Qz IIb), with large anhedral crystals. **d.** Plane nicols composite microphotograph of the quartz (QzIIa)-tourmaline veins that crosscut the acid metavolcanics of the Monfurado Fm. **e.** Crossed nicols composite microphotograph of the section shown in (d.). **f.** Calcite-dolomite marbles of the Upper Monfurado Fm. unit. **g.** pervasive calcsilicate alteration of the marble units of the Monfurado Formation, with development of tremolite-actinolite and pyroxene paragenesis substituting the previous calcite-dolomite matrix.

microscope to ensure the representativeness of the mineralization assemblages.

The selected samples were crushed for the selection of mono-mineralic grains of arsenopyrite, pyrite, and pyrrhotite. Arsenopyrite and pyrite were hand-picked under a binocular stereomicroscope, whereas pyrrhotite was separated using a hand-magnet and then hand-picked. Sulfur isotope analysis was performed by obtaining SO_2 for the determination of the $^{34}S/^{32}S$ isotopic ratio by isotope ratio mass spectrometry at the NUCLEUS Laboratory, University of Salamanca - Spain.

Table 1
Representative major and trace elements data from drill core selected samples. Major elements in wt.%; trace elements in ppm.

Sample		1	2	3	4	5	6	7	8	9
	LOD*	M12@66 *m*	M8@80 *m*	M8@83 *m*	M6@28 *m*	Acid Metavolcanics (outcrop)	M10@76 *m*	M6@60 *m*	M12@95 *m*	M12@98 *m*
		Paragneiss	Acid Metavolcanics	Acid Metavolcanics	Acid Metavolcanics		Marble	Calcsilicate rock	Intermediate Metavolcanics	Basic Metavolcanics
wt. %										
SiO_2	0.01	70.5	76.4	72.6	73.3	75.3	3.56	6.88	60.8	49.1
Al_2O_3	0.01	12.8	13.55	12.85	13.2	13.75	0.08	1.51	16.75	14.3
Fe_2O_3	0.01	4.58	1.35	4.35	1.66	0.64	6.07	3.35	5.01	5.09
CaO	0.01	0.58	1.1	1.19	0.56	0.96	29.3	36.8	5.94	17.4
MgO	0.01	2.83	0.41	1.77	1.87	1.07	18.3	10.95	1.47	2.49
Na_2O	0.01	2.83	6.42	5.49	1.58	7.59	0.02	0.14	3.22	1.52
K_2O	0.01	0.86	0.55	0.6	5.77	0.17	0.01	0.35	4.08	2.81
Cr_2O_3	0.002	0.006	<0.002	0.003	0.002	0.006	<0.002	<0.002	0.011	0.011
TiO_2	0.01	0.39	0.22	0.41	0.29	0.48	<0.01	0.09	0.68	0.57
MnO	0.01	0.01	<0.01	0.02	0.01	0.02	0.52	0.41	0.07	0.12
P_2O_5	0.01	0.11	0.13	0.13	0.1	0.07	0.02	0.05	0.15	0.13
SrO	0.01	<0.01	0.01	0.01	<0.01	<0.01	0.01	0.03	0.01	0.03
BaO	0.01	0.03	0.05	0.07	0.13	0.01	0.07	0.02	0.09	0.08
LOI	0.01	2.69	1.44	2.39	1.6	0.72	38.3	36	2.01	5.36
Total		98.22	101.63	101.88	100.07	100.79	96.26	96.58	100.29	99.01
	LOD									
ppm										
Ba	0.5	282	393	593	1130	46.2	584	659	823	686
Sr	0.1	91.1	240	210	50.9	87.8	181	212	230	352
Rb	0.2	31.5	13	12.3	126	6.2	0.6	65.9	122.5	91.7
Cs	0.01	0.48	0.44	0.53	1.72	0.09	0.12	1.1	1.77	1.37
V	5	102	11	33	21	78	7	23	110	124
Co	1	11	5	6	1	1	<1	2	8	5
Ni	1	19	2	5	3	7	<1	2	27	34
Cr	10	50	20	20	20	50	<10	30	90	90
Zr	2	117	249	265	215	193	5	120	177	179
Hf	0.1	3.5	7.4	7.8	7	5.4	0.2	3.7	5.2	5.3
Nb	0.1	5.8	5.8	9.3	9.6	9.5	<0.2	5.4	12.8	10.4
Ta	0.1	0.5	0.6	0.9	1.1	0.6	0.1	0.7	0.9	0.8
Ga	0.1	18.2	15.1	17	19.1	15.1	0.7	10.7	21.5	21.7
Tl	0.02	<10	10	<10	<10	<10	<10	<10	<10	<10
Li	10	10	<10	10	10	<10	<10	10	10	<10
Cd	0.5	<0.5	<0.5	<0.5	<0.5	<0.5	<0.5	<0.5	<0.5	<0.5
Mo	1	2	<1	1	1	1	2	<1	1	1
Sn	1	12	3	5	9	6	<1	5	3	6
W	1	6	2	3	5	4	1	5	3	3
Ag	0.5	<0.5	<0.5	<0.5	<0.5	<0.5	<0.5	1.8	<0.5	<0.5
As	0.1	<5	16	30	12	8	7	10	<5	<5
Pb	2	<2	6	2	10	3	3	8	6	8
Zn	2	6	16	11	10	18	16	20	15	20
Cu	1	1	27	79	4	6	17	11	25	8
Th	0.05	3.94	16.4	14.35	17	7.78	<0.05	8.56	10.95	9.58
U	0.05	1.65	5.88	6.13	9.52	4.72	0.13	5.04	3.88	3.46
Y	0.1	16.6	27.4	21.2	39.3	23.7	1.7	22.4	30.6	29.6
Sc	1	11	1	8	5	8	<1	4	15	14
La	0.1	11.8	5.3	11.7	37.7	10.1	1.9	21.2	39.7	34.6
Ce	0.1	24.2	14	27.8	78.9	19	2.9	44.8	81.8	74.5
Pr	0.02	2.65	1.98	3.4	9.14	3.35	0.29	5.14	8.97	8.34
Nd	0.1	10.2	9.2	14.8	33.8	14.2	1.4	19.2	32.5	31.9
Sm	0.03	1.85	3.1	3.3	7.01	4.11	0.38	3.92	5.76	5.91
Eu	0.02	0.84	0.49	0.52	0.57	0.33	0.25	0.61	1.08	1.19
Gd	0.05	2.26	3.63	3.13	6.86	3.52	0.46	3.67	5.05	5.84
Tb	0.01	0.45	0.7	0.53	1.15	0.67	0.07	0.59	0.85	0.87
Dy	0.05	3	5.21	3.48	7.09	4.28	0.36	3.87	5.5	5.43
Ho	0.01	0.61	1.09	0.81	1.49	0.82	0.05	0.79	1.16	1.14
Er	0.03	1.84	3.07	2.38	4.25	2.61	0.14	2.52	3.33	3.09
Tm	0.01	0.28	0.45	0.38	0.61	0.38	0.02	0.33	0.54	0.46
Yb	0.03	1.77	2.96	2.6	3.93	2.78	0.16	2.09	3.34	2.87
Lu	0.01	0.23	0.41	0.39	0.57	0.44	<0.01	0.3	0.49	0.41

Representative major, minor and trace element data from drill core selected samples. Major elements in wt.%; minor, trace and REE in ppm. *Limits of Detection

3.6. Whole-rock geochemistry

Major element bulk analysis was performed using X-ray fluorescence (XRF) whereas trace and rare earth element analysis were quantified by ICP-MS (Inductively Coupled Plasma – Mass Spectroscopy) through a fusing bead and acid digestion method. Both analyses were performed at ALS Seville Laboratories using the ME-XRF26 and ME-MS81 analytical packages.

4. Results

4.1. Host rock petrography and geochemistry

4.1.1. Escoural formation

At the study area, the Escoural Fm. is composed of quartz-feldspar paragneiss with feldspar porphyroblasts visible in hand samples. The matrix displays strong deformation, and mineral strain is materialized by the presence of fine plates of biotite surrounding the porphyroblasts of feldspar (Fig. 4**a**). These crystals have pale polysynthetic twinning and are associated with recrystallized fine-grained quartz on strain

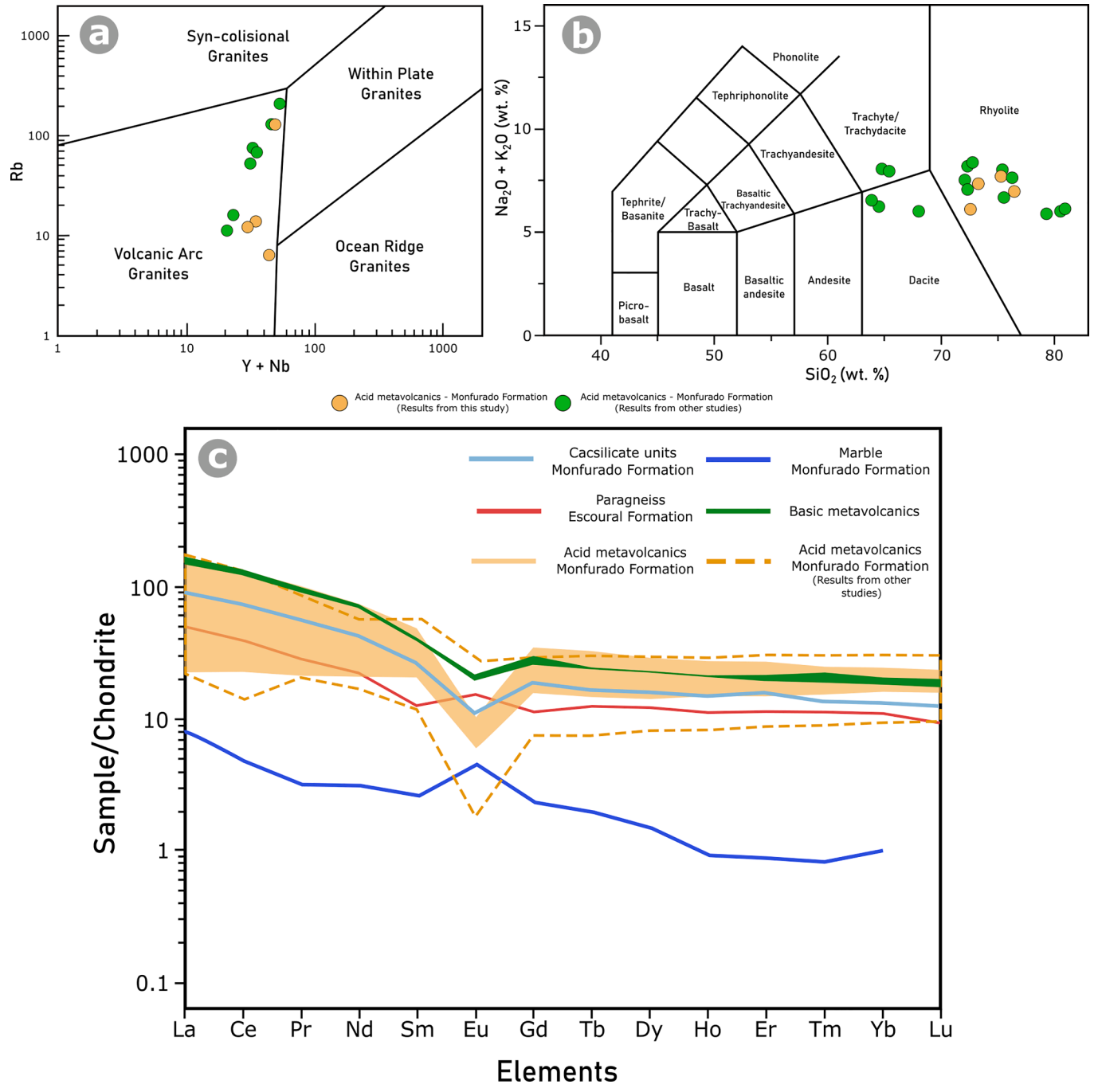

Fig. 5. a. Rb vs Y + Nb tectonomagmatic discriminant diagram (after Pearce et al., 1984) applied to the acid metavolcanic rocks of the Monfurado Fm.. **b.** Total alkali-silica diagram plot (after Le Maitre et al., 2012) of the acid metavolcanic rocks. **c.** Chondrite-normalized REE patterns representative of the host-rocks from the Monfurado deposit. In all diagrams a comparison is made to previous data for the acid metavolcanic rocks of the Montemor-o-Novo region (light-orange color dashed line; Chichorro, 2006; Pedro, 1996; Leal, 2001). Chondrite values after Palme and O'Neill (2014).

shadows. The quartz from the paragneiss matrix displays the development of ribbon textures, which outline the stretching lineation. Some samples exhibit the growth of amphibole (mainly actinolite), agreeing with the greenschist-amphibolitic metamorphic conditions described for the region.

Geochemistry of a paragneiss from this unit (**Sample 1;** Table 1) revealed relatively high SiO_2 content, low Al_2O_3 values (70.5 wt% and 12.8 wt%, respectively), and Na_2O/K_2O of 3.41, as expected for coarse metasedimentary rocks. The REE diagram normalized to Chondrite (Palme and ÓNeill, 2014; Fig. 5) show high fractionation of LREE over MREE (La/Sm_{CN} = 3.98), slightly flat HREE (Sm/Yb_{CN} = 1.13), and a marked positive Eu anomaly (McLennan 1989) of Eu/Eu* = 1.25. Such values are slightly different than other major element geochemical data of metagraywackes and paragneisses from *Serie Negra* reported in literature (SiO_2 = 55 – 66 wt%, Al_2O_3 = 15 – 19 wt%; Pereira et al., 2006; Lopes, 2015; Díez-Fernández et al., 2017). Likewise, the steep LREE/MREE patterns are observed in bibliographic data, but contrast with the considerable negative Eu anomalies (Eu/Eu* = 0.43 – 0.87).

4.1.2. Monfurado formation (Lower unit)

The acid metavolcanic rocks are composed of a quartz-feldspar matrix, with a white to greyish color in hand sample, and are often crosscut by late-quartz veins. Local variations of this lithology display biotite development, observable in hand samples.

Thin section examination allows to describe this lithotype as medium-grained, mainly composed of euhedral quartz crystals (Qz I) with sparse large porphyroblasts of feldspar (Fig. 4**c**), mostly plagioclase which exhibit polysynthetic twinning. Hydrothermal alteration is pervasive and is materialized by intense sericite alteration of plagioclase (Fig. 4**c**). Quartz exhibits deformation features, such as undulatory extinction and ribbon textures in the most deformed sections, whereas biotite is found in fine plates, sub-parallel to the main foliation plane.

The acid metavolcanic rocks are strongly affected by brittle deformation that promoted the development of centimetric quartz veining (Qz IIa/IIb; Fig. 4**c, d**). The Qz IIa veins correspond to sub-vertical structures that generally crosscut bedding and are ubiquitously accompanied by tourmaline (Fig. 4**d**). These veins are perpendicularly crosscut by Qz IIb veins, which are mainly composed of quartz, feldspar and pyrite (Fig. 4**c**).

Tourmaline is cogenetic with quartz IIa, and displays characteristic triangular basal sections (Fig. 4**d, e**), with green to brownish optical zoning, and subhedral to euhedral shapes. Epidote aggregates are seldomly observed throughout the matrix, along with Qz I.

Samples of the acid metavolcanic rocks (**Sample 2, 3, 4, and 5;** Table 1) revealed chemical compositions consistent with a rhyolite to rhyodacite calc-alkaline affinity (Fig. 5**b**) and volcanic arc-like signature (Nb/Y = 0.21–0.44; Fig. 5**a**). CN REE generally displays flat patterns with subtle enrichments in LREE over MREE and HREE (La/SmCN = 1.1 – 3.4; Sm/YbCN = 1.1 – 1.9; Fig. 5), well pronounced negative Eu anomalies (Eu/Eu*= 0.25 – 0.49) and slightly demarked Ce anomaly (Ce/Ce*= 0.79 – 1.07), according to the McLennan (1989) equation. The herein presented geochemical data for the acid metavolcanic rocks is consistent with previously published data regarding other MNSZ rift-related volcanic events (Pedro, 1996; Leal, 2001; Sánchez-García et al., 2003; Sánchez-García et al., 2019; Chichorro, 2006)

4.1.3. Monfurado formation (Upper unit)

The transition from acid to basic metavolcanic rocks is identified by other authors (Chichorro, 2006; Salgueiro, 2011), and is distinguishably marked by the presence of amphibolic units, some with schistosity. These rocks are composed of amphibole, namely hornblende and medium-grained feldspar porphyroblasts with an oval shape and strongly sericitized cores (Fig. 4**b**). Geochemistry of intermediate/basic metavolcanic samples from these sections (**Samples 8 and 9;** Table 1) showed SiO_2 values between 60.8 wt% and 49.1 wt%., respectively. Both samples have relatively high alumina and alkali content (Al_2O_3 = 16.75 wt% and 14.3 wt%; $Na_2O + K_2O$ = 7.3 wt% and 4.3 wt%), although, in sample 8, trace element chemistry is characterized by low Nb/Y (0.41) and Zr/Ti (0.04), but high LILE components (Rb = 122 ppm; Ba = 823 ppm; Sr = 230 ppm), which is in accordance with volcanic-arc tectonic setting of emplacement. Sample 9 (Table 1), besides displaying lower SiO_2 values, has very high CaO content (17.4 wt %); also, trace element ratios (Ti/V = 27.5, Zr/Y = 6.0) display affinities with basalts characteristic of E-MORB and within-plate environments, resembling the possible tectonic setting of the overlying Carvalhal Fm. (Pearce and Norry, 1979; Shervais, 1982; Chichorro et al., 2008; Sánchez-García et al., 2019).

Marbles (Fig. 4**f**) are ubiquitous to the upper unit of the Monfurado formation, usually displaying a calcite-dolomite matrix as revealed by the high CaO (29.3 wt%) and MgO (18.3 wt%) contents (Sample 6).

Hydrothermal alteration of marbles is revealed by the development of calcsilicate assemblages dominated by actinolite-tremolite, which is sometimes accompanied by pyrite (Fig. 4**g**). One selected calcsilicate sample (Sample 7) revealed higher SiO_2, Al_2O_3, and CaO values (6.88 wt %, 1.51 wt%, and 36.8 wt%), with lower Fe_2O_3 and MgO contents (3.35 wt% and 10.95 wt%) when compared to the pristine marble sample.

4.2. Mineralized domains

Different types of mineralization can only be identified through detailed petrographic characterization of the ores. Such work is essential in understanding the succession of events related to ore deposition, providing the sequence of crystallization and its relationship with the complex geological history of the region.

4.2.1. Pre-Gold ore stage

4.2.1.1. Oxides. The Monfurado gold prospect is spatially associated with iron ore bodies that belong to the Monges mine and are mainly hosted in marbles and calcsilicate rocks (Fig. 2). The iron ores possibly formed through submarine hydrothermal activity during the Cambro-Ordovician intracratonic rifting settings (Salgueiro, 2011), which are prone to the formation of SEDEX-VMS deposits.

The iron-rich domains intersected by the drill cores are fundamentally composed of metric massive to disseminated magnetite sections hosted in a calcite-dolomite matrix, with minor pyrite and sparse chalcopyrite. Needle-like amphibole crystals, identified as actinolite-tremolite, accompany the iron oxides (Fig. 6**a**) that display intense deformation as evidenced by the boudin-shaped magnetite crystals (Fig. 6**a**). Barite is found in close relation with magnetite and is, possibly, contemporary of its deposition.

4.2.1.2. Sulfides paragenesis. Two main pre-ore pyrite-rich sulfide domains were identified as (1) isolated pyrite crystals hosted in marbles from the Upper unit of the Monfurado Fm. (Fig. 6**b**), and usually accompanied by amphibole-chlorite assemblages; and (2) massive pyrite layers in a fine-grained and euhedral quartz matrix, in which pyrite is usually surrounded by chlorite-amphibole aggregates with minor epidote (Fig. 6**c**). The quartz matrix found in this section suggests a volcanogenic nature for these pyrite accumulations, possibly similar to the one associated with the iron ores (SEDEX-VMS; Salgueiro, 2011).

4.2.2. Gold ore stage

4.2.2.1. Gold-sulfides assemblages in massive sulfide layers. A massive sulfide layer (MSL) is present in the majority of the studied drill cores, apparently marking a laterally continuous layer, with an approximate thickness of 3 to 15 m. During the exploration campaigns the attention was drawn to M5, M7, and M12 drill cores (Fig. 2), which revealed gold grades up to 18 g/ton in the MSL intersected by these drill cores (Fig. 2).

The MSL is hosted in metasomatized marbles of the Monfurado Fm.

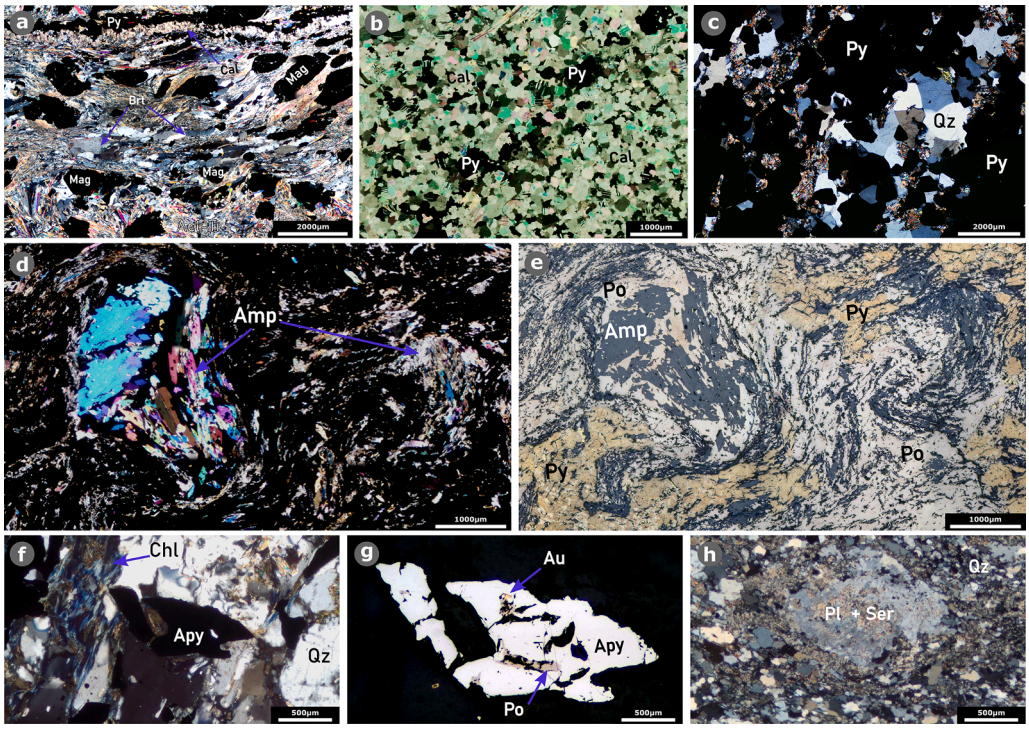

Fig. 6. Mineralized domains petrography showing host-rock relations and translucid mineral identification. **a.** Crossed nicols composite microphotograph of the pre-gold oxide domain section in which dispersed opaques (Mag-magnetite) are accompanied by tremolite-actinolite in a calcsilicate matrix. Barite shows a ribbon texture which might indicate deformation. This section is crosscut by a late calcite-pyrite vein. **b.** Crossed nicols composite microphotograph of a pre-gold sulfide domain constituted mainly by pyrite in a calcite-dolomite matrix (Monfurado Fm. marbles), sometimes showing the development of tremolite in the pyrite-calcite contact. **c.** Crossed nicols composite microphotograph of a pre-gold sulfide domain mainly composed of massive pyrite in a quartz volcanogenic matrix. **d.** and **e.** Crossed nicols and reflected light composite microphotograph, respectively, of the gold-mineralization sulfide-rich layers in which amphibole develops along with pyrrhotite and pyrite. Pyrrhotite displays intense deformation (folding) with rotation of the larger amphibole crystals. **f.** Crossed nicols transmitted light composite microphotograph, of the gold-mineralization arsenopyrite-rich layers. Arsenopyrite is found in a quartz dominated matrix and develops along with Fe-rich chlorite (pennine). **g.** Reflected light of the section shown in (f.) at a x5 magnification, showing gold inclusions in arsenopyrite. **h.** Crossed nicols transmitted light composite microphotograph of the acid metavolcanic matrix, composed by fine-grained subhedral quartz crystals and large sericitized plagioclase porphyroclasts.

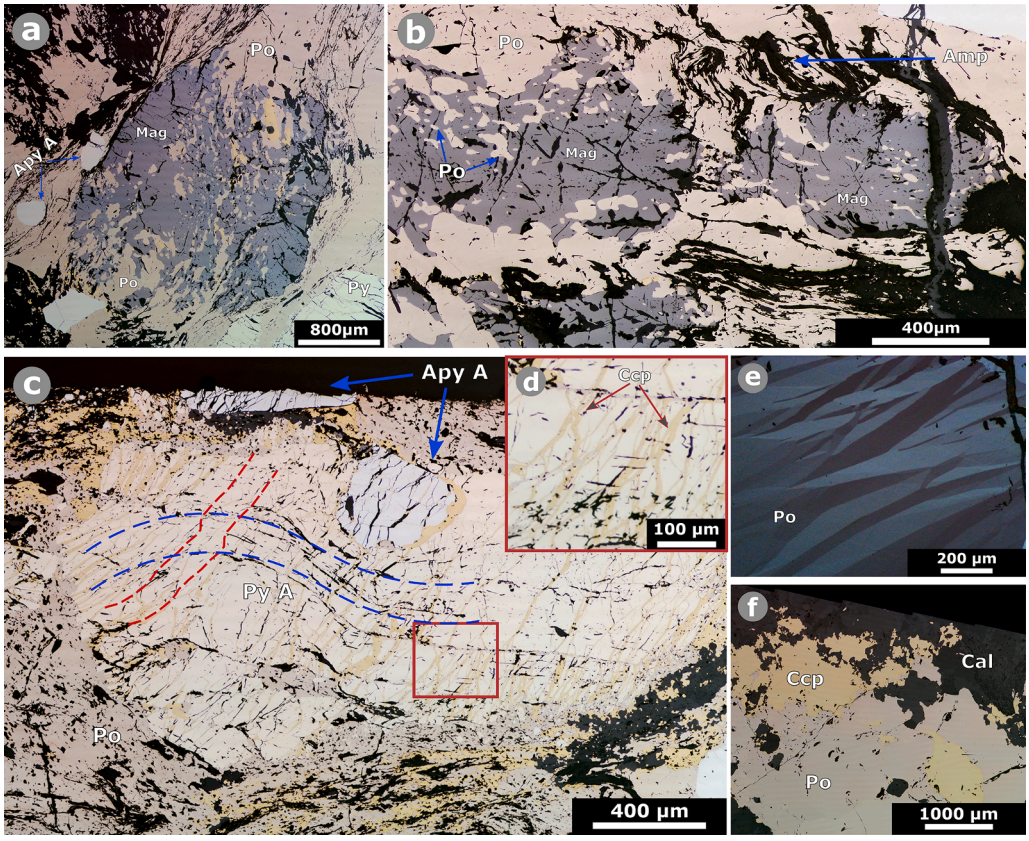

Fig. 7. Composite microphotographs of ore petrography performed on cross sections from the massive sulfide horizons. **a.** and **b.** Sulfidation process in which alteration of magnetite to pyrrhotite occurs. Magnetite (grey) correspond to relics of the sulfidation process within pyrrhotite. **(c.)** composite image of 16 microphotographs (x5 magnification) showing pervasive brittle-ductile deformation, marked by the red and blue dashed lines. **d.** magnification of a section from figure (c.) showing a stockwork texture of late ore-stage chalcopyrite, filling fractures generated during brittle deformation. **e.** reflected light crossed nicols microphotograph of a pyrrhotite crystal section. The undulatory extinction is pronounced by the corrugation lamellae/deformation twinning. **f.** late-stage deposition of chalcopyrite around pyrrhotite in a low-deformed calcite-dolomite marble of the Monfurado Formation.

(Fig. 3), having pyrrhotite as the dominant sulfide phase and usually accompanied by fine to medium-grained actinolite-tremolite crystals (Fig. 6**d, e;** Fig. 7**b**). Pyrite, arsenopyrite, and chalcopyrite are also present in variable proportions.

Magnetite is partially replaced by pyrrhotite, and sparse relicts of the iron oxide are found within pyrrhotite, outlining the presence of sulfidation processes, (Fig. 7**a and b**). Pyrrhotite preserves ductile deformation at all scales, displaying *durchbewegung* textures (e.g. Marshall and Gilligan, 1989) in hand samples (Fig. 8**a, b**) and, at a microscopic scale, corrugation lamellae/deformation twinning and strong anisotropy (Fig. 7**e**). Pyrrhotite mostly surrounds arsenopyrite and pyrite crystals (Fig. 7**c**) although, to a lesser extent, it is found in less deformed sections (Fig. 7**f**) in pyrrhotite-pyrite-chalcopyrite assemblages.

In these layers gold is mainly associated with arsenopyrite (Apy A in Fig. 8) and pyrite (Py A in Fig. 9), although not exclusively. Arsenopyrite A display syn-kinematic textures that are compatible with the high strain observed in the host rocks

A small and localized arsenopyrite-rich layer (Apy B in Fig. 8**c**) was identified in a quartz-chlorite matrix in a 0.6 m thick section of the M7 drill core (Fig. 6**f, g**). The relation between Apy B and the host rock is difficult to discern, nevertheless, it was possible to identify that the matrix is characterized by fine-grained anhedral quartz crystals and arsenopyrite is ubiquitously surrounded by chlorite with berlin-blue birefringence colors (Fig. 6**f**). Small and rare gold grains hosted in Apy B (Fig. 6**g**) and disperse in the quartz matrix (Fig. 8**n, o**) were identified, with no clear spatial relation to the MSL. The microscopic analysis of Apy A and Apy B suggests that they are homogeneous mineral phases, with no optical zonation, however, the backscatter electron images revealed a faint compositional zonation, indicating a slight arsenic depletion towards the rims of Apy A (Fig. 8**g, h, i**).

Gold grains are mostly found in arsenopyrite usually occurring as fracture filling in Apy A (Fig. 8**h to m**), and to a lesser extent in Py A (Fig. 9**c, d, g, h**). Ductile deformation in Py A crystals (Fig. 7**c**; blue dashed lines) is outlined by the presence of acicular amphibole, whereas brittle deformation is marked by perpendicular fracturing associated with micro-scale cataclasis (Fig. 7**c**; red dashed lines), affecting both Apy

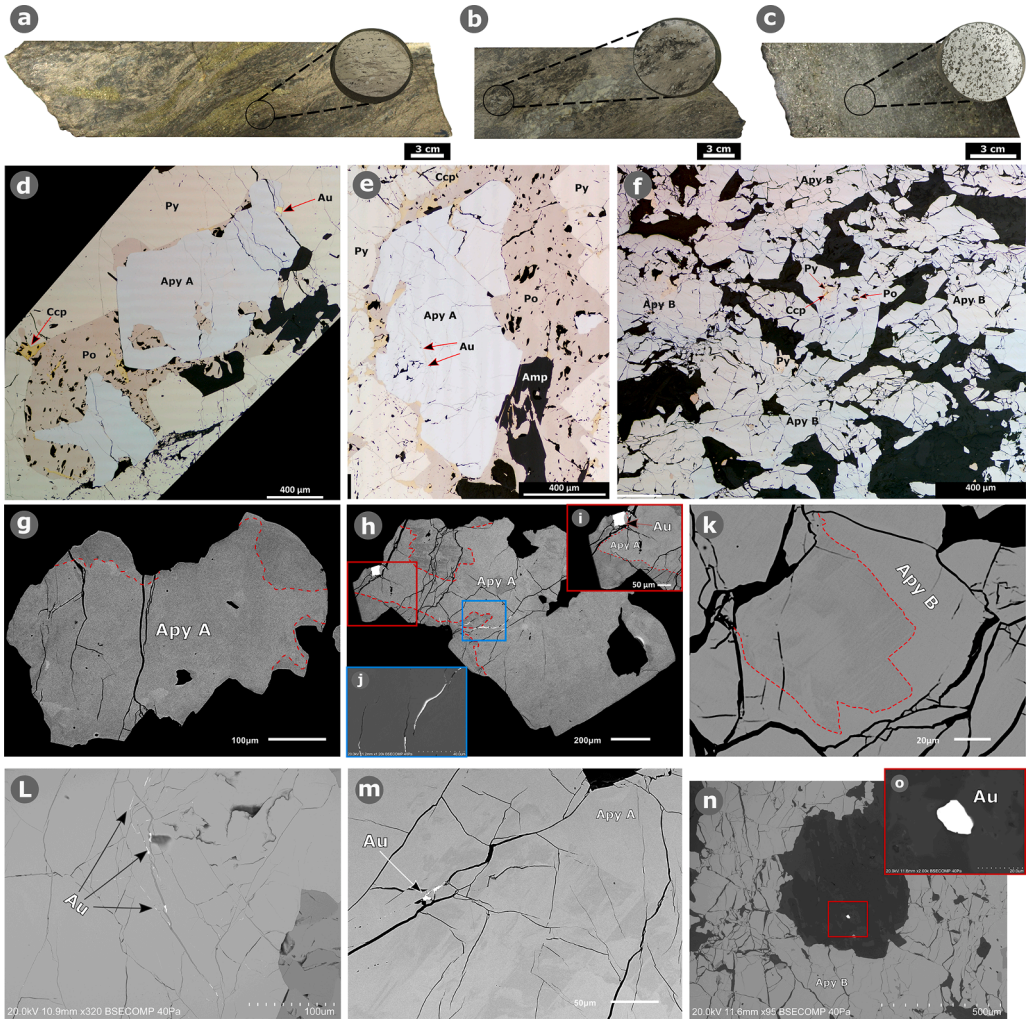

Fig. 8. Representative samples, microphotographs and scanning electron microscopy (SEM) images of the main arsenopyrite paragenesis. **a.** massive sulfide horizon intersected by M5 drill core (@86 m) and one of the prepared polished drill core cross sections. **b.** massive sulfide horizon in a calcite-dolomite matrix intersected by M5 drill core (@87 m) and one of the prepared polished drill core cross sections. **c.** Massive arsenopyrite horizon intersected by M7 drill core (@123 m) and one of the prepared polished drill core cross sections. **d.** Composite image of 8 microphotographs (x5 magnification) from the cross section shown in (a.), in which gold occurs in arsenopyrite (ApyA) microfractures. **e.** Composite image of 6 microphotographs (x5 magnification) showing a massive sulfide layers (Po + Py + Apy) with gold particles being associated to fractures in arsenopyrite. **f.** Composite image of 6 microphotographs (x5 magnification) of an arsenopyrite-rich layers (Apy B) assemblage in a siliciclastic matrix. This image corresponds to the same cross section shown in (b.). **g.** SEM image of an arsenopyrite crystal (Apy A) from a massive sulfide layer in which it was possible to individualize a subtle zonation marked by the red dashed lines. Arsenopyrite rims are slightly impoverished in arsenic. **h.** SEM image of the same section shown in (d.) in which it is possible to identify gold (bright areas) distribution on arsenopyrite. Gold particles mainly occur in arsenopyrite rims (red square) and as a fracture filling phase (blue square). Consistent zonation is individualized with a slight decrease in the arsenic content, marked by the red dashed lines. **i.** Zoom-in to the red square section from (h.), in which a 50 µm gold particle is identified as being associated to the Apy A arsenic depleted rim. **j.** Zoomed section of the blue square from (h.) in which fractures of arsenopyrite are filled by gold. **k.** SEM image of an arsenopyrite crystal (Apy B) from the arsenopyrite-rich layers in which it was possible to individualize a subtle zonation. The sample here presented corresponds to the same cross section shown in (c.) and (f.). **l.** SEM image showing distribution of gold inside arsenopyrite (Apy A) from a massivesulfide layers. **m.** SEM image showing distribution of gold inside arsenopyrite (Apy A) from a massive sulfide layer. **n.** SEM image of one free gold particle (red square) in a siliciclastic matrix from the arsenopyrite-rich layers shown in (c.) and (f.). **o.** Zoomed section to the free gold particle from (n.).

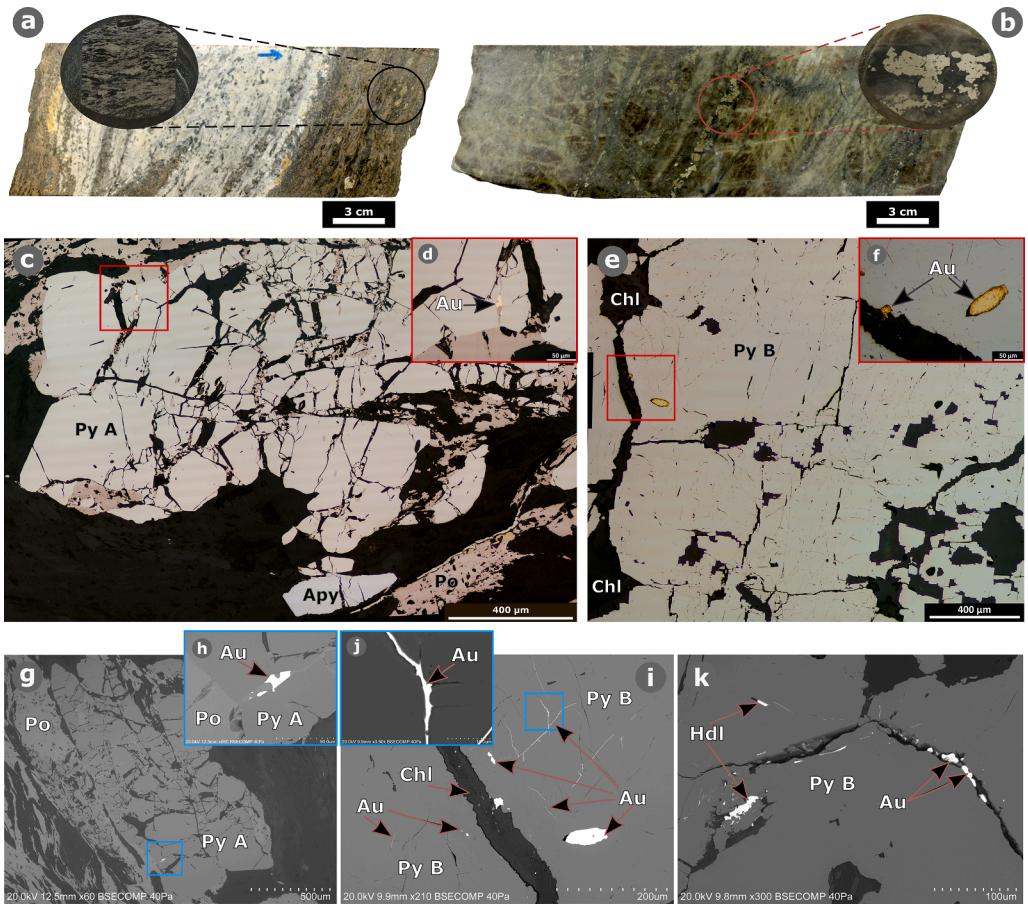

Fig. 9. Representative samples, microphotographs and SEM images of the main pyrite paragenesis. **a.** massive sulfide layer in calcite-dolomite intercalations, intersected by M7 drill core (@110.5 m) and one of the prepared polished drill core cross sections. **b.** Pyrite-chlorite vein-type mineralization hosted in acid metavolcanic rocks. Drill core sample collected from M7 (@ 107.4 m) and one of the prepared polished drill core cross sections. **c.** Composite image of 10 microphotographs (x5 magnification) from the polished cross section shown in (a.). This section corresponds to a massive sulfide layer in which Pyrite A is identified. **d.** Zoomed section from the red square shown in (c.) in which a gold particle is identified in a pyrite fracture. **e.** Composite image of 8 microphotographs (x5 magnification) from the pyrite-chlorite vein structures shown in (b.). **f.** Zoomed in section from the red square shown in (e.) in which a large (80 µm) gold particle is individualized, along with a smaller particle. **g.** SEM imagery of the field of view shown in (c.), revealing that Py A do not show any relevant zonation. The blue square identifies the location of a gold. **h.** Zoomed in blue square section from (g.), the bright zone corresponds to a gold particle. **i.** SEM image showing the gold distribution and textures in Pyrite B. This image corresponds to the same field of view shown in (e.). Gold distribution in Py B fractures (blue square) were only possible to identify by SEM imagery, revealing a higher gold content. **j.** Zoomed blue square section from (i.) field of view, in which fracture filling by gold is observed. **k.** Gold and hedleyite distribution as fracture filling from Py B.

A and Py A. This type of deformation texture is particularly well preserved in the M4, M5 and M7 drill cores.

Chalcopyrite is abundant in the MSL, mostly found as fracture filling of Apy A, Py A and pyrrhotite (Fig. 7**c,** Fig. 10**b**). Other relatively late sulfide phases, such as inclusions of hedleyite and altaite, were identified mainly associated to pyrrhotite (Fig. 10**d, e**). Sphalerite is observed along some fractures of arsenopyrite (Fig. 10**c, g**), whereas galena is found in fractures along with pyrrhotite and/or chalcopyrite.

4.2.2.2. Gold-sulfides assemblages in acid metavolcanic rocks. Gold is also found in pyrite fractures (Fig. 9**i, j**) hosted in late veins crosscutting the acid metavolcanics, which exclusively occur at top of the MSL (Qz IIb; Fig. 4**c, d, e**). Pyrite hosting this gold mineralization type is addressed as Py B. The macroscopic analysis of hand samples suggests that pyrite is accompanied by chlorite and Qz IIb deposition and is controlled by late fracturing of the host rock (Fig. 9**b**).

Pyrite crystals (Py B) are usually euhedral, large (size > 400 µm) ; Fig. 9**b, e**), and accompanied by intense chloritization of the host rock. At a microscopic scale, native gold is found in chlorite ± quartz assemblages (Fig. 10**a**), and filling thin fractures in Py B, as revealed by backscattered imagery (Fig. 9**i, j**). Hedleyite was also found in Py B microfractures (Fig. 9**k,** Fig. 10**f**).

4.3. Sequence of crystallization

The sequence of crystallization for the Monfurado gold prospect (Fig. 11) was identified by petrography and descriptions of the textural features of the ores. Two main stages of metal input were identified: i) the pre-ore stage with an oxide and sulfide paragenesis and ii) the ore stage, in which gold mineralization is found in MSL, as well as in quartz-chlorite-pyrite veins hosted in the acid metavolcanic rocks.

Concerning the ore stage, two main types of gold mineralization were identified, as follows:

- Type i) correspond to gold in the MSL, which is ubiquitously composed of massive pyrrhotite and contains disseminated arsenopyrite (Apy A) and pyrite (Py A). These sulfide layers are sub-parallel to the surrounding iron-rich carbonate host rocks of the Monfurado Fm.. Gold deposition occurs in the rims and as fracture filling of arsenopyrite (Fig. 8) and, to a lesser extent, pyrite (Fig. 9). A single and constrained gold occurrence was found, in which Au is hosted in a layer composed almost exclusively of arsenopyrite (Apy B).
- Type ii) mineralization is characterized by vein-hosted gold mineralization crosscutting the metavolcanic acid rocks. Gold is sometimes accompanied by Bi-Te phases (Fig. 10) and occurs as fracture filling of pyrite (Py B) associated with silicification and chloritization.

4.4. Fluid inclusion studies

4.4.1. Fluid inclusion petrography

Quartz-hosted fluid inclusions are common throughout the studied samples, while inclusions hosted in tourmaline, barite and tremolite are

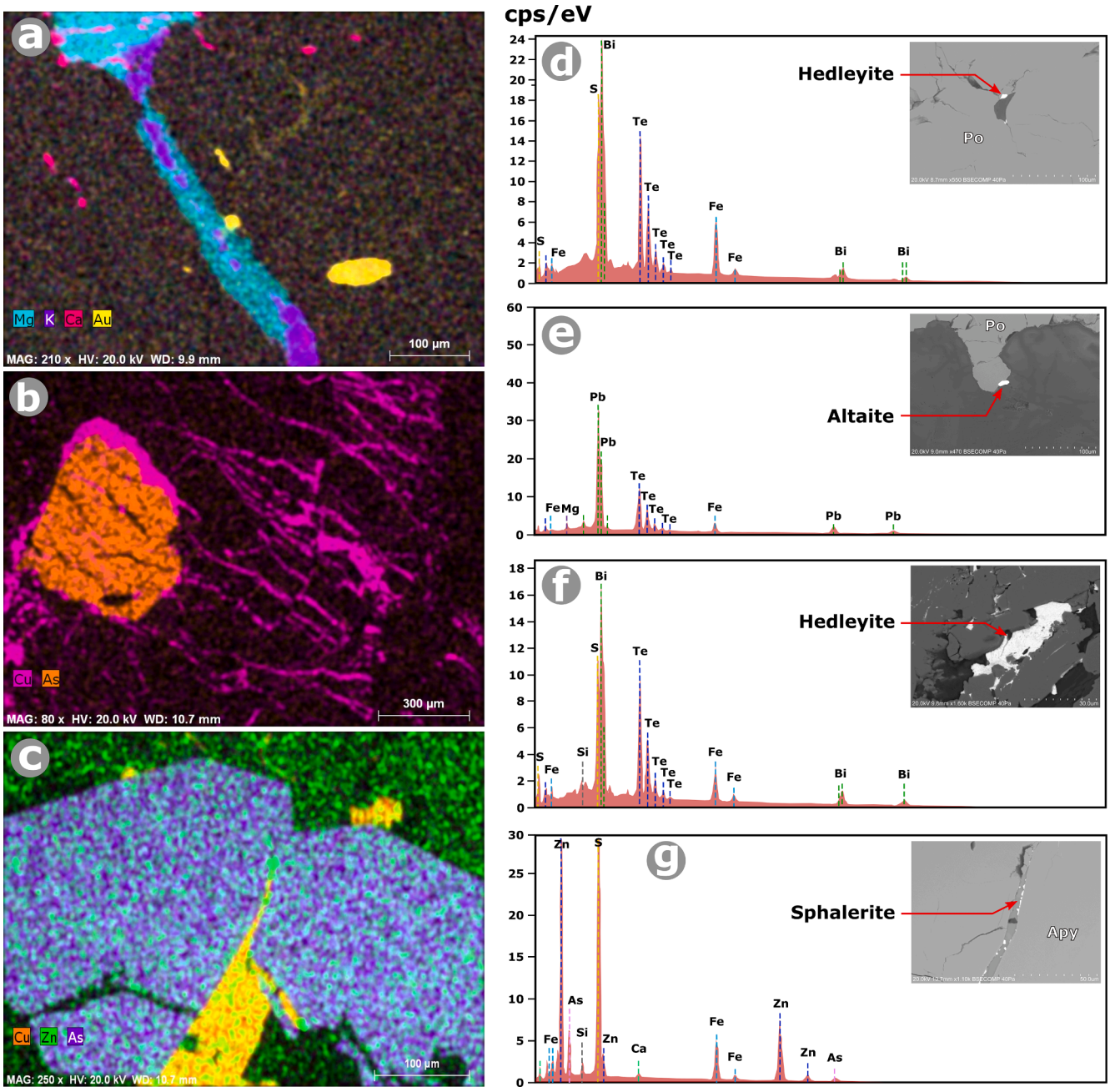

Fig. 10. EDS mapping (a. to c.) and single spot analysis (d. to g.) of different sections and mineral phases representative of the Monfurado deposit paragenesis. **a.** EDS map of the field of view shown in Fig. 9-(e.), in which the distribution of gold is observed (yellow) inside a pyrite crystal and a chlorite vein. **b.** EDS map acquired in the field of view shown in Fig. 7-(c.) showing the stock-work distribution of chalcopyrite, filling fractures in pyrite and arsenopyrite. **c.** EDS map of an arsenopyrite crystal from a sample collected from the massive sulfide layers, in which it is possible to identify late Cu and Zn mineral phases filling a fracture. **d.** Hedleyite identification in a pyrrhotite porosity. **e.** Altaite identification on the borders between pyrrhotite and a calcite-dolomite matrix. **f.** Hedleyite identification as fracture filling in Py B. **g.** Sphalerite identification filling a fracture of Apy A.

rarer, smaller, and harder to study due to the color and cleavage of the host minerals. Quartz samples were prepared from veins crosscutting the acid metavolcanics and calcsilicate rocks of the Monfurado Fm., described as Qz IIb (Fig. 4**c;** Fig. 12**a-d**).

Barite and tremolite samples were prepared from calcsilicate rocks of the Monfurado Fm., which is the result of regional metamorphism and metasomatic alteration of marbles. The crystals are disseminated in a tremolite dominated matrix. Tourmaline samples were prepared from quartz-tourmaline - Qz IIa veins (Fig. 4**d, e**) - which are cross-cut by Qz IIb veins in the acid-metavolcanic rocks (Fig. 12**d**).

Four types of fluid inclusions were identified, and the adopted fluid inclusion terminology is according to Boiron et al. (1992). Lc-w inclusions correspond to triphasic FÍs ($L_{H2O\text{-}NaCl} + L_{CO2} + V_{CO2}$; Fig. 12**e**) with carbonic and aqueous volumetry varying significantly, occurring in transgranular fluid inclusion planes (FIP) in Qz IIb from veins that exclusively crosscut calcsilicate rocks. Lw_1 FÍs occur as clusters of biphasic inclusions (L + V), hosted in baryte, tremolite (Fig. 12**f**) and tourmaline (Fig. 12**i**). Lw_2 inclusions are biphasic (L + V; Fig. 12**g**), mainly found in transgranular FIP in quartz-plagioclase-chlorite-pyrite veins (Qz IIb; Fig. 12**a-d**). The volumetric proportion ratio between the liquid and vapor phase varies between 10 and 15 bubble vol. % for both Lw_1 and Lw_2 inclusions. The aqueous Lw_1 and Lw_2 fluid inclusions

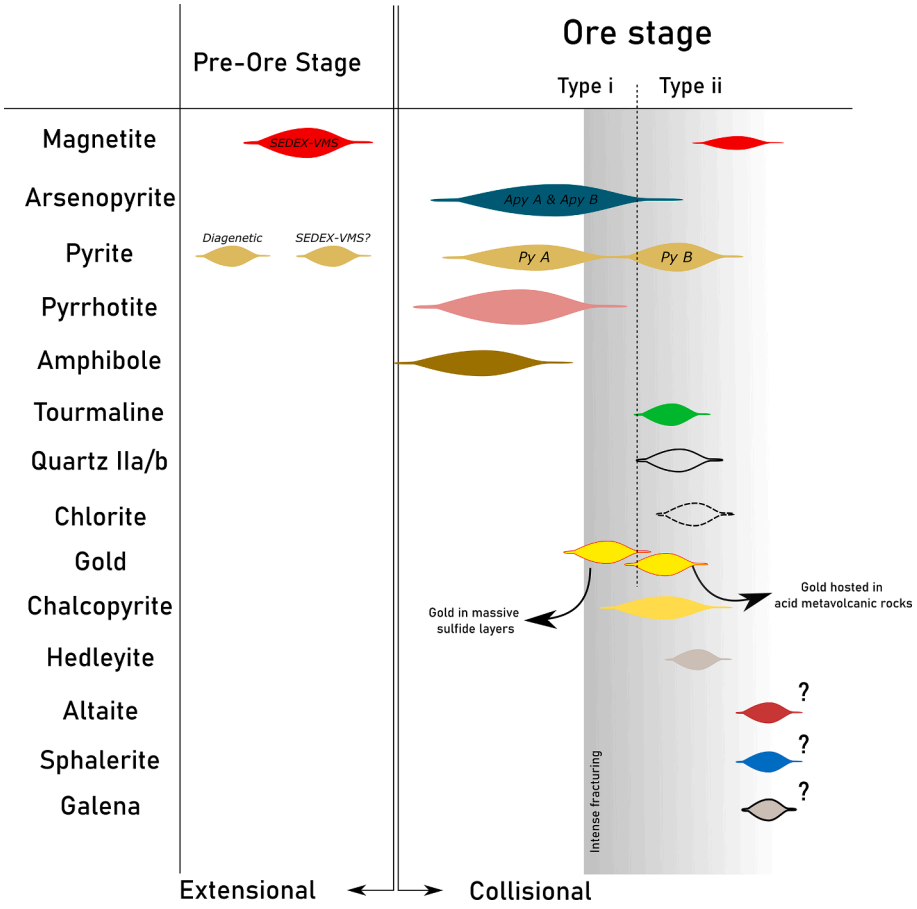

Fig. 11. Mineral assemblages and sequence of crystallization representative of the Monfurado gold prospect.

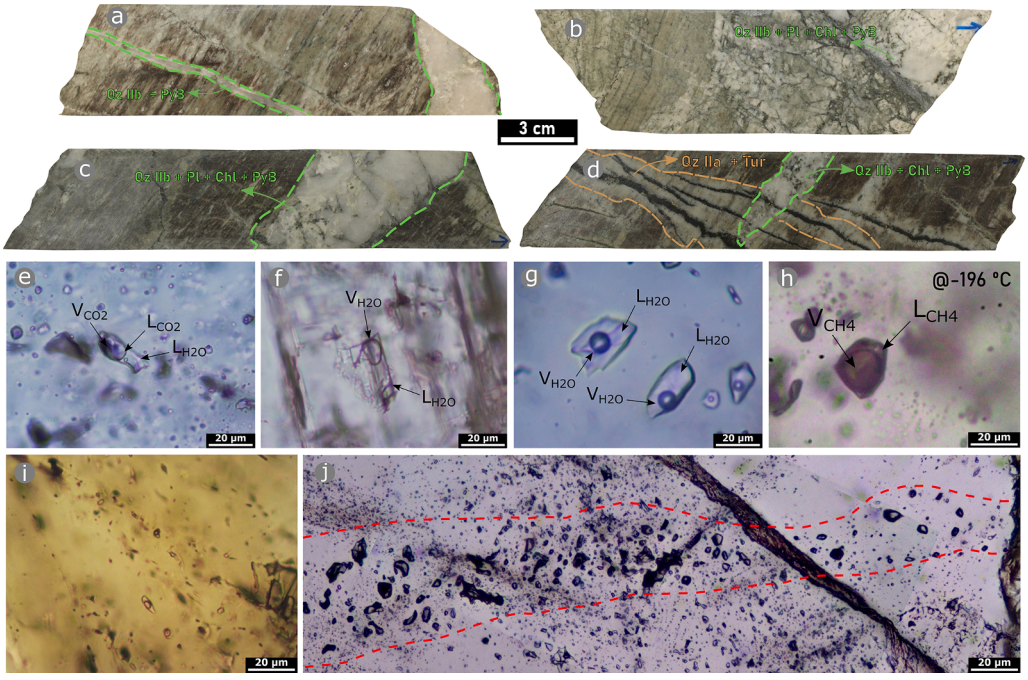

Fig. 12. a. – d. Representative photos of the drill core samples that display the crosscutting relation among veins from which tourmaline and QzIIb were used in the fluid inclusion study. **e. – j.** Microphotographs representative of the fluid inclusion types individualized throughout this study. **e.** Lc-w three-phase aquo-carbonic fluid inclusions hosted in quartz. **f.** Lw_1 two-phase fluid inclusions hosted in a tremolite crystal. **g.** Lw_2 two-phase aqueous fluid inclusions hosted in Qz IIb. **h.** The figure shows a L_{CH4} fluid inclusions during the microthermometry studies under a temperature of −196 °C. **i.** Lw1 fluid inclusions hosted in tourmaline prepared from the drill core sample shown in (d.). **j.** Composite microphotograph and image stacking showing a V_{CH4} fluid inclusion plane in Qz IIb prepared from the drill core sample shown in (a.).

show a clear dominance over Lc-w and are found in samples from different depths.

Lastly, methane-rich fluid inclusions (Fig. 12**h**) hosted in quartz were identified in transgranular FIP (Fig. 12**j**) and were exclusively observed in samples from quartz veins (Qz IIb) crosscutting the acid metavolcanic-rocks from the Monfurado Fm. (Fig. 12**a-d**). These inclusions have an

oval shape, with liquid CH_4 displaying a dark color and homogeneous aqueous H_2O-phase proportion (5%), at room temperature.

4.4.2. Microthermometry

Summarized microthermometry results are shown in Table 2 and Fig. 13, and the complete data is provided in **Supplementary Material A**. Lc-w fluid inclusions showed Tm_{CO2} ranging between −58.6 °C and −56.8 °C which indicates a near CO_2-pure phase, with minor concentrations of CH_4 (≈5% mol; Thiery et al., 1994; Maia et al., 2019). Th_{CO2} ranged from 0 °C to 24.6 °C and homogenization exclusively occurred into the liquid phase. Clathrate phases were identified in Lc-w inclusions, however, due to the small size and clustered occurrence of these FÍs, a correct measurement of Tm_{chl} was not possible, thus it was not possible to perform salinity and pressure estimations.

Ice melting temperatures measured in Lw_1 inclusions hosted in baryte range from −22.1 °C to −3.7 °C, and homogenization occurs into the liquid phase (L + V → L) with Th from 274 °C to 309 °C with a median of 290 °C. Salinities (eq. w(NaCl)) range from 6.0 to 23.1 eq. w (NaCl), with median pressure (*Md*) estimations of 5.0 MPa.

Lw_1 inclusions hosted in tremolite display Tm_{ice} between −16.6 °C and −1.5 °C, and Th ranging between 195 °C and 330 °C with a median of 305 °C. The calculated salinities range from 2.6 to 19.9 eq. w(NaCl) with a median of 12.1 eq. w(NaCl) and estimated pressures are in the range of 1.3 MPa to 11.8 MPa, with a median of 8.7 MPa. Fluid inclusions in tourmaline are small (5 μm), therefore only eight complete measurements were performed, with Tm_{ice} ranging between −6 °C and −0.5 °C and Th from 420 °C to 460 °C (*Md* = 425 °C). Correspondent salinities range from 0.9 to 9.2 eq. w(NaCl) with a median of 2.1 eq. w (NaCl), and the pressure estimations range from 27.6 MPa to 32.4 MPa, with a median of 29.8 MPa.

Table 2
Summarized microthermometry results and descriptive statistics obtained from the fluid inclusions studies.

		Lc-w	Lw_1			Lw_2	L_{CH4}	V_{CH4}
		Quartz	Baryte	Tourmaline	Tremolite	Quartz	Quartz	
Te	Min.	N.D.	N.D.	N.D.	N.D.	−33		
	Max.					−15		
	Mean					−24.9		
	Median					−25	N.D.	N.D.
	Std. Dev.					3.9		
	1st Quartile					−27		
	3rd Quartile					−23		
Tm_{CO2}	Min.	−58.6	N.P.	N.P.	N.P.	N.P.		
	Max.	−56.8						
	Mean	−57.4						
	Median	−57.3					N.P.	N.P.
	Std. Dev.	0.5						
	1st Quartile	−57.8						
	3rd Quartile	−57.0						
Th_{CO2}	Min.	0	N.P.	N.P.	N.P.	N.P.		
	Max.	24.6						
	Mean	10.1						
	Median	9.8					N.P.	N.P.
	Std. Dev.	6.7						
	1st Quartile	4.5						
	3rd Quartile	16.7						
Tmice	Min.	−14.3	−21.2	−6	−16.6	−14.3	−6.2	
	Max.	−4.5	−3.7	−0.5	−1.5	−0.1	−0.9	
	Mean	−7.3	−12.6	−1.9	−7.6	−4.8	−3.05	
	Median	−6.0	−13.4	−1.2	−7.4	−4.0	−2.55	N.D.
	Std. Dev.	3.1	6.9	1.7	3.9	3.2	1.955	
	1st Quartile	−9.0	−20	−2	−10.1	−5.8	−5.375	
	3rd Quartile	−4.7	−4.9	−1	−5.8	−2.9	−1.225	
Th	Min.	N.D.	274	420	194.5	125.4	−143.5*[1]	−141
	Max.		309	460	330	327.0	−136.3	−136
	Mean		283	437.9	292.3	225.8	−140.9	−138.117
	Median		275	425	305	227.5	−141.8	−137.6
	Std. Dev.		15	19.3	35.5	46.0	2.2	1.4
	1st Quartile		274	420	267.5	203.2	−142.7	−139.45
	3rd Quartile		301	460	315.2	252.8	−138.3	−137.15
Salinity	Min.	N.D.*	6.0	0.9	2.6	1.7		
	Max.		23.1	9.2	19.9	15.3		
	Mean		17.0	3.2	11.1	6.8		
	Median		19.4	2.1	12.1	6.0	N.D.	N.D.
	Std. Dev.		6.7	2.6	4.9	3.0		
	1st Quartile		8.8	1.7	6.9	4.8		
	3rd Quartile		22.7	3.4	16.7	8.4		
Ph(MPa)	Min.		4.95	27.6	1.3	0.3	0.36*[2]	0.42
	Max.		9.4	32.4	11.8	11.9	0.54	0.55
	Mean		6.5	29.9	7.4	3.0	0.42	0.49
	Median	N.D.*	5.0	29.8	8.7	2.5	0.40	0.51
	Std. Dev.		2.1	1.9	3.1	2.3	0.06	0.04
	1st Quartile		4.95	27.6	4.7	1.5	0.38	0.46
	3rd Quartile		9.4	32.4	10.0	3.6	0.49	0.52

N.D. = not determined; N.P. = not present; N.D.* = $Tm_{(chl)}$ is needed to calculate this parameter; *[1]Homogenization of CH_4; *[2] Pressure at CH_4 homogenization

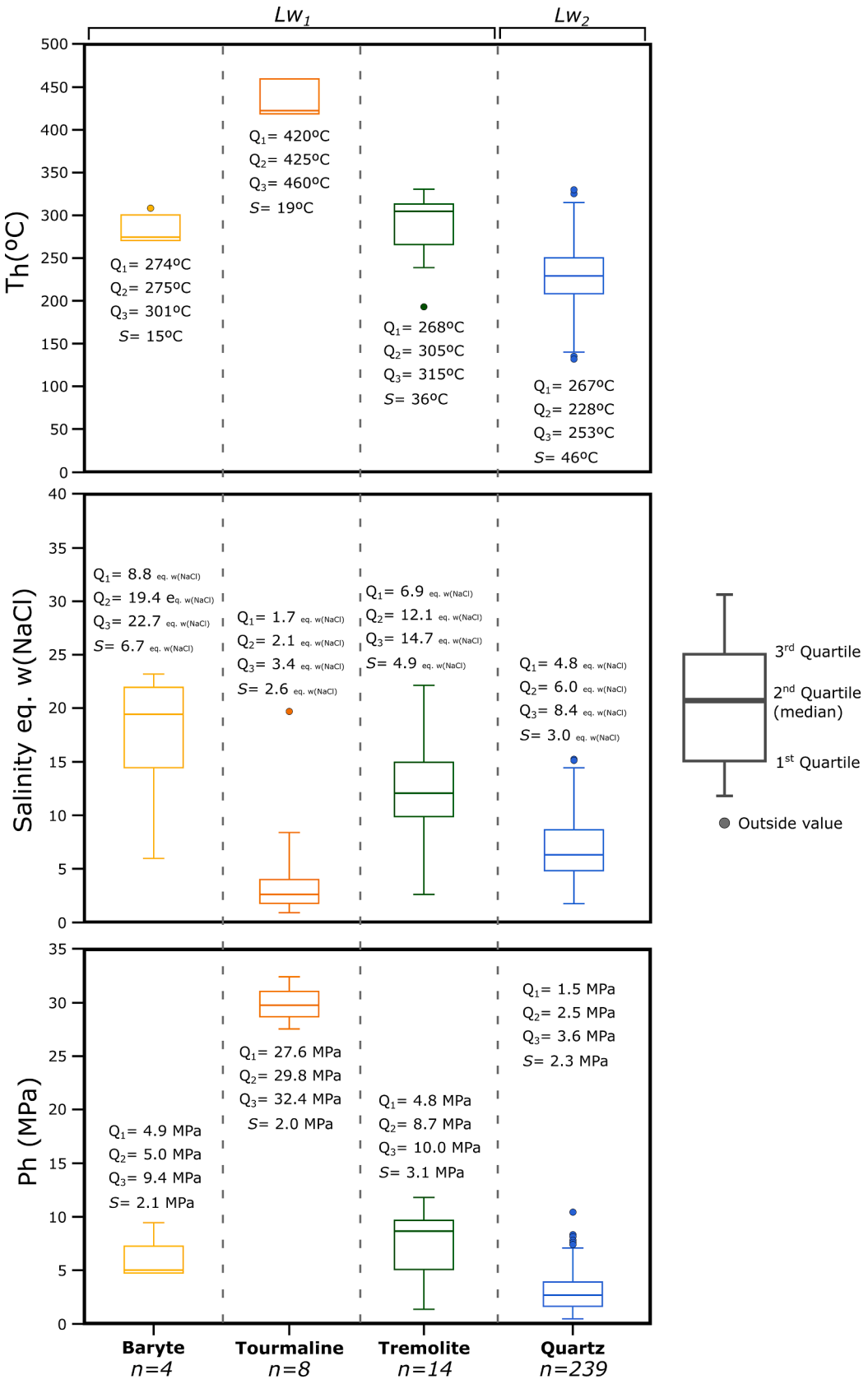

Fig. 13. Boxplot diagrams in which representative P-T-x data from fluid inclusion microthermometry is plotted. 1st quartile, 2nd quartile, 3rd quartile and standard deviation (*S*) values are provided for each diagram. Data is here divided regarding the host-mineral, and the number of fluid inclusions studied in each one is provided by *n*.

First ice melting temperatures (Te) measured in Lw_2 FÍs hosted by quartz, range from −33 °C to −15 °C, with a median of −26 °C. Tm_{ice} ranges from −14.3 °C to −0.1 °C and $Th_{(L+V\rightarrow L)}$ are between 125 °C and 327 °C with a median of 226 °C. Salinities range from 1.7 to 15.3 eq. w (NaCl), with a correspondent eq. w(NaCl) median of 6.5, with pressure estimations between 0.3 MPa and 19.7 MPa (*Md* = 3.1 MPa).

Methane-rich fluid inclusions hosted in quartz (Fig. 12 **h**) exhibited similar behaviors through the cooling runs (up to the −196.6 °C), and although triple point temperature of CH_4 was reached (−182.5 °C) inclusions did not completely freeze. As shown by early studies from Roedder (1984), CH_4-rich fluid inclusions can sustain a metastable behavior through temperatures much lower than the triple point, thus not allowing salinity estimations. Microthermometry of these inclusions revealed phase transitions below the critical temperature of CH_4 (−82.6 °C), with Tm_{CH4} between −143.5 °C and −136.3 °C when homogenizing in the liquid-phase (L_{CH4}) and between −141.0 °C and −136.0 °C when homogenization into the vapor (V_{CH4}) phase occurs. Although the aqueous portion of the CH_4-rich inclusions is particularly small (approx. 5%), Tm_{ice} was limitedly observed in the range of −6.2 °C and −0.9 °C. Pressure at CH_4 homogenization was estimated between 0.35 MPa and 0.54 MPa for L_{CH4} and between 0.41 MPa and 0.55 MPa for V_{CH4} (Table 2).

4.5. Sulfides, gold, and silicate geochemistry

A total of 278 EPMA spot analyses were performed in arsenopyrite (159), pyrite (48), gold (7), tourmaline (13), chlorite (18), and feldspars (23). Sample selection was done after a detailed mineralogical description and SEM-EDS analysis. The microprobe raw results can be consulted in **Supplementary Material B**.

Arsenopyrite composition (Table 3) was acquired both for Apy A and Apy B, with As weight content below the typical stoichiometric composition for arsenopyrite (46 wt%), with a median of 41.25 wt% for the complete arsenopyrite data.

EPMA analysis considered the zoning observed in backscattered electron imagery, revealing Apy A arsenic content varying from 38.14 wt% to 43.06 wt% (*Md* = 41.55 wt%) in crystal cores and from 40.05 wt % to 41.26 wt% (*Md* = 40.44 wt%) at the rims.

Apy B revealed As contents ranging from 40.45 wt% to 41.76 wt% (*Md* = 41.06 wt%) in the crystal cores and between 39.70 wt% and 40.78 wt% (*Md* = 40.03 wt%) in the arsenic-depleted patchy areas (Fig. 8**k**). Although gold was analyzed as a trace element no concentrations above EPMA limits of detection (LOD; 308 ppm) were present. Both types of arsenopyrite displayed suitable values of Fe (<34.3 at. %), for the application of the arsenopyrite geothermometer (Kretschmar and Scott, 1976).

Microprobe analysis of Py A and Py B (Table 3) revealed faint variation in As content, reinforcing their petrographic distinction (Fig. 9). Py A revealed arsenic values mostly below LOD (1734 ppm). Whereas, in Py B, the concentration of As ranges from 0.18 wt% to 0.71 wt% (*Md* = 0.32 wt%). Although none of the above-mentioned pyrite types is considered As-rich, Py B shows a slight arsenic enrichment.

Gold hosted in Apy A from type i mineralization style revealed Au values ranging from 85.56 wt% to 86.29 wt% (Table 4), and Ag values between 13.15 wt% and 13.56 wt%. Low values of Fe were also detected, whereas the remaining analyzed elements are below EPMA LOD (disclosed in Table 4). Arsenopyrite-rich layers from type i mineralization display small gold grains with Au contents of 91.80 wt% and Ag contents of 7.08 wt%. Due to the small gold particle size, only one isolated gold particle was analyzed in these type i mineralized sections.

Table 3
Representative EPMA analysis of arsenopyrite and pyrite crystals from the Type i and Type ii mineralization. The presented values correspond to the median values from several single-spot analysis (n) performed in each arsenopyrite crystal, in wt. % and atom per formula unit (a.p.f.u.). Structural formulae calculated on anionic basis of As + S = 1 for arsenopyrite, and S = 2 for pyrite.

Sample		Apy Type	Minerali-zation Type	S (wt. %)	As (wt. %)	Fe (wt. %)	S (a.p.f.u)	As (a.p.f.u)	Fe (a.p.f.u)	*n**
005–31.3b	Arsenopyrite	Apy A	Type i	23.45	40.91	35.74	1.15	0.86	1.00	8
005–31.3b		Apy A	Type i	23.64	41.25	35.81	1.15	0.86	1.00	5
005–31.3b		Apy A	Type i	23.40	41.21	35.55	1.14	0.86	1.00	9
005–31.3b		Apy A	Type i	23.78	41.50	35.21	1.15	0.86	0.97	1
005–31.3b		Apy A	Type i	23.18	42.07	35.25	1.13	0.87	0.98	1
005–31.3b		Apy A	Type i	23.63	41.67	34.81	1.14	0.86	0.96	1
005–31.3b		Apy A	Type i	23.77	42.00	35.20	1.14	0.86	0.97	1
005–31.3b		Apy A	Type i	23.03	42.56	34.51	1.12	0.88	0.96	10
005–31.3b		Apy A	Type i	23.55	41.91	34.13	1.14	0.87	0.95	9
005–32.4b		Apy A	Type i	23.12	42.72	34.64	1.12	0.88	0.96	10
005–32.4b		Apy A	Type i	23.39	41.64	34.68	1.14	0.87	0.97	1
005–32.4b		Apy A	Type i	23.61	41.05	34.67	1.15	0.85	0.97	6
004–11.1b		Apy A	Type i	23.41	41.85	34.73	1.13	0.87	0.97	20
005–32.4c		Apy A	Type i	23.69	40.96	35.18	1.15	0.85	0.98	12
005–32.4c		Apy A	Type i	23.65	40.24	35.42	1.16	0.84	1.00	3
005–32.4c		Apy A	Type i	23.45	41.56	35.25	1.14	0.86	0.98	6
005–32.4c		Apy A	Type i	23.28	41.32	35.24	1.14	0.86	0.99	8
005–31.3b		Apy Arims	Type i	23.46	40.56	35.88	1.15	0.85	1.01	4
005–31.3b		Apy Arims	Type i	23.46	40.56	35.88	1.15	0.85	1.01	1
007–21.8a		Apy B	Type i	23.68	41.09	35.07	1.15	0.85	0.98	6
007–21.8a		Apy B	Type i	23.71	41.10	35.03	1.15	0.85	0.97	8
007–21.8a		Apy B	Type i	23.60	40.96	34.96	1.15	0.85	0.98	10
007–21.8a		Apy B	Type i	23.60	41.19	35.00	1.15	0.86	0.98	8
007–21.8a		Apy B rims	Type i	24.93	39.98	35.43	1.19	0.81	0.98	3
007–21.8a		Apy B rims	Type i	24.37	40.64	35.39	1.17	0.83	0.97	3
007–21.8a		Apy B rims	Type i	24.38	40.18	35.23	1.17	0.82	0.97	2
005–31.3b	Pyrite	Py A	Type i	53.720	0.24	45.35	2	0.002	0.97	6
007–10.3b		Py B	Type ii	53.76	0.57	45.22	2	0.008	0.97	18
007–10.3b		Py B	Type ii	53.89	0.24	45.48	2	0.004	0.97	15

Representative EPMA analysis of arsenopyrite and pyrite crystals from the different mineralized horizons. The presented values correspond to the median values from several single-spot analysis (***n***) performed in each arsenopyrite crystal. (in wt. %)
n = number of single spot analysis per crystal

Table 4
Representative EPMA analysis of gold particles from the Type i and Type ii mineralization.

Mineralization Type		Type i)				Type ii)		
Mode of occurence		Filling Apy A fractures			Free particles	Filling Py B fractures		
(wt. %)	LOD (ppm)	1	2	3	4	5	6	7
Au	5554	85.5623	86.2867	86.2194	91.8017	80.5427	82.8970	82.1758
Ag	861	13.5587	13.2686	13.1482	7.0838	18.6811	16.8268	17.4702
Fe	498	0.1247	0.1644	b.d.l.	0.1572	0.2442	0.1242	0.116
Cu	360	0.0368	b.d.l.	b.d.l.	b.d.l.	b.d.l.	b.d.l.	b.d.l.
Se	731	b.d.l.	b.d.l.	b.d.l.	b.d.l.	b.d.l.	b.d.l.	b.d.l.
Te	388	b.d.l.	b.d.l.	b.d.l.	b.d.l.	b.d.l.	b.d.l.	b.d.l.
Bi	1463	b.d.l.	b.d.l.	b.d.l.	b.d.l.	b.d.l.	b.d.l.	b.d.l.
Hg	3886	b.d.l.	b.d.l.	b.d.l.	b.d.l.	b.d.l.	b.d.l.	b.d.l.
Total		99.3163	99.8263	99.5365	99.1189	99.6290	99.9311	99.8498
Fineness	–	863	867	868	928	812	831	825

*b.d.l. = below detection limit

Gold filling microfractures in pyrite B from type ii mineralization shows a slightly different composition, with lower Au (between 80.54 wt % and 82.90 wt%) and higher Ag (between 16.83 wt% and 18.68 wt%) concentrations.

EPMA analysis were used to calculate gold fineness (Fisher, 1945), with results ranging from 863 to 868 for gold filling Apy A fractures from type i mineralization and from 812 to 831 for gold in Py B from type ii mineralization. The single free gold particle from type i showed the higher fineness value of 928.

Microprobe analysis was performed in mineral phases found on the host rocks of gold mineralization, as an auxiliary method to characterize the degree of hydrothermal alteration. This study was mostly applied to secondary minerals, namely feldspar from Qz IIb veins, and chlorite accompanying gold-bearing pyrite from to type ii mineralization (sample shown in Fig. 9**b**).

Feldspar characterization was performed using the microprobe analysis (Table 5; **Supplementary Material B**) on samples of Escoural Fm. paragneisses, Carvalhal Fm. basic metavolcanic rocks, and veins crosscutting the Monfurado Fm acid metavolcanis rocks, based on An, Ab and Or percentages applying the classification diagram from Fig. 14**a**. The results show that the paragneiss and basic metavolcanic rocks are mainly composed of orthoclase, whereas the analyzed feldspars from veins that crosscut acid metavolcanic rocks of rhyolite affinity are mainly albite (Ab84%; Table 5).

Chlorites were selected from samples of Qz IIb-plagioclase-pyrite veins that crosscut the acid metavolcanic rocks and are found to be related to type ii mineralization, therefore allowing the comparison between the chlorite geothermometer and the fluid inclusion data (Table 2) from Qz IIb (Fig. 12 **a – d**). The selected samples correspond to trioctahedral chlorites, classified as clinochlore by the Mg – Al^{+} - Fe classification diagram (Fig. 14**b**). The chlorite geothermometer was performed after Cathelineau (1988) using the EPMA data (Table 5; **Supplementary Material B**).

Additionally, tourmaline crystals hosted in Qz IIa quartz crosscutting acid metavolcanic rocks (Fig. 4**d, e**) were selected for microprobe analysis (Table 5; **Supplementary Material B**). The classification diagram using the Na / (Na + Ca) in the X site and Fe / (Fe + Mg) in the Y site (Fig. 14**c**) classify the samples as dravite.

4.6. Sulfur isotopes data ($\delta^{34}S_{CDT}$)

In the type i mineralization, the $\delta^{34}S_{CDT}$ was measured in arsenopyrite, pyrrhotite and pyrite. Apy A has values from 10.1 ‰ to 10.3 ‰ (Table 6), comparable to those found in Apy B, with a $\delta^{34}S_{CDT}$ of 10.6 ‰. Pyrite (Py A) shows signatures from 9.5 and 9.6 ‰ (Table 6), whereas pyrrhotite revealed lighter $\delta^{34}S_{CDT}$ values, from 8.5‰ and 9.7 ‰. In type ii mineralization, the $\delta^{34}S_{CDT}$ of the pyrite (Py B) shows a value of 10.2 ‰.

To compare $\delta^{34}S_{CDT}$ signatures, pyrites from the pre-ore stages were selected for sulfur source differentiation. Pyrites ubiquitously disseminated in the marbles, possibly diagenetic, yield $\delta^{34}S_{CDT}$ signature of 13.7 ‰ heavier than that of ore stage sulfides. The pyrites interpreted as being contemporary of the SEDEX-VMS iron mineralization events display contrasting $\delta^{34}S_{CDT}$ signatures of 3 ‰ (Table 6) lighter than those of the ore-stage.

5. Discussion

5.1. Depositional stages

The Monfurado prospect is not only an interesting and complex case study from the Escoural gold district (Fig. 1**b, d**), as it is also an example of gold deposition that can be compared to worldwide Orogenic Gold deposits. In summary, two main gold mineralization types characterize the deposit: Type i mineralization is parallel to the host rock layering, with gold found in arsenopyrite (Apy A and Apy B) and pyrite (Py A) disseminated in massive sulfide layers (Fig. 8**a-c**) and mostly deposited in microfractures in those minerals (Fig. 8**l, m**). The presence of magnetite substitution by pyrrhotite suggest that fluid-rock interactions might have assisted gold deposition in type i mineralization.

Type ii mineralization occurs in veins parallel to bedding, in which gold is found to be hosted in pyrite (Py B) microfractures, usually accompanied by chlorite and quartz, and found in veins exclusively crosscutting the acid metavolcanic unit. The development of these veins is structurally controlled by late brittle deformation.

The identification of the paragenetic sequence is supported by the petrographic and mineralogical data, and is reinforced by the isotopic and geochemical data, constituting what is here described as the main gold stage (Fig. 11).

Type i mineralization has never been described for the Escoural gold district (Fig. 1**b, d**), whereas type ii shows a mode of occurrence similar to what is found in other deposits of the district (e.g. Casas Novas, Chaminé) where gold mainly occurs in quartz lodes, with chloritization of the host rocks, in arsenopyrite-loellingite-pyrite-gold assemblages associated with native bismuth and bismuthinite (Ribeiro et al., 1993). Such features are consistent to type ii mineralization at the Monfurado prospect, where gold deposition is sometimes accompanied by hedleyite (Fig. 9**k**; Fig. 10**f**)

When inspecting gold fineness (Table 4) it becomes evident that gold from type i shows higher values (863–868) than those from type ii gold (812–831) which reinforces the distinct petrographic criteria.

5.2. Thermal and fluid evolution constraints

Fluid inclusion studies are extremely important in identifying the P-T-V-x conditions of the fluids responsible for gold transport in orogenic gold deposits, as well as in understanding host rock interactions promoted by those fluids, such as sulfidation and carbonation (Palin and Xu,

Table 5
Representative EPMA analysis (wt. %) of chlorite, tourmaline and feldspars. The presented values correspond to the average values from several single-spot analysis (n) performed in each phase. Additionally, standard deviation (σ) values of the analysis are provided in separate columns. For chlorite, the average temperatures are presented according to Chathelineau (1988) empirical geothermometric equation and structural formula was calculated using the WinCcac software from Yavuz et al. (2015), based on 14 oxygens. The structural formula for plagioclase and alkali feldspars was calculated based on 32 oxygens, and tourmaline in the basis of 29 oxygens.

Lithology	Quartz-Chlorite-Pyrite-(Gold) veins hosted in acid metavolcanic rocks						Lithology	Acid metavolcanic rocks				Lithology	Paragneiss – Escoural Fm.		Basic metavolcanic rocks		Quartz – Feldspar – Chlorite veins in acid metavolcanic rocks	
Mineral	Chlorite						Mineral	Tourmaline				Mineral	Feldspars					
	n = 7	σ	n = 9	σ	n = 2	σ		Rim (n = 6)	σ	Core (n = 7)	σ		n = 5	σ	n = 8	σ	n = 10	σ
Element (wt. %)							**Element (wt. %)**					**Element (wt. %)**						
SiO_2	28.9	0.3	28.3	0.6	27.9	0.6	**SiO_2**	37.2	0.21	37.4	0.38	**SiO_2**	63.4	1.20	64.18	0.46	66.77	1.18
TiO_2	0.1	0.0	0.0	0.0	0.0	0.0	**TiO_2**	0.8	0.42	0.5	0.50	**TiO_2**			0.03	0.00		
Al_2O_3	17.6	0.3	17.8	0.7	20.4	0.5	**Al_2O_3**	30.2	0.86	30.6	1.61	**Al_2O_3**	18.7	0.43	18.82	0.22	20.60	0.56
FeO	20.1	0.3	23.0	2.1	17.6	0.4	**FeO**	4.7	0.29	4.9	1.49	**FeO**	0.1	0.00	0.06	0.00	0.07	0.01
MnO	0.2	0.0	0.2	0.0	0.2	0.0	**MgO**	9.1	0.23	8.8	0.28	**CaO**	1.2	1.20	0.02	0.02	0.85	0.37
MgO	18.3	0.4	16.1	1.3	19.7	0.1	**CaO**	0.6	0.25	0.4	0.28	**Na_2O**	0.4	0.16	0.57	0.23	9.71	2.64
CaO	0.1	0.0	0.1	0.0	0.1	0.0	**Na_2O**	2.4	0.09	2.5	0.14	**K_2O**	16.2	0.49	16.17	0.40	1.87	3.88
Na_2O	0.0	0.0	0.0	0.0	0.0	0.0	**Total**	85.0	0.38	85.2	0.49	**BaO**	0.4	0.11	0.45	0.13	1.73	0.00
K_2O	0.0	0.0	0.0	0.0	0.0	0.0						**Total**	99.6	1.07	100.23	0.50	99.99	0.37
Total	85.3	0.9	85.6	0.7	86.1	0.5	**Formula O = 29**											
Formula O = 14							**B**					**Formula O = 32**						
Z								3.0	0.00	3.0								
Si	3.0	0.0	3.0	0.1	2.9	0.1	**Si**	6.1	0.02	6.1		**Si**	11.8	0.07	11.89	0.03	11.77	0.06
Al^{IV}	1.0	0.0	1.0	0.1	1.1	0.1	**Ti**	0.1	0.05	0.1		**Al**	4.1	0.04	4.11	0.04	4.28	0.06
Total (IV)	4.0	0.0	4.0	0.0	4.0	0.0	**Al**	5.8	0.13	5.9		**Fe(ii)**	0.0	0.00	0.01	0.00	0.01	0.00
R							**Fe(ii)**	0.6	0.04	0.7		**Ca**	0.3	0.25	0.00	0.00	0.16	0.07
Al^{VI}	1.2	0.0	1.3	0.1	1.3	0.0	**Mn**	0.0	0.00	0.0		**Na**	0.2	0.06	0.21	0.08	3.30	0.88
Ti	0.0	0.0	0.0	0.0	0.0	0.0	**Mg**	2.2	0.05	2.1		**K**	3.9	0.08	3.82	0.10	0.44	0.92
Cr	0.0	0.0	0.0	0.0	0.0	0.0	**Ca**	0.1	0.04	0.1		**Ba**	0.0	0.01	0.03	0.01	0.13	0.00
Fe^{3+}	0.0	0.0	0.0	0.0	0.0	0.0	**Na**	0.8	0.03	0.8		**Total**	20.1	0.06	20.07	0.02	19.96	0.05
Fe^{2+}	1.8	0.0	2.1	0.2	1.5	0.0	**K**	0.0	0.00	0.0		**An (%)**	2.3	4.50	0.11	0.10	4.11	1.75
Mn	0.0	0.0	0.0	0.0	0.0	0.0	**Total**	18.8	0.04	18.8		**Ab (%)**	3.7	1.46	5.13	2.03	84.66	22.29
Mg	2.9	0.1	2.5	0.2	3.0	0.0						**Or (%)**	94.0	4.62	94.77	1.96	11.22	23.56
Total (VI)	5.9	0.0	5.9	0.0	5.9	0.0												
Total	9.9	0.0	9.9	0.0	9.9	0.0												
Fe/(Fe + Mg)	0.4	0.0	0.4	0.0	0.3	0.0												
Mg + Fe	4.6	0.1	4.6	0.1	4.5	0.0												
Mg/(Mg + Fe)	0.6	0.0	0.6	0.0	0.7	0.0												
Al-chl (%)	18.6	0.4	19.0	0.8	20.7	0.4												
Fe-chl (%)	32.5	0.8	37.5	3.4	28.4	0.0												
Mg-chl (%)	48.9	1.1	43.5	3.4	50.9	0.4												
Geothermometer (°C)*	244.1	5.1	251.3	17.0	290.0	19.0												

***after**Cathelineau, 1988

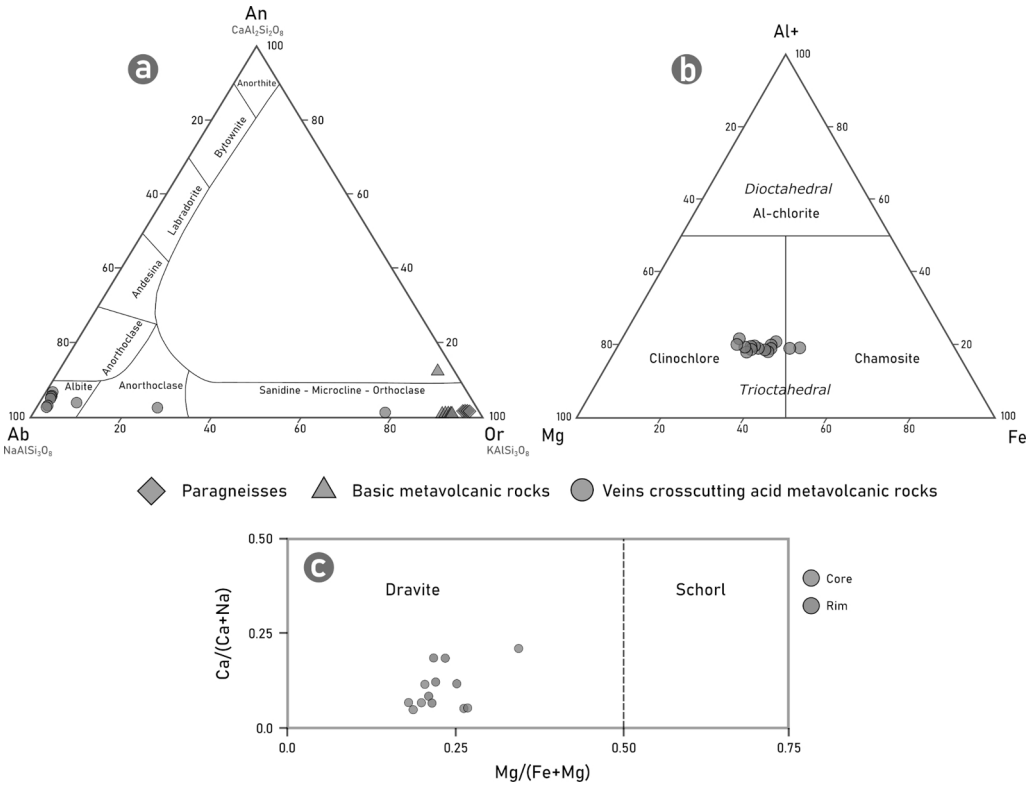

Fig. 14. **(a.)** Feldspar ternary diagram classification with the plots of individual punctual EPMA analysis (provided in Supplementary Material B) and following the nomenclature from Ribbe (1983). **(b.)** Chlorite compositional diagram (after Zane and Weiss, 1998) for the analysed chlorites from the Quartz-Chlorite-Pyrite-(Gold) veins hosted in acid metavolcanic rocks. **(c.)** Tourmaline classification using the ratios Ca / (Ca + Na) vs Mg / (Fe + Mg) (after Galbraith et al., 2009).

Table 6
Sulfur isotope data ($\delta^{34}S$) for the main sulfide phases of the Monfurado deposit.

Sample	Mineralization Type	Mineral	$\delta^{34}S_{CDT(‰)}$
M7-15	Type i	Apy A	10.1
M4-11	Type i	Apy A	10.3
M5-32	Type i	Py A	9.6
M5-31	Type i	Py A	9.5
M5-30	Type i	Po	9.7
M4-11	Type i	Po	9.1
M7-15	Type i	Po	8.5
M7-21	Type i	Apy B	10.6
M7-10	Type ii	Py B	10.2
M7-19	Volcanogenic	Volcanogenic Pyrite	3
M4-14	Diagenetic	Diagenetic Pyrite	13.7

n* = number of EPMA single-spot analysis

2000; Goldfarb et al., 2001; Goldfarb et al., 2005; Hodkiewicz et al., 2009; LaFlamme et al., 2018a; Petrella et al., 2020). Nevertheless, the discussion regarding the fluid evolution of orogenic gold deposits is quite vast and presents weaknesses pointed out in detail by Goldfarb et al. (2005) and Goldfarb and Groves (2015). Ubiquitously, H_2O-CO_2-H_2S($\pm CH_4 \pm N_2$) reduced fluids, with low salinities have been identified in phanerozoic orogenic gold deposits, with temperatures ranging from 250 °C to 400 °C (Bierlein and Crowe, 2000; Goldfarb et al., 2005; Bodnar et al., 2014; Wyman et al., 2016).

The settings in which orogenic gold deposits occur are commonly associated with metasedimentary successions and metabasaltic rocks (Pitcairn et al., 2015) affected by greenschist to amphibolic regional metamorphism, displaying complex tectonic activity in which cyclic shear re-activations leads to successive fracturing and filling during several fluid circulation stages. This tectonism usually results in intricate fluid inclusion assemblages with unclear relation with ore deposition stages. The complexity of these hydrothermal systems often leads to uncertain fluid inclusion data interpretations, with unclear identification of the fluids responsible for ore transport (Groves et al., 2019).

Areas as the Monfurado gold prospect are examples of the above-mentioned fluid complexity, in which interpretation of fluids is highly conditioned by the geodynamic processes that occurred in pre- and post-ore deposition times. Nevertheless, the identification and characterization of the dominant fluids present in this hydrothermal system were possible. Combining the fluid inclusions results with arsenopyrite and chlorite geothermometer estimations allowed to describe the thermal evolution of the system.

Lw_1 inclusions (Fig. 13), especially those studied in tourmaline (dravite; Fig. 14), reflect the presence of fluids with higher temperature (>400 °C) and under higher pressure (>30 MPa), contrasting to Lw_2 inclusions. Most quartz samples in which Lw_2, L_{CH4}/V_{CH4} were identified correspond to late quartz-chlorite-feldspar veins that crosscut acid metavolcanic rocks (Fig. 12**a-d**) in which gold-bearing Py B (Fig. 9**b**) is found. Lw_2 fluid inclusions are ubiquitous in quartz (Qz IIb), and microthermometry revealed relatively low temperatures (*Md* = 230 °C) and low salinities (*Md* = 6.0 % eq. w(NaCl)), which are values compatible with the ones described for other orogenic gold deposits (Fig. 15**a**; Wilkinsson, 2001; Bodnar et al., 2014). Furthermore, Cathelineau (1988) geothermometer was applied to selected chlorite crystals, sampled from the same veins in which Lw_2 inclusions were identified (Fig. 12**a-d**). The chlorite geothermometer indicates temperatures ranging from 229 °C to 309 °C (Table 5; **Supplementary Material B**), with average temperatures of 253 °C, which are compatible to those obtained from Lw_2 inclusions hosted in quartz (Fig. 15**a**).

Arsenopyrite geothermometer was performed using the EPMA data following Kretshmar and Scott (1976) criteria. This methodology was applied assuming a pyrite-arsenopyrite equilibrium (Table 7). Crystal cores of Apy A show an As at. % content from 28.05 at. % to 30.43 at. % corresponding to a temperature range from 239 °C to 372 °C that are overlapped by the obtained temperatures for Apy B, indicating

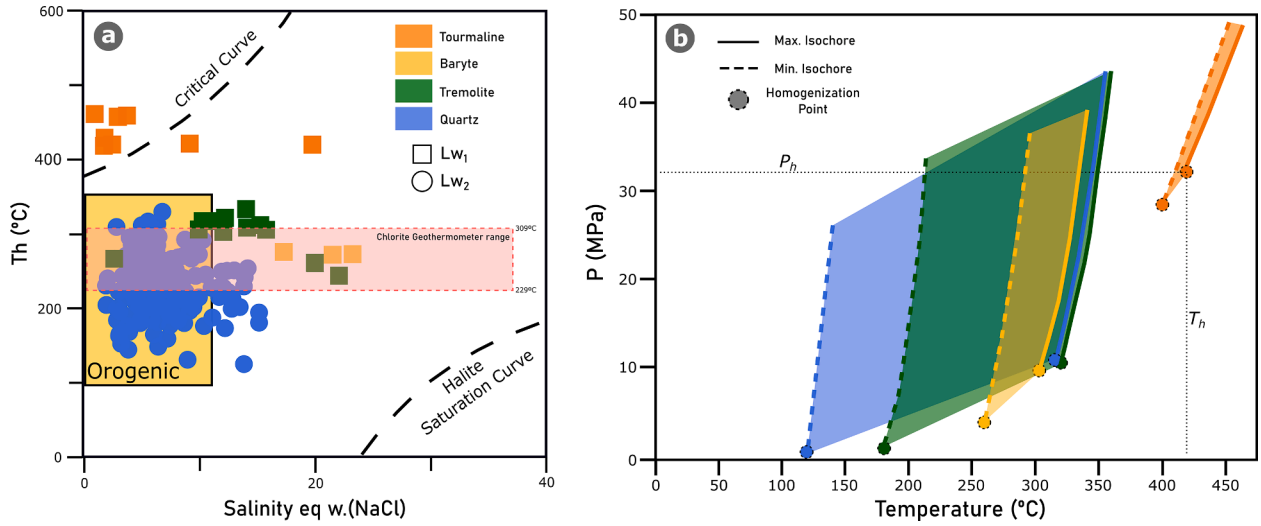

Fig. 15. (a.) Th (°C) vs Salinity (eq. w(NaCl)) plot of the gathered data from fluid inclusion studies. The fields represent the temperature and salinity boundaries for the fluids identified as being associated to those metallogenic environments (after Wilkinson, 2001; Bodnar et al., 2014). The red rectangle marks the range of temperatures obtained for the chlorite geothermometer. **(b.)** P-T reconstruction based on the data collected from the studied fluid inclusions.

Table 7
Summarized statistical data calculated for Apy A and Apy B geothermometer according to Kretschmar and Scott (1976) method.

	Apy A						Apy B					
	Center			Rims			Center			Rims		
	As (at%)	T (°C)	Log a(S_2)	As (at%)	T (°C)	Log a(S_2)	As (at%)	T (°C)	Log a(S_2)	As (at%)	T (°C)	Log a(S_2)
Mean	29.05	305.31	−10.50	28.09	245.63	−12.14	28.68	280.16	−10.79	27.66	217.19	−12.66
Median	29.03	–	–	28.04	–	–	28.61	–	–	27.54	–	–
Std. Dev.	0.52	66.28	−2.64	0.32	32.81	−2.60	0.23	27.96	−1.93	0.37	29.13	−2.35
Min.	28.05	239.03	−13.1	27.58	212.82	−14.7	28.27	252.20	−12.7	27.15	188.06	−15
Max.	30.43	371.59	−7.9	28.73	278.43	−9.5	29.24	308.11	−8.9	28.17	246.32	−10.3
n*	111			9			32			7		

temperatures ranging from 252 °C to 308 °C (Fig. 16) and a mean log a (S_2) = −10.8 for crystal cores.

The slight As depletion found in Apy A crystal rims leads to a range of estimated temperatures from 213 °C to 279 °C (Table 7), suggesting a decrease in temperature from the center towards the rims. Sulfur fugacity also decreases from the cores (log a(S_2) = −10.5) to the rims (log a(S_2) = −12.73; Fig. 16**;** Table 7) as a consequence of the lower arsenic contents.

Apy B also displayed As depleted areas with a patch zonation, to which temperature estimations from 188 °C to 246 °C and mean log a (S_2) = −12.7 (Table 7) were obtained.

Both arsenopyrites from massive sulfide layers (Apy A) and arsenopyrite-rich layers (Apy B) from mineralization type i (Fig. 8**c**) revealed similar arsenopyrite geothermometer (Fig. 16) and sulfur activity estimations which indicates that the processes that led to their formation are very similar. Additionally, the progressively lower P-T registered by fluid inclusions (Fig. 15**b**), is consistent with the chemical composition and correspondent geothermometer estimations attributed to arsenopyrite deposition.

5.3. *Sulfide $\delta^{34}S_{CDT}$ signatures*

Sulfur isotopic composition of sediment-hosted orogenic gold deposits, such as the Escoural gold district, share a similar trend to the seawater sulfate curve throughout geological time (Chang et al., 2008; Groves et al., 2020a,b). Such evidence suggests that sulfur in these deposits is originated from reduced seawater sulfate, fractionated by biogenic or abiogenic processes, which justifies the lighter $\delta^{34}S_{CDT}$ signatures found in sulfides from orogenic gold deposits. Considering this, the gathered $\delta^{34}S_{CDT}$ isotopic signatures of sulfides from the Monfurado ore assemblage suggest a sulfur fractionation of around 10 ‰ to 20 ‰ (coherent with abiogenic fractionation) from the initial seawater sulfate signature (Chang et al., 2008), considering the Neoproterozoic carbonaceous metasediments from Escoural Fm. to be the main sulfur provider to the system. The narrow $\delta^{34}S_{CDT}$ values of the ore assemblage sulfides (Table 6), from 8.5 ‰ to 10.6 ‰ (Fig. 17), indicate that although local paragenetic differences exist (Fig. 11), they share the same sulfur sources and are affected by the same, or at least similar, sulfur fractionation processes (LaFlamme et al., 2018a). Furthermore, the narrow $\delta^{34}S_{CDT}$ variation, although revealing a slight shift in pyrrhotite towards lower $\delta^{34}S_{CDT}$ values, suggest that the variation of fO_2 in the fluid was not significant for major destabilization of $Au(HS)_2^-$, and therefore fluid oxidation is unlikely a major control on Au deposition as suggested by the sulfidation reaction modelling presented by Petrella et al. (2021).

The data obtained by different authors, for other NW Iberian gold districts, both in Portugal and Spain, are displayed in Fig. 17. Similar $\delta^{34}S_{CDT}$ signatures were obtained in the NW Spain Vilalba gold district (Martinez-Abad et al., 2015) and Llamas de Cabrera (Gómez-Fernández et al., 2012), both hosted in Lower Palaeozoic metasediments, with positive values between 2.7 ‰ and 10.9 ‰ and from 8 ‰ to 23.1 ‰, respectively. Gold districts in NW Portugal, hosted in granite rocks, have distinct $\delta^{34}S_{CDT}$ values with contrastingly negative signatures. Examples of these differences are, the Limarinho deposit (−9.2 ‰ – −1.6 ‰; Fuertes-Fuentes et al., 2016) and the Santo António (Penedono) gold deposit (−5.3 ‰ – −3.6 ‰; Neiva et al., 2019).

This study found meaningful $\delta^{34}S_{CDT}$ differences in massive pyrites, possibly related with the SEDEX-VMS ores, and diagenetic pyrites hosted in marbles from the Monfurado Fm., with $\delta^{34}S_{CDT}$ values of 3 ‰ and 13.7

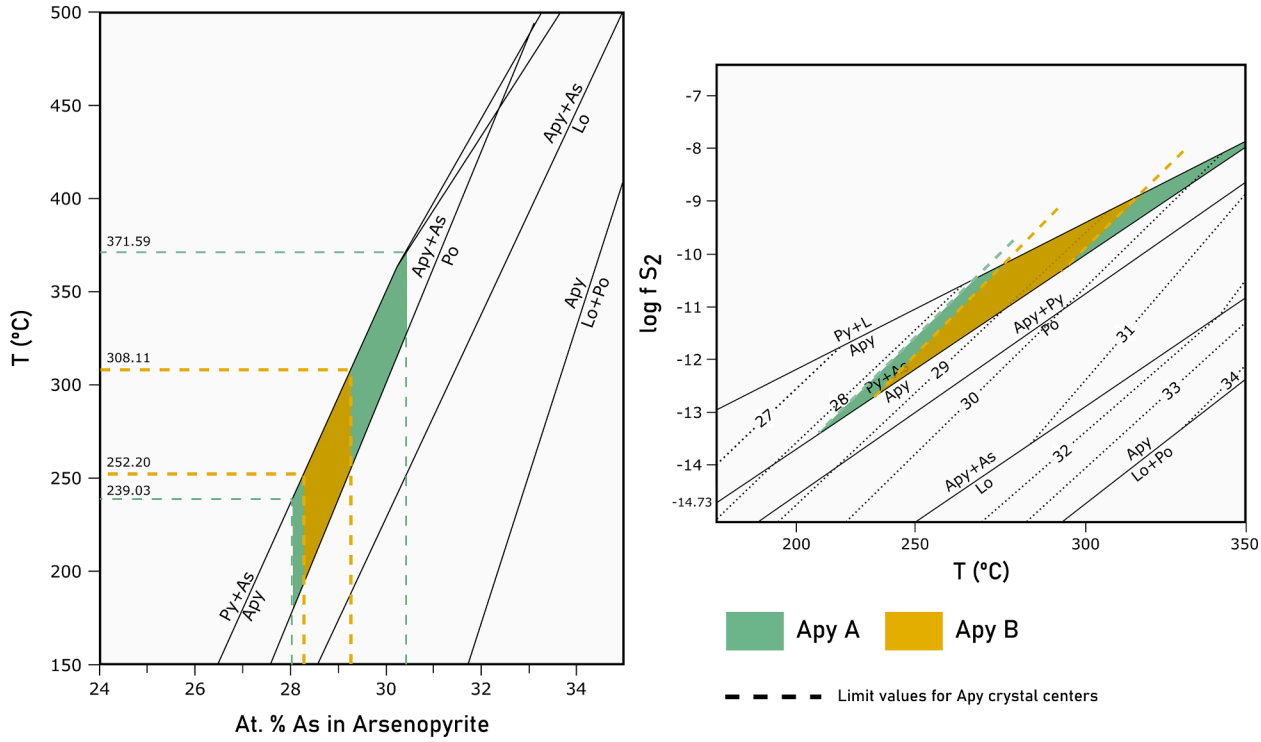

Fig. 16. Arsenopyrite geothermometer (modified by Rajabpour et al., 2017 after Kretschmar and Scott, 1976) in which: the upper diagrams show the projection of T (°C) vs As at. % content of arsenopyrite in the arsenopyrite-pyrite stability field. Single plots are shown both for Apy A and Apy B crystal cores. Log fS_2 vs T(°C) projection for arsenopyrite chemical composition is shown in the right-side diagram.

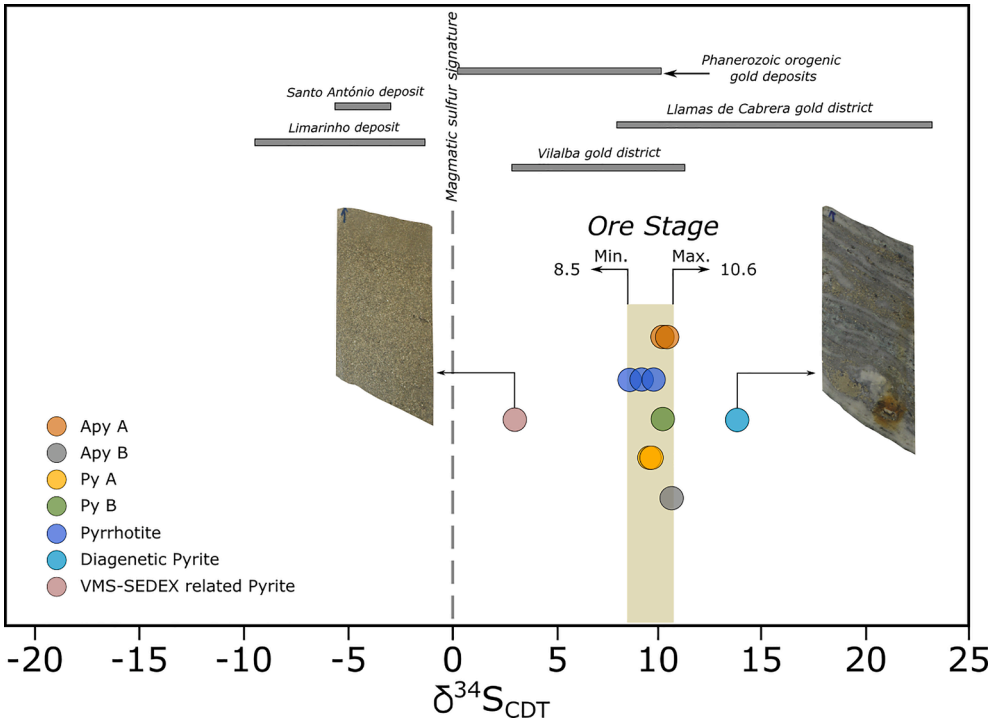

Fig. 17. $\delta^{34}S$ values for the main sulfide phases described for the Monfurado deposit, with the constraining of $\delta^{34}S$ values for the analyzed ore stage sulfides. The grey horizontal bars show the range of $\delta^{34}S$ signatures for worldwide Paleozoic gold deposits (Nesbitt, 1991) and other NW Iberian gold districts. The Santo António deposit (Neiva et al., 2019), Limarinho deposit (Fuertes-Fuentes et al., 2016), Llamas de Cabrera gold district (Gómez-Fernández et al., 2012) and Vilalba gold district (Martinez-Abad et al., 2015) sulfur isotope ranges are displayed for comparison purposes.

‰ respectively (Fig. 17). The difference of these values, when compared to sulfide phases representative of the ore stage, suggest a significant change in the sulfur fractionation throughout the geodynamic evolution of the area.

5.4. Possible gold source and deposition mechanisms

The geodynamic controls of OMZ favored the formation and preservation of several types of mineral deposits, from the ones related to the early rift stage (e.g. Cambrian SEDEX-VMS Montemor-o-Novo iron ore deposits) to the Carboniferous orogenic gold deposits under study. The

compressional and oblique collision developed crustal-scale strike-slip shears, such as the MNSZ, and supra-crustal thermal anomalies that promoted the hydrothermal fluid circulation through dehydration of metal-rich sedimentary basins. Such crustal anisotropies acted as a pathway for metal-enriched metamorphic fluids, and at the same time conditioned the regional tectono-metamorphic regimes that favored the formation of orogenic gold systems (Goldfarb and Groves, 2015; Groves et al., 2020a,b). Combining these geodynamic conditions and considering the gathered data in this research, it is proposed that the Monfurado case study displays a distinct orogenic gold occurrence in SW Iberia, in which a supracrustal metamorphic model (Groves et al., 2019) is the most adequate to explain the genesis of these deposits (Goldfarb and Groves, 2015; Groves and Santosh, 2016). The Escoural gold district displays structural features that correlate it with an orogenic gold model, and the research here presented suggests that local redox destabilization promoted by fluid-rock interactions are the main control on gold deposition related to type i mineralization, which is the main type at the Monfurado gold prospect. In other Escoural gold district deposits, such as the Casas Novas, Chaminé and Braços, gold mineralization is mainly hosted in quartz-arsenopyrite veins associated with brittle deformation and crosscutting the Escoural Fm. (Ribeiro et al., 1993; Inverno, 2001; Lopes et al., 2015; Lopes, 2015), whereas in the Monfurado prospect two types of gold mineralization were identified.

Through this work evidence for metamorphic derived fluids being responsible for Au transport at the Escoural gold district were found. The most likely origin for such fluids is the devolatilization of the Neoproterozoic metasedimentary basement, locally represented by the Escoural Fm., which could also be a key provider of Au and S. Nevertheless, Pitcairn et al. (2015) recently discussed the possibility of trace amounts of Au, at the ppb levels, being remobilized from adjacent metabasaltic host rocks, such as the ones belonging to the Carvalhal Fm, which opens the possibility for other metal providers. For such devolatilization processes to occur several tectonic events can be invoked, such as i) slab break-off (Jesus et al., 2007; Pin et al., 2008; Ribeiro et al., 2010) and correspondent asthenosphere upwelling (Goldfarb and Groves, 2015); ii) radiogenic heat, provided by upper crust lithological pilling (Ribeiro et al., 2007) or even iii) igneous activity associated with the emplacement of magmatic bodies (e.g. Jesus et al., 2007; Moita et al., 2009).

Our research suggests that reduced metamorphic fluids capable of transporting gold in bisulfide complexes ($Au(HS)_2^-$) were enrolled in the process, as indicated by the presence of CH_4-fluids. One new type of gold mineralization (type i) has been identified in the Escoural gold district, in which gold deposition is believed to be triggered by the interaction of the reduced Au transporting fluids and the iron oxide-rich host rocks.

Additionally, the inspection of gold fineness reveals overall values from 812 and 868 which are consistent values for orogenic gold deposits (Morrison et al., 1991). Gold particle fineness is slightly higher for the type i mineralization (863–868) when compared to type ii (812–831) which, as pointed out by other authors (Palyanova, 2008; Petrella et al., 2021), could suggest different ore sources or different ore deposition mechanisms associated to the same mineralizing event. Considering that sulfides from type i and type ii mineralization show very narrow $\delta^{34}S_{CDT}$ signatures it is suggested that the source for sulfur is the same for both types (Fig. 17) and therefore the differences in gold fineness are most likely associated to different ore deposition mechanisms being enrolled with type i and type ii mineralization.

5.4.1. Type i mineralization: Sulfidation processes

For type i Au mineralization, destabilizing conditions for gold deposition were met when the initially reduced fluid interacted with the magnetite-rich host rocks (Monfurado Fm.). Sulfur concentrations in the fluid promoted magnetite sulfidation (Phillips and Groves, 1984; Phillips, 1986; Phillips and Hughes, 1996; Goldfarb et al., 2005), resulting in magnetite replacement by pyrrhotite (Palin and Xu, 2000, Fig. 7**a, b**). Sulfidation reactions are an important alteration associated to gold deposition in orogenic gold deposits (Goldfarb et al., 2005; Petrella et al., 2020; Petrella et al., 2021), and are here interpreted as the main control for the deposition of gold in type i mineralization. The interaction between the reduced fluids transporting $Au(HS)^-_2$ and the iron-rich host rocks from the Monfurado Fm. led to the deposition of pyrrhotite by substitution of magnetite and coeval deposition of sulfides such as arsenopyrite and pyrite. The deposition of these sulfide phases result in the consumption of H_2S from the fluid, thus leading to $Au(HS)^-_2$ destabilization and consequent gold deposition. These processes have been thoroughly discussed by Petrella et al. (2021), which disclose the chemical reactions that result from this fluid-rock interaction.

The fact that most of the gold particles from type i are found in arsenopyrite, suggests that arsenopyrite served as an electrochemical trap for Au (Möller and Kersten, 1994; Dubosq et al., 2018), which raises the question of Au possibly being incorporated in the atomic structure of arsenopyrite during its deposition as thoroughly discussed by Pokrovski et al. (2021). Post deposition metamorphism and deformation could have been an important mechanism in scavenging Au from arsenopyrite and pyrite structure (Fougerouse et al., 2016), leading to its deposition as fracture filling in type i mineralization.

Type i gold mineralization is exclusive to the Monfurado prospect and is part of the main gold mineralization stage, corresponding to gold grades up to 5.3 g/ton through an 8-meter section in one of the drill cores (Fig. 2). The contrasting rheological properties between the acid metavolcanic rocks and the carbonated units of the Monfurado Fm. are responsible for the focusing of type i gold mineralization endowment in these sections. This lithological contact served as an anisotropy for fluid circulation, thus focusing the fluid-rock interactions in the highly permeable iron-rich carbonate units of the Monfurado Fm. whereas, in the acid metavolcanic rocks, brittle-vein emplacement occurred. The result of sulfidation reactions (Fig. 7**a, b**) can be observed throughout the structural pathway in which a laterally consistent sulfide layer (MSL) was generated, which is observable in all core logs. The acid metavolcanics unit served as a low permeability barrier, concentrating fluid circulation at its base, and sulfidation reactions occurred in the lower calcsilicate /carbonate unit (Fig. 2; Fig. 3).

5.4.2. Type ii mineralization: Evidence of reduced fluids

Type ii mineralization is found in quartz-veins (Qz IIb) hosted in acid metavolcanic rocks (Fig. 12**a-d**), contrasting to type i mineralization and thus suggesting that this mineralization type is structurally controlled. The veins bearing this mineralization type are usually sub-horizontal and parallel to the structural pathway, which is interpreted to be focused in the MSL.

Reduced CH_4-rich and H_2O-NaCl fluids were found in quartz from Qz IIb veins, and presumably assisted ore transport (Fig. 9**a;** Fig. 12**h, j**). The presence of CH_4-pure fluid inclusions is particularly interesting and indicates that such fluids are generated under reduced conditions, coherent to the fluids sustaining gold transport in bisulfide complexes (Goldfarb et al., 2005; Phillips and Powell, 2010; Pokrovski et al., 2014, Goldfarb and Groves, 2015). Several geological events are prone to contribute with CH_4 to the ore-forming fluids, from biogenic to abiotic sources (Etiope and Sherwood Lollar, 2013). One commonly considered source of CH_4 is the thermal degradation of organic matter by the reactions between metamorphic-hydrothermal fluids and organic-rich and carbonate-rich rocks, during regional metamorphism (Fan et al., 2004; Etiope and Sherwood Lollar, 2013; Gaboury, 2013; Zhang et al., 2019). Such reactions can be the main CH_4 supplier at the Monfurado gold prospect, owing to the metamorphism and metasomatism that affected the Escoural Fm. metasediments, and the Monfurado Fm. carbonate-rich units. A recent review by Gaboury (2021) addresses the role of organic matter on the formation of orogenic gold deposits since carbonaceous shales, such as the ones from Escoural Fm., are usually attributed as a common gold source. This evidence, together with the $\delta^{34}S_{CDT}$ values from Py B (Table 6; Fig. 17) is consistent with an input of sulfur, and possibly gold, from this Neoproterozoic basement.

In summary, the transport of gold was possibly assisted by CH_4-rich fluids and the partitioning of H_2S into the vapor and non-aqueous phases, such as CH_4, could impose destabilization of $Au(HS)^-_2$ complexes and subsequent gold deposition in type ii mineralization, as suggested by Naden and Shepherd (1989).

Aqueous-carbonic (Lc-w) fluid inclusions were exclusively found in clear-quartz veins cross-cutting the calcsilicate rocks of the Monfurado Fm., indicative that H_2O-CO_2-NaCl fluids have been locally incorporated in the system, and although such fluids are commonly found in orogenic gold deposits, in this case, such association could not be clearly disclosed.

The aqueous fluid inclusions found in Qz IIb veins revealed the presence of low-salinity (*Md* = 6.0 eq. w(NaCl)) and lower-temperature (*Md* = 230 °C) H_2O-NaCl fluids, coherent with the chlorite and arsenopyrite geothermometer (Table 5**;** Fig. 15**a**). Such temperatures indicate probable input of meteoric water to the system (Lw_2; Fig. 15), although linking it to gold deposition was not possible.

6. Conclusions

6.1. Vectoring future mineral exploration

The research approach presented throughout this work proved suitable for providing valuable insights on gold deposition mechanisms at the particularly interesting case study of the Escoural Orogenic gold district, the Monfurado gold prospect (Fig. 1).

The Monfurado gold prospect corresponds to a complex occurrence of gold displaying a unique mineralization style (type i) in which gold deposition was assisted by sulfidation processes that had not been recognized in the Escoural gold district (Fig. 1**a**). The spatial association of this gold prospect with the Santiago do Escoural fault and the precedent iron ores opens the possibility for other gold prospects to be found in the vicinity of this regional geological structures.

Considering the geochemistry, fluid inclusions, and isotopic data, the Neoproterozoic metasediments (i.e. Escoural Fm.) are suggested to be the most likely sulfur and gold supplier to the system. However, the role of the Cambrian volcanogenic iron-rich rocks from the Monfurado Fm. and metabasites from the Carvalhal Fm. (Table 1) as a source of metals is unknown and must not be ruled out considering the present evidence.

Additionally, the identification of gold-bearing sulfide layers - i.e. massive and arsenopyrite-rich - constitutes a valuable exploration vectoring tool for the sector. Understanding the role of the pre-existing iron-oxide domains in the evolution of the system provided insights for new gold deposition mechanisms and supports the possible existence of uncovered gold mineralization associated with the remaining massive iron bodies. Future exploration projects could benefit from this approach, focusing prospects on the contact between the acid metavolcanic and carbonate rocks from the Monfurado Fm., and addressing the relation between gold deposition and the iron-rich host rocks.

Declaration of Competing Interest

The authors declare that they have no known competing financial interests or personal relationships that could have appeared to influence the work reported in this paper.

Acknowledgements

M. Maia acknowledges the financial support of Fundação para a Ciência e Tecnologia (FCT; Portuguese Science and Technology Foundation) through the PhD grant SFRH/BD/145049/2019, as well as the financial support provided by the Society of Economic Geologists Foundation (SEGF) through the Hugh McKinstry Fund and attributted via the Student Research Grant program (2019).

M. Maia, P. Nogueira, and F. Noronha acknowledge the funding provided by the Institute of Earth Sciences (ICT) through the COMPETE 2020 (UIDB/GEO/04683/2020) under the reference POCI-01-0145-FEDER-007690. J. Mirão acknowledges the financial support of the Fundação para a Ciência e Tecnologia (FCT) through the project UID/Multi/04449/2013 and the European Regional Development Fund through the COMPETE 2020 project – POCI-01-0145-FEDER 007649.

This work is a contribution to the project "ZOM-3D Metallogenic Modelling of Ossa-Morena Zone: Valorization of the Alentejo Mineral Resources" (ALT20-03-0145- FEDER-000028), funded by Alentejo 2020 (Regional Operational Program of Alentejo) through the FEDER/FSE/FEEI. The authors would like to thank the pertinent and constructive comments provided by Dr. Reimar Seltmann and an anonymous reviewer, which greatly improved the manuscript.

Appendix A. Supplementary data

Supplementary data to this article can be found online at https://doi.org/10.1016/j.oregeorev.2022.104736.

References

Andrade, A., Silva, J.M., Arruda, C.R., Gameiro, J.C.S., 1949. Minas de Ferro de Montemor-o-Novo. Serviço de Fomento Mineiro 15, 125.

Apalategui, O., Eguiluz, L., Quesada, C., 1990. Ossa-Morena Zone: Structure. In: Martinez, E., Dallmeyer, R.D. (Eds.), Pre-Mesozoic Geology of Iberia. Springer Verlag, pp. 280–291.

Araújo, A., Piçarra de Almeida, J., Borrego, J. Pedro, J. and Oliveira, T., 2013. As regiões central e sul da Zona de Ossa-Morena. in: Dias, R., Araújo, A., Terrinha, P., Kullberg, J.C. (Eds.), Geologia de Portugal, Volume 1, Escolar Editora, pp 509-549.

Araújo, A., Fonseca, P., Munhá, J., Moita, P., Pedro, J., Ribeiro, A., 2005. The Moura Phyllonitic Complex: an accretionary complex related with obduction in the Southern Iberia Variscan Suture. Geodinamica Acta 18 (5), 375–388. https://doi.org/10.3166/ga.18.375-388.

Araújo, A., 1995. Estrutura de uma geotransversal entre Brinches e Mourão (Zona Ossa Morena): Implicações na evolução geodinâmica da margem SW do terreno Autóctone Ibérico. PhD thesis Universidade de Évora, 200 p. (in Portuguese with English abstract).

Azor, A., Dias da Silva, Í., Barreiro, J.G., González-Clavijo, E., Catalán, J.M., Simancas, J. F., Martínez Poyatos, D., Pérez-Cáceres, I.G., Lodeiro, F., Expósito, I., Casas, J.M., Clariana, P., García-Sansegundo, J., Margalef, A., 2019. Deformation and Structure. In: The geology of Iberia: A geodynamic approach. Springer, Cham, pp. 307–348. https://doi.org/10.1007/978-3-030-10519-8_10.

Bakker, R.J., 2003. Package FLUIDS 1. Computer programs for analysis of fluid inclusion data and for modelling bulk fluid properties. Chem. Geol. 194 (1-3), 3–23. https://doi.org/10.1016/S0009-2541(02)00268-1.

Bakker, R.J., 2018. AqSo_NaCl: computer program to calculate p-T-V-x properties in the H_2O-NaCl fluid system applied to fluid inclusion research and pore fluid calculation. Comput. Geosci 115, 122–133. https://doi.org/10.1016/j.cageo.2018.03.003.

Barroso, M., Mateus, A., Figueiras, J., Martins, R., Oliveira, V., 2003. Mineralogy and geochemical characteristics of different superimposed mineralisations at the Enfermarias prospect (Moura, Portugal). VI Congresso Nacional de Geologia, Lisboa (Portugal), Ciências da Terra (UNL), Lisboa, n.° esp. V, CD-ROM, F9-F12.

Bateman, R., Hagemann, S., 2004. Gold mineralization throughout about 45 Ma of Archean orogenesis: protracted flus of gold in the Golden Mile, Yilgarn craton, Western Australia. Mineralium Deposita 39, 536–559. https://doi.org/10.1007/s00126-004-0431-2.

Bierlein, F.P., Crowe, D.E., 2000. Phanerozoic orogenic lode gold deposits. SEG Rev. 13, 103–139.

Bodnar, R.J., Lecumberri-Sanchez, P., Moncada, D., Steele-MacInnis, M., 2014. Fluid inclusions in hydrothermal ore deposits. Treatise Geochem. 13, 119–142.

Bodnar, R.J., Vityk, M.O., 1994. Interpretation of microthermometric data for H2O–NaCl fluid inclusions. In: De Vivo, B., Frezzotti, M.L. (Eds.), Fluid Inclusions in Minerals: Methods and Applications. Sienna, pp. 117–130.

Boiron, M.C., Essarraj, S., Sellier, E., Cathelineau, M., Lespinasse, M., Poty, B., 1992. Identification of fluid inclusions in relation to their host microstructural domains in quartz by cathodoluminescence. Geochim. Cosmochim. Acta 56 (1), 175–185. https://doi.org/10.1016/0016-7037(92)90125-3.

Borrego, J., 2009. Cartografia geológico-estrutural de um sector da Zona de Ossa-Morena (subsector de Estremoz-Barrancos-Ficalho) e sua interpretação tectónica. PhD thesis, 479 p. (in Portuguese with English abstract).

Caldeira, R., Ribeiro, M.L., Moreira, M.E., 2007. Geoquímica das sequências máficas e félsicas entre Alvito, Torrão e Alcáçovas (SW da ZOM). Comunicações Geológicas 94, 5–28.

Carvalho, D., 1971. Observações sobre os jazigos de ferro da área Pedrógão-Orada. I Congresso Hispano – Luso – Americano de Geologia Económica, Madrid – Lisboa, v.1, p. 519-537.

Carvalhosa, A., 1983. Esquema geológico do Maciço de Évora. Comunicações dos Serviços Geológicos de Portugal 69 (2), 201–208.

Carvalhosa, A., Zbyszewski, G., 1994. Carta Geológica de Portugal, Notícia Explicativa da Folha 35-D (Montemor-o-Novo). Instituto Geológico e Mineiro 1 (50), 000.

Castro, A., Pereira, M.F., Rodríguez, C., Fernández, C., de la Rosa, J.D., 2020. Atypical peri-Gondwanan granodiorite–tonalite magmatism from Southern Iberia. Origin of magmas and implications. Lithos 372-373, 105684. https://doi.org/10.1016/j.lithos.2020.105684.

Cathelineau, M., 1988. Cation site occupancy in chlorites and illites as function of temperature. ClayMiner. 23, 471–485. https://doi.org/10.1180/claymin.1988.023.4.13.

Cepedal, A., Fuertes-Fuente, M., Martin-Izard, A., García-Nieto, J., Boiron, M.C., 2013. J. Geochem. Explor. 124, 101–126. https://doi.org/10.1016/j.gexplo.2012.08.010.

Cepedal, A., Fuertes-Fuente, M., Martin-Izard, A., Arias, D., Aragón, D., 2018. The Portas deposit (Lugo, NW of Spain): An orogenic gold deposit related to Paleozoic ironstones. 15th Quadrennial IAGOD International Association on the Genesis of Ore Deposits Symposium.

Chang, Z., Large, R.R., Maslennikov, V., 2008. Sulfur isotopes in sediment-hosted orogenic gold deposits: evidence for an early timing and a seawater sulfur source. Geology 36 (12), 971–974. https://doi.org/10.1130/G25001A.1.

Chichorro, M., Pereira, M.F., Díaz-Azpiroz, M., Williams, I.S., Fernández, C., Pin, C., Silva, J.B., 2008. Cambrian ensialic rift-related magmatism in the Ossa-Morena Zone (Évora–Aracena metamorphic belt, SW Iberian Massif): Sm–Nd isotopes and SHRIMP zircon U-Th–Pb geochronology. Tectonophysics 461 (1-4), 91–113. https://doi.org/10.1016/j.tecto.2008.01.008.

Chichorro, M., 2006. A evolução tectónica da Zona de Cisalhamento de Montemor-o-Novo (Sudoeste da Zona de Ossa-Morena – Área de Santiago do Escoural – Cabrela). PhD Thesis, University of Évora, p.569, (in Portuguese with English abstract).

D'Angelico, A.J., Jenkin, G.R.T., James, D., 2016. Orogenic gold mineralisation in northwest Iberia, Portugal: role of meta-sediment source as a control on location, geochemistry and mineralogy. Appl. Earth Sci. 125 (2), 73–74. https://doi.org/10.1080/03717453.2016.1166604.

Dallmeyer, R.D., Fonseca, P.E., Quesada, C., Ribeiro, A., 1993. 40Ar/39Ar mineral age constraints for the tectonothermal evolution of a Variscan suture in southwest Iberia. Tectonophysics 222 (2), 177–194. https://doi.org/10.1016/0040-1951(93)90048-O.

de Oliveira, D.P.S., Robb, L.J., Inverno, C.M.C., Charlesworth, E.G., 2007. Metallogenesis of the São Martinho and Mosteiros Gold Deposits, Tomar Cordoba Shear Zone, Portugal. Int. Geol. Rev. 49 (10), 907–930. https://doi.org/10.2747/0020-6814.49.10.907.

Dias da Silva, Í., Pereira, M.F., Silva, J.B., Gama, C., 2018. Time-space distribution of silicic plutonism in a gneiss dome of the Iberian Variscan Belt: The Évora Massif (Ossa-Morena Zone, Portugal). Tectonophysics 747, 298–317. https://doi.org/10.1016/j.tecto.2018.10.015.

Dias, R., Ribeiro, A., Romão, J., Coke, C., Moreira, N., 2016. A review of the Arcuate Structures in the Iberian Variscides; Constraints and Genetic Models. Tectonophysics 681, 170–194. https://doi.org/10.1016/j.tecto.2016.04.011.

Dias, G., Simões, P.P., Ferreira, N., Leterrier, J., 2002. Mantle and crustal sources in the genesis of Late-Hercynian granitoids (NW Portugal): geochemical and Sr-Nd isotopic constraints. Gondwana Res. 5 (2), 287–305. https://doi.org/10.1016/S1342-937X(05)70724-3.

Díez-Fernández, R., Fuenlabrada, J.M., Chichorro, M., Pereira, M.F., Sánchez-Martínez, S., Silva, J.B., Arenas, R., 2017. Geochemistry and tectonostratigraphy of the basal allochthonous units of SW Iberia (Évora Massif, Portugal): Keys to the reconstruction of pre-Pangean paleogeography in southern Europe. Lithos 268, 285–301. https://doi.org/10.1016/j.lithos.2016.10.031.

Dubosq, R., Lawley, C.J.M., Rogowitz, A., Schneider, D.A., Jackson, S., 2018. Pyrite deformation and connections to gold mobility: Insight from micro-structural analysis and trace element mapping. Lithos 310–311, 86–104. https://doi.org/10.1016/j.lithos.2018.03.024.

Etiope, G., Sherwood Lollar, B., 2013. Abiotic methane on earth. Rev. Geophys. 51 (2), 276–299. https://doi.org/10.1002/rog.20011.

Fan, H.-R., Xie, Y.-H., Wang, K.-Y., Wilde, S.A., 2004. Methane-rich fluid inclusions in skarn near the giant REE–Nb–Fe deposit at Bayan Obo, Northern China. Ore Geol. Rev. 25 (3-4), 301–309. https://doi.org/10.1016/j.oregeorev.2004.05.001.

Faria, A.F., Chichorro, M., and Amaral, P.K., 1997. Montemor Gold Project, Southern Portugal – Geological Evaluation Report. Moriminas – Soc.Mineira de Montemor Lda., Montemor-o-Novo.

Fisher, N.H., 1945. The fineness of gold, with special reference to the Morobe gold field, New Guinea. Econ. Geol. 40, 449–495. https://doi.org/10.2113/gsecongeo.40.7.449.

Fonseca, P.E., Munhá, J.M., Pedro, J., Rosas, F., Moita, P., Araújo, A., Leal, N., 1999. Variscan ophiolites and high-pressure metamorphism in southern Iberia. Ofioliti 24 (2), 259–268.

Fougerouse, D., Micklethwaite, S., Halfpenny, A., Reddy, S.M., Cliff, J.B., Martin, L.A.J., Kilburn, M., Guagliardo, P., Ulrich, S., 2016. The golden ark: arsenopyrite crystal plasticity and the retention of gold through high strain and metamorphism. Terra Nova 28 (3), 181–187. https://doi.org/10.1111/ter.12206.

Franke, W., 2000. The mid-European segment of the Variscides: tectonostratigraphic units, terrane boundaries and plate tectonic evolution. Geol. Society, London, Spec. Publ. 179 (1), 35–61. https://doi.org/10.1144/GSL.SP.2000.179.01.05.

Franke, W., 2014. Topography of the Variscan orogen in Europe: failed–not collapsed. Int. J. Earth Sci. 103 (5), 1471–1499. https://doi.org/10.1007/s00531-014-1014-9.

Franke, W., Cocks, L.R.M., Torsvik, T.H., 2017. The Palaeozoic Variscan oceans revisited. Gondwana Res. 48, 257–284. https://doi.org/10.1016/j.gr.2017.03.005.

Fuertes-Fuentes, M., Cepedal, A., Lima, A., Dória, A., Ribeiro, M.A., Guedes, A., 2016. The Au-bearing vein system of the Limarinho deposit (northern Portugal): genetic constraints from Bi-chalcogenides and Bi–Pb–Ag sulfosalts, fluid inclusions and stable isotopes. Ore Geol. Rev. 72, 213–231. https://doi.org/10.1016/j.oregeorev.2015.07.009.

Gaboury, D., 2013. Does gold in orogenic deposits come from pyrite in deeply buried carbon-rich sediments? Insight from volatiles in fluid inclusions. Geology 41 (12), 1207–1210. https://doi.org/10.1130/G34788.110.1130/2013340.

Gaboury, D., 2019. Parameters for the formation of orogenic gold deposits. Appl. Earth Sci. 128 (3), 124–133. https://doi.org/10.1080/25726838.2019.1583310.

Gaboury, D., 2021. The Neglected Involvement of Organic Matter in Forming Large and Rich Hydrothermal Orogenic Gold Deposits. Geosciences 11 (8), 344. https://doi.org/10.3390/geosciences11080344.

Galbraith, C.G., Clarke, D.B., Trumbull, R.B., Wiedenbeck, M., 2009. Assessment of Tourmaline Compositions as an Indicator of Emerald Mineralization at the Tsa da Glisza Prospect, Yukon Territory, Canada. Econ. Geol. 104 (5), 713–731. https://doi.org/10.2113/gsecongeo.104.5.713.

Goldfarb, R.J., Groves, D.I., Gardoll, S., 2001. Orogenic gold and geologic time: a global synthesis. Ore Geol. Rev. 18 (1-2), 1–75. https://doi.org/10.1016/S0169-1368(01)00016-6.

Goldfarb, R.J., Baker, T., Dube′, B., Groves, D.I., Hart, C.J.R., Gosselin, P., 2005. Distribution, character and genesis of gold deposits in metamorphic terranes. Econ. Geol. 407–450 https://doi.org/10.5382/AV100.14.

Goldfarb, R.J., Groves, D.I., 2015. Orogenic gold: common or evolving fluid and metal sources through time. Lithos 233, 2–26. https://doi.org/10.1016/j.lithos.2015.07.011.

Gómez-Fernández, F., Vindel, E., Martín-Crespo, T., Sánchez, V., Clavijo, E.G., Matías, R., 2012. The Llamas de Cabrera gold district, a new discovery in the Variscan basement of northwest Spain: a fluid inclusion and stable isotope study. Ore Geol. Rev. 46, 68–82. https://doi.org/10.1016/j.oregeorev.2012.02.001.

Groves, D.I., Santosh, M., 2016. The giant Jiaodong gold province: The key to a unified model for orogenic gold deposits? Geosci. Front. 7 (3), 409–417. https://doi.org/10.1016/j.gsf.2015.08.002.

Groves, D.I., Santosh, M., Deng, J., Wang, Q., Yang, L., Zhang, L., 2020a. A holistic model for the origin of orogenic gold deposits and its implications for exploration. Miner. Deposita 55 (2), 275–292. https://doi.org/10.1007/s00126-019-00877-5.

Groves, D.I., Santosh, M., Zhang, L., 2020b. A scale-integrated exploration model for orogenic gold deposits based on a mineral system approach. Geosci. Front. 11 (3), 719–738. https://doi.org/10.1016/j.gsf.2019.12.007.

Gutiérrez-Marco, J.C., Piçarra, J.M., Meireles, C.A., Cózar, P., García-Bellido, D.C., Pereira, Z., Vaz, N., Pereira, S., Lopes, G., Oliveira, J.T., Quesada, C., Zamora, S., Esteve, J., Colmenar, J., Bernardéz, E., Coronado, I., Lorenzo, S., Sá, A.A., Dias da Silva, Í., González-Clavijo, E., Díez-Montes, A., Gómez-Barreiro, J., 2019. Early Ordovician-Devonian Passive Margin Stage in the Gondwanan Units of the Iberian Massif. In: The geology of Iberia: A geodynamic approach. Springer, Cham, pp. 75–98. https://doi.org/10.1007/978-3-030-10519-8_3.

Hodkiewicz, P.F., Groves, D.I., Davidson, G.J., Weinberg, R.F., Hagemann, S.G., 2009. Influence of structural setting on sulphur isotopes in Archean orogenic gold deposits, Eastern Goldfields Province, Yilgarn Western Australia. Miner. Deposita 44 (2), 129–150. https://doi.org/10.1007/s00126-008-0211-5.

Inverno, C.M.C., 2001. Comparison between orogenic (or mesothermal) gold deposits and intrusion-related gold deposits. Some extrapolation to Portugal. Cadernos Lab. Xeolóxico de Laxe 36, 99–156 in Portuguese with English abstract.

Jesus, A.P., Munhá, J., Mateus, A., Tassinari, C., Nutman, A.P., 2007. The Beja Layered Gabbroic Sequence (Ossa-Morena Zone, Southern Portugal): geochronology and geodynamic implications. Geodin Acta 20 (3), 139–157. https://doi.org/10.3166/ga.20.139-157.

Jesus, A.P., Mateus, A., Munhá, J.M., Tassinari, C.C., dos Santos, T.M.B., Benoit, M., 2016. Evidence for underplating in the genesis of the Variscan synorogenic Beja Layered Gabbroic Sequence (Portugal) and related mesocratic rocks. Tectonophysics 683, 148–171. https://doi.org/10.1016/j.tecto.2016.06.001.

Julivert, M., Fontboté, J.M., Ribeiro, A., Nabais Conde, L.E., 1972. Mapa Tectónico de la Península Ibérica y Baleares. Scale 1:1.000.000, IGME.

Kretschmar, U., Scott, S., 1976. Phase relations involving arsenopyrite in the system Fe-As-S and their application. Can. Mineral. 14 (3), 364–386.

Kroner, U., Stephan, T., Romer, R.L., Roscher, M., 2020. Paleozoic plate kinematics during the Pannotia-Pangea supercontinent cycle. Geol. Society, London, Spec. Publ. 503 https://doi.org/10.1144/SP503-2020-15.

LaFlamme, C., Jamieson, J.W., Fiorentini, M.L., Thébaud, N., Caruso, S., Selvaraja, V., 2018a. Investigating sulfur pathways through the lithosphere by tracing mass independent fractionation of sulfur to the Lady Bountiful orogenic gold deposit, Yilgarn Craton. Gondwana Res. 58, 27–38. https://doi.org/10.1016/j.gr.2018.02.005.

LaFlamme, C., Sugiono, D., Thébaud, N., Caruso, S., Fiorentini, M., Selvaraja, V., Jeon, H., Voute, F., Martin, L., 2018b. Multiple sulfur isotopes monitor fluid evolution of an Archean orogenic gold deposit. Geochim. Cosmochim. Acta 222, 436–446. https://doi.org/10.1016/j.gca.2017.11.003.

Le Maitre, R.W., Streckeisen, A., Zanetin, B., Le Bas, M.J., Bonin, B., Bateman, P., Bellieni, G., Dudek, A., Efremova, S., Keller, J., Lameyre, J., Sabine, P.A., Schmid, R., SØrensen, H., and Wooley, A.R., 2012. Igneous Rocks: A classification and Glossary of Terms, second editions, Cambridge University Press, 2012, 235 pp.

Leal, N., 2001. Estudo petrológico e geoquímico de rochas metamórficas de alta pressão das regiões de Alvito-Viana do Alentejo e de Safira (Zona de Ossa-Morena, Maciço Ibérico). PhD Thesis, Universidade de Lisboa, 402 p. (in Portuguese with English abstract).

Leal, S., Lima, A., Noronha, F., Mortensen, J., Mackenzie, D., 2022. Geological setting of the Bigorne gold deposit, Iberian Variscan belt (Northern Portugal) and Au-Bi-Te mineral assemblages as indicators of the ore-forming conditions. Ore Geol. Rev. 141, 104689 https://doi.org/10.1016/j.oregeorev.2021.104689.

Lindgren, W., 1907. The relation of ore deposition to physical conditions. Econ. Geol. 2, 105–127.

Lindgren, W., 1933. Mineral deposits, 4th ed. McGraw Hill, New York and London, p. 930.
Lopes, L.C.S., Santos, J.F., Sousa, J.C., and Ribeiro, S., 2015. New petrographic, geochemical and isotopic data on the Boa Fé gold prospect (Montemor-o-Novo, Ossa-Morena Zone). Comunicações Geológicas, v.102, Especial I, (in Portuguese with English abstract).
Lopes, L.C.S., 2015. Litogeoquímica na área de concessão da Boa-Fé (COLT Resources). Master Thesis, Univ. Aveiro and Univ. Porto, p.152, (in Portuguese with English abstract).
Lotze, F., 1945. Zur gliederung der Varisziden der Iberischen meseta. Geoteckt. Forsch Berlin 6, 78–92.
MacKenzie, D., Craw, D., Mortensen, J.K., 2019. Orogenic gold deposits in the Variscan belt in northwestern Iberia. In: Proceedings of the 15th SGA Biennal Meeting, 27–30 August 2019, Glasgow, Scotland. SGA, pp. 736–738.
Maia, M., São Pedro, D., Mirão, J., Noronha, F., Nogueira, P., 2019. Fluid constraints for Au deposition at the Monges irondeposit, Ossa-Morena Zone (Montemor-o-Novo, Portugal). In: Proceedings of the 15th SGA Biennal Meeting, 27–30 August 2019, Glasgow, Scotland, vol.1, p. 252–255.
Maia, M., Barrulas, P., Nogueira, P., Mirão, J., Noronha, F., 2022. In situ LA-ICP-MS trace element analysis of magnetite as a vector towards mineral exploration: A comparative case study of Fe-skarn deposits from SW Iberia (Ossa-Morena Zone). Journal of Geochemical Exploration 234, 106941. https://doi.org/10.1016/j.gexplo.2021.106941.
Marshall, B., Gilligan, L.B., 1989. Durchbewegung structure, piercement cusps, and piercement veins in massive sulfide deposits: formation and interpretation. Econ. Geol. 84, 2311–2319. https://doi.org/10.2113/gsecongeo.84.8.2311.
Martinez-Abad, I., Cepedal, A., Arias, D., Martin-Izard, A., 2015. The Vilalba gold district, a new discovery in the Variscan terranes of the NW of Spain: a geologic, fluid inclusion and stable isotope study. Ore Geol. Rev. 66, 344–365. https://doi.org/10.1016/j.oregeorev.2014.10.021.
Martins, R., Mateus, A., Figueiras, J., Barroso, M., Oliveira, V. 2003. Post-metamorphic evolution of the Lower Cambrian section at Enfermarias (Moura, Portugal): its record and metallogenic implications. VI Congresso Nacional de Geologia, Lisboa (Portugal), Ciências da Terra (UNL), Lisboa, n.° esp. V, CD-ROM, B60-B63.
Mateus, A., Araújo, A., Gonçalves, M.A., and Matos, J., 2005. Variscan overthrusting, fluid flow and genesis of magnetite ore-bodies at the Azenhas area (Pedrógão, Ossa-Morena Zona, SE Portugal). Boletín Geológico y Minero, v.116(1), p. 3-22. ISSN 0366-0176.
Mateus, A., Munhá, J., Inverno, C., Matos, J.X., Martins, L., Oliveira, D., Jesus, A., Salgueiro, R., 2013. Mineralizações no sector português da Zona de Ossa-Morena. In: Dias, R., Araújo, A., Terrinha, P., Kullberg, J.C. (Eds.), Geologia de Portugal, vol 1. Escolar Editora, Lisboa, pp. 577–619.
Matos, J., Araújo, A., Mateus, A., 1998. Cartografia de detalhe e controle estrutural das mineralizações na região de Pedrógão-Orada. Geologos 2, 101–104.
Matte, P., 2001. The Variscan collage and orogeny (480–290 Ma) and the tectonic definition of the Armorica microplate: a review. Terra Nova 13 (2), 122–128. https://doi.org/10.1046/j.1365-3121.2001.00327.x.
McLennan, S.M., 1989. Rare Earth elements in sedimentary rocks: influence of provenance and sedimentary processes. In: Lipin, B.R., McKay, G.A. (Eds.), Geochemistry and mineralogy of Rare earth elements. Mineralogical Society of America, Rev. Mineral, v.21, p.169-200.
Melfos, V., Voudouris, P., Serafimovski, T., Tasev, G., 2019. Fluid Inclusions at the Plavica Au-Ag-Cu Telescoped Porphyry-Epithermal System, Former Yugoslavian Republic of Macedonia (FYROM). Geosciences 9, 88. https://doi.org/10.3390/geosciences9020088.
Moita, P., Munhá, J., Fonseca, P.E., Tassinari, C.C.G., Araujo, A., Palácios, T., 2005b. Dating orogenic events in Ossa-Morena Zone. XIV Semana de Geoquímica/ VIII Congresso de Geoquímica dos Países de Língua Portuguesa, 459-461.
Moita, P., Munhá, J., Fonseca, P.E., Pedro, J., Tassinari, C.C.G., Araujo, A., Palácios, T., 2005a. Phase equilibria and geochronology of Ossa Morena eclogites. XIV Semana de Geoquímica/ VIII Congresso de Geoquímica dos Países de Língua Portuguesa 463–466.
Moita, P., Santos, J.F., Pereira, M.F., 2009. Layered granitoids: interaction between continental crust recycling processes and mantle-derived magmatism: examples from the Évora Massif (Ossa–Morena Zone, southwest Iberia, Portugal). Lithos 111 (3-4), 125–141. https://doi.org/10.1016/j.lithos.2009.02.009.
Möller, P., Kersten, G., 1994. Electrochemical accumulation of visible gold on pyrite andcarsenopyrite surfaces. Miner. Deposita 29, 404–413.
Morrison, G.W., Rose, W.J., Jaireth, S., 1991. Geological and geochemical controls on the silver content (fineness) of gold in gold–silver deposits. Ore Geol. Rev. 6 (4), 333–364.
Mortensen, J.K., Martin Izard, A., Cepedal, M.A.H., Fuertes-Fuente, M., Lima, A., Creaser, R., 2014. Gold metallogeny of northwestern Iberia: superimposed orogenic and intrusion related mineralization in an evolving Variscan Orogen. SEG Denver 2014 Conference, Denver, Colorado.
Murphy, J.B., Quesada, C., Gutiérrez-Alonso, G., Johnston, S.T., Weil, A., 2016. Reconciling competing models for the tectono-stratigraphic zonation of the Variscan orogen in Western Europe. Tectonophysics 681, 209–219. https://doi.org/10.1016/j.tecto.2016.01.006.
Naden, J., Shepherd, T.J., 1989. Role of methane and carbon dioxide in gold deposition. Nature 342 (6251), 793–795.
Nance, R.D., Gutiérrez-Alonso, G., Keppie, J.D., Linnemann, U., Murphy, J.B., Quesada, C., Strachan, R.A., Woodcock, N.H., 2010. Evolution of the Rheic ocean. Gondwana Res. 17 (2–3), 194–222. https://doi.org/10.1016/j.gr.2009.08.001.
Nance, R.D., Gutiérrez-Alonso, G., Keppie, J.D., Linnemann, U., Murphy, J.B., Quesada, C., Strachan, R.A., Woodcock, N.H., 2012. A brief history of the Rheic Ocean. Geosci. Front. 3 (2), 125–135. https://doi.org/10.1016/j.gsf.2011.11.008.
Neiva, A.M., Moura, A., Gomes, C.A.L., Pereira, M.F., Corfu, F., 2019. The granite-hosted Variscan gold deposit from Santo António mine in the Iberian Massif (Penedono, NW Portugal): constraints from mineral chemistry, fluid inclusions, sulfur and noble gases isotopes. J. Iber. Geol. 45 (3), 443–469. https://doi.org/10.1007/s41513-019-00103-1.
Nesbitt, B.E., 1991. Phanerozoic gold deposits in tectonically active continental margins. In: Foster, R.P. (Ed.), Gold metallogeny and exploration: London. Blackie, pp. 63–103.
Noronha, F., Cathelineau, M., Boiron, M.C., Banks, D.A., Dória, A., Ribeiro, M.A., Nogueira, P., Guedes, A., 2000. A three stage fluid flow model for Variscan gold metallogenesis in northern Portugal. J. Geol. Explor. 71 (2), 209–224. https://doi.org/10.1016/S0375-6742(00)00153-9.
Oliveira, V.M.J., 1986. Prospeção de minérios metálicos a Sul do Tejo. Geociências – Aveiro 1, 15–22.
Oliveira, J.T., Oliveira, V., Piçarra, J.M., 1991. Traços gerais da evolução tectono-estratigráfica da Zona de Ossa Morena, em Portugal: síntese crítica do estado actual dos conhecimentos. Comum. Serv. Geol, Port. 77, 3–26.
Palyanova, G., 2008. Physicochemical modeling of the coupled behavior of gold and silver in hydrothermal processes: gold fineness, Au/Ag ratios and their possible implications. Chem. Geol. 255, 399–413. https://doi.org/10.1016/j.chemgeo.2008.07.010.
Palin, J.M., Xu, Y., 2000. Gilt by association? Origins of pyritic gold ores in the Victory mesothermal gold deposit, Western Australia. Econ. Geol. 95, 1627–1634. https://doi.org/10.2113/gsecongeo.95.8.1627.
Palme, H., and ÓNeill, HStC., 2014. Cosmochemical Estimates of Mantle Composition. In: Holland, H.D. & Turekian K.K. (Eds) Treatise on geochemistry. Vol. 15: Analytical geochemistry/inorganic instrument analysis. Elsevier, Oxford, p. 1-39. doi:10.1016/B978-0-08-095975-7.00201-1.
Pearce, J.A., Norry, M.J., 1979. Petrogenetic implications of Ti, Zr, Y, and Nb variations in volcanic rocks. Contrib. Mineral. Petrol. 69 (1), 33–47. https://doi.org/10.1007/BF00375192.
Pearce, J.A., Harris, N.B.W., Tindle, A.G., 1984. Trace element discrimination diagrams for the tectonic interpretation of granitic rocks. J. Petrol. 25 (4), 956–983. https://doi.org/10.1093/petrology/25.4.956.
Pedro, J., Araújo, A., Fonseca, P.E., Tassinari, C., Ribeiro, A., 2010. Geochemistry and U-Pb zircon age of the internal Ossa-Morena Zone ophiolite sequences: a remnant of Rheic ocean in SW Iberia. Ofioliti 35 (2), 117–130.
Pedro, J., 1996 Estudo do metamorfismo de alta pressão na área de Safira (Montemor-o-Novo) Zona de Ossa-Morena. MSc. Thesis, Universidade de Lisboa, 69p. (in Portuguese with English abstract).
Pedro, J., 2004. Estudo geológico e geoquímico das sequências ofiolìticas da zona de Ossa-Morena (Portugal). PhD Thesis, Universidade de Lisboa, 225p. (in Portuguese with English abstract).
Pereira, M.F., Chichorro, M., Linnemann, U., Eguiluz, L., Silva, J.B., 2006. Inherited arc signature in Ediacaran and Early Cambrian basins of the Ossa-Morena zone (Iberian Massif, Portugal): paleogeographic link with European and North African Cadomian correlatives. Precambrian Res. 144 (3–4), 297–315. https://doi.org/10.1016/j.precamres.2005.11.011.
Pereira, M.F., Chichorro, M., Williams, I.S., Silva, J.B., 2008. Zircon U-Pb geochronology of paragneisses and biotite granites from the SW Iberian Massif (Portugal): evidence for a palaeogeographical link between the Ossa-Morena Ediacaran basins and the West African craton. Geol. Society, London, Spec. Publ. 297 (1), 385–408. https://doi.org/10.1144/sp297.18.
Pereira, M.F., Chichorro, M., Moita, P., Santos, J.F., Solá, A.M.R., Williams, I.S., Silva, J. B., Armstrong, R.A., 2015. The multistage crystallization of zircon in calc-alkaline granitoids: U-Pb age constraints on the timing of Variscan tectonic activity in SW Iberia. Int. J. Earth Sci. 104 (5), 1167–1183.
Pereira, M. F., Silva, J. B., Chichorro, M., Moita, P., Santos, J. F., Apraiz, A., and Ribeiro, C., 2007. Crustal growth and deformational processes in the northern Gondwana margin: Constraints from the Évora Massif (Ossa-Morena zone, southwest Iberia, Portugal). Special Paper 423: The Evolution of the Rheic Ocean: From Avalonian-Cadomian Active Margin to Alleghenian-Variscan Collision, 333–358. doi:10.1130/2007.2423(16).
Pereira, M.F., Solá, A.R., Chichorro, M., Lopes, L., Gerdes, A., and Silva, J.B., 2012. North-Gondwana assembly, break up and paleogeography: U–Pb isotope evidence from detrital and igneous zircons of Ediacaran and Cambrian rocks of SW Iberia. Gondwana Res., 22(3-4), 866-881. doi:1016/j.gr.2012.02.010.
Pereira, M.F., Silva, J.B., Chichorro, M., 2003. Internal Structure of the Évora High-grade Terrains and the Montemor-o-Novo Shear Zone (Ossa-Morena Zone, Portugal). Geogaceta 33, 79–82.
Pereira, M.F., Gutíerrez-Alonso, G., Murphy, J.B., Drost, K., Gama, C., Silva, J.B., 2017. Birth and demise of the Rheic Ocean magmatic arc(s): combined U-Pb and Hf isotope analyses in detrital zircon from SW Iberia siliciclastic strata. Lithos 278, 383–399. https://doi.org/10.1016/j.lithos.2017.02.009.
Peterson, E.C., Mavrogenes, J.A., 2014. Linking high-grade gold mineralization to earthquake-induced fault-valve processes in the Porgera gold deposit, Papua New Guinea. Geol. 42 (5), 383–386. https://doi.org/10.1130/G35286.110.1130/2014143.
Petrella, L., Thébaud, N., Laflamme, C., Martin, L., Occhipinti, S., Bigelow, J., 2020. In-situ sulfur isotopes analysis as an exploration tool for orogenic gold mineralization in the Granites-Tanami Gold Province, Australia: learnings from the Callie deposit. J. Geochem. Explor. 214, 106542. https://doi.org/10.1016/j.gexplo.2020.106542.

Petrella, L., Thébaud, N., Evans, K., LaFlamme, C., Occhipinti, S., 2021. The role of competitive fluid-rock interaction processes in the formation of high-grade gold deposits. Geochim. Cosmochim. Acta 310, 38–54. https://doi.org/10.1016/j.gca.2021.08.024.

Phillips, G.N., 1986. Geology and alteration in the Golden Mile, Kalgoorlie. Econ. Geol. 81, 779–808. https://doi.org/10.2113/gsecongeo.81.4.779.

Phillips, G.N., Groves, D.I., 1984. Fluid access and fluid-wall rock interaction in the genesis of the Archaean gold-quartz vein deposit at Hunt mine, Kambalda, Western Australia. In: Foster, R.P. (Ed.), Gold '82—the geology, geochemistry and genesis of gold deposits: Rotterdam. Balkema, pp. 389–416.

Phillips, G.N., Hughes, M.J., 1996. The geology and gold deposits of the Victorian gold province. Ore Geol. Rev. 11 (5), 255–302. https://doi.org/10.1016/S0169-1368(96)00006-6.

Phillips, G.N., Powell, R., 2010. Formation of gold deposits: a metamorphic devolatilization model. J. Metamorph. Geol. 28 (6), 689–718. https://doi.org/10.1111/j.1525-1314.2010.00887.x.

Piçarra, J.M., 2000. Estudo estratigráfico do sector de Estremoz-Barrancos, Zona de Ossa Morena, Portugal. Volume 1: Litoestratigrafia do intervalo Câmbrico médio? - Devónico inferior. PhD Thesis, Universidade de Évora, p. 95. (in Portuguese with English abstract).

Pin, C., Fonseca, P.E., Paquette, J.-L., Castro, P., Matte, P., 2008. The ca. 350 Ma Beja Igneous Complex: a record of transcurrent slab break-off in the Southern Iberia Variscan Belt? Tectonophysics 461, 356–377. https://doi.org/10.1016/j.tecto.2008.06.001.

Pitcairn, I.K., Craw, D., Teagle, D.A.H., 2015. Metabasalts as sources of metals in orogenic gold deposits. Miner. Deposita 50 (3), 373–390. https://doi.org/10.1007/s00126-014-0547-y.

Pokrovski, G.S., Akinfiev, N.N., Borisova, A.Y., Zotov, A.V., Kouzmanov, K., 2014. Gold speciation and transport in geological fluids: insights from experiments and physical-chemical modelling. Geol. Society, London, Spec. Publ. 402 (1), 9–70. https://doi.org/10.1144/SP402.4.

Pokrovski, G.S., Escoda, C., Blanchard, M., Testemale, D., Hazemann, J.-L., Gouy, S., Kokh, M.A., Boirn, M.-C., de Parseval, F., Aigouy, T., Menjot, L.L., de Parseval, P., Proux, O., Rovezzi, M., Béziat, D., Salvi, S., Kouzmanov, K., Barstch, T., Pöttgen, R., Doert, T., 2021. An arsenic-driven pump for invisible gold in hydrothermal systems. Geochem. Perspect. Lett. 17, 39–44. https://doi.org/10.7185/geochemlet.2112.

Quesada, C., Fonseca, P.E., Munhá, J., Oliveira, J.T., Ribeiro, A., 1994. The Beja-Acebuches Ophiolite (Southern Iberia Variscan fold belt): geological characterization and geodynamic significance. Boletín Geológico y Minero 105 (1), 3–49.

Quesada, C., Braid, J.A., Fernandes, P., Ferreira, P., Jorge, R.S., Matos, J.X., Murphy, J. B., Oliveira, J.T., Pedro, J., Pereira, Z., 2019. SW Iberia Variscan Suture Zone: Oceanic Affinity Units. In: The Geology of Iberia: A Geodynamic Approach. Springer, Cham, pp. 131–171. https://doi.org/10.1007/978-3-030-10519-8_5.

Rajabpour, S., Behzadi, M., Jiang, S.-Y., Rasa, I., Lehmann, B., Ma, Y., 2017. Sulfide chemistry and sulfur isotope characteristics of the Cenozoic volcanic-hosted Kuh-Pang copper deposit, Saveh county, northwestern central Iran. Ore Geol. Rev. 86, 563–583. https://doi.org/10.1016/j.oregeorev.2017.03.001.

Ribbe, P. H., 1983. Feldspar mineralogy. Mineralogical Society of America. 2nd. Ed., pp 362.

Ribeiro, M.L., Castro, A., Almeida, A., Menéndez, L.G., Jesus, A., Lains, J.A., Carrilho Lopes, J., Martins, H.C.B., Mata, J., Mateus, A., Moita, P., Neiva, A., Ribeira, M.A., Santos, J.F., Solá, A.R., 2019. Variscan Magmatism. In: The Geology of Iberia: A Geodynamic Approach. Springer, Cham, pp. 497–526. https://doi.org/10.1007/978-3-030-10519-8_13.

Ribeiro, A., Dias, R., BrandÃo Silva, J., 1995. Genesis of the Ibero-Armorican arc. Geodinamica Acta 8 (4), 173–184.

Ribeiro, A., Munhá, J., Dias, R., Mateus, A., Pereira, E., Ribeiro, L., Fonseca, P., Araújo, A., Oliveira, O., Romão, J., Chaminé, H., Coke, C., and Pedro, J.C., 2007. Geodynamic evolution of the SW Europe Variscides. Tectonophysics, v.26, TC6009. doi:10.1029/2006TC002058.

Ribeiro, C., Mateus, A., Barriga, F., 1993. Gold mineralization of the Escoural area (Montemor, Évora, Portugal): a progress report. Comun. XII Reun. Geol. Oeste Penins. 1, 215–226.

Ribeiro, A., Munhá, J., Fonseca, P.E., Araújo, A., Pedro, J.C., Mateus, A., Tassinari, C., Machado, G., Jesus, A., 2010. Variscan ophiolite belts in the Ossa-Morena Zone (Southwest Iberia): Geological characterization and geodynamic significance. Gondwana Res. 17 (2-3), 408–421. https://doi.org/10.1016/j.gr.2009.09.005.

Robardet, M., Gutiérrez-Marco, J.C., 2004. The Ordovician, Silurian and Devonian sedimentar rocks of the Ossa-Morena Zone (SW Iberian Peninsula, Spain). J. Iber. Geol. 30, 73–92. https://doi.org/10.1016/j.gexplo.2018.02.011.

Rodríguez-Terente, L.M., Martin-Izard, A., Arias, D., Fuertes-Fuente, M., Cepedal, A., 2018. The Salave Mine, a Variscan intrusion-related gold deposit (IRGD) in the NW of Spain: Geological context, hydrothermal alterations and ore features. J. Geoch. Explor. 188, 364–389.

Roedder, E., 1984. Fluid inclusions, Rev. Mineral., Ribbe, P.H.,Ed., Mineralogical Society of America, vol. 12.

Rosas, F.M., Marques, F.O., Ballèvre, M., Tassinari, C., 2008. Geodynamic evolution of the SW Variscides: orogenic collapse shown by new tectonometamorphic and isotopic data from western Ossa-Morena Zone, SW Iberia. Tectonics 27 (6), n/a–n/a. https://doi.org/10.1029/2008TC002333.

Rubio Pascual, F.J.R., Matas, J., Parra, L.M.M., 2013. High-pressure metamorphism in the Early Variscan subduction complex of the SW Iberian Massif. Tectonophysics 592, 187–199. https://doi.org/10.1016/j.tecto.2013.02.022.

Salgueiro, R., Mateus, A., Inverno, C., 2010a. Caracterização e génese do skarn ferrífero de Orada (Zona de Ossa-Morena). E-Terra 20 (3).

Salgueiro, R., Inverno, C., Mateus, A., 2010b. Main characteristics and genesis of the Vale de Pães skarn (Cuba-Vidigueira, Ossa Morena Zone, Portugal). Estudios Geológicos 66 (1), 65–74. https://doi.org/10.3989/egeol.40150.101.

Salgueiro, R., 2011. Caracterização e génese das mineralizações de magnetite – sulfuretos em Monges (Santiago do Escoural, Montemor-o-Novo) e ensaio comparativo com as suas congéneres em Orada-Vale de Pães (Serpa-Vidigueira). PhD Thesis, Univ. Lisboa, 524 p., (in Portuguese with English abstract).

Sánchez-García, T., Bellido, F., Quesada, C., 2003. Geodynamic setting and geochemical signatures of Cambrian-Ordovician rift-related igneous rocks (Ossa-Morena Zone, SW Iberia). Tectonophysics 365 (1-4), 233–255. https://doi.org/10.1016/S0040-1951(03)00024-6.

Sánchez-Garcia, T., Bellido, F., Pereira, M.F., Chichorro, M., Quesada, C., Pin, C., Silva, J. B., 2010. Rift-related volcanism predating the birth of the Rheic Ocean (Ossa-Morena zone, SW Iberia). Gondwana Res. 17 (2), 392–407. https://doi.org/10.1016/j.gr.2009.10.005.

Sánchez-García, T., Quesada, C., Bellido, F., Dunning, G.R., Tánago, J.G., 2008. Two-step magma flooding of the upper crust during rifting: the Early Paleozoic of the Ossa Morena Zone (SW Iberia). Tectonophysics 461 (1–4), 72–90. https://doi.org/10.1016/j.tecto.2008.03.006.

Sánchez-García, T., Pereira, M.F., Bellido, F., Chichorro, M., Silva, J.B., Valverde-Vaquero, P., Pin, C., Solá, A.R., 2014. Early Cambrian granitoids of North Gondwana margin in the transition from a convergent setting to intra-continental rifting (Ossa-Morena Zone, SW Iberia). Int. J. Earth Sci. 103 (5), 1203–1218. https://doi.org/10.1007/s00531-013-0939-8.

Sánchez-García, T., Chichorro, M., Solá, A.R., Álvaro, J.J., Díez-Montes, A., Bellido, F., Ribeiro, M.L., Quesada, C., Lopes, J.C., Dias da Silva, Í., González-Clavijo, E., Gómez Barreiro, J., López-Carmona, A., 2019. The Cambrian-Early Ordovician Rift Stage in the Gondwanan Units of the Iberian Massif. In: Quesada, C., Oliveira, J.T. (Eds.), The Geology of Iberia: A Geodynamic Approach. The Variscan Cycle. Springer Nature, Switzerland, pp. 27–74. https://doi.org/10.1007/978-3-030-10519-8.

Serviço de Fomento Mineiro, 1977, 1:5 000 Geologic map of the Escoural-Monges region.

Shervais, J.W., 1982. Ti-V plots and the petrogenesis of modern and ophiolitic lavas. Earth Planet. Sci. Lett. 59 (1), 101–118. https://doi.org/10.1016/0012-821X(82)90120-0.

Sibson, R.H., Moore, J.M.M., Rankin, A.H., 1975. Seismic pumping—a hydrothermal fluid transport mechanism. J. Geol. Society 131 (6), 653–659.

Simancas, J.F., 2019. Variscan Cycle. In: Quesada. C., Oliveira, J.T. (Eds.), The Geology of Iberia: a geodynamic approach. Vol.2: The Variscan Cycle. Springer (Berlin), Regional Geology Series, pp 1-25. doi:10.1007/978-3-030-10519-8_1.

Thiery, R., Vidal, J., Dubessy, J., 1994. Phase equilibria modelling applied to fluid inclusions: Liquid-vapour equilibria and calculation of the molar volume in the CO2-CH4-N2 system. Geoch. Cosm. Acta 58 (3), 1073–1082. https://doi.org/10.1016/0016-7037(94)90573-8.

Tornos, F., Inverno, C.M.C., Casquet, C., Mateus, A., Ortiz, G., Oliveira, V., 2004. The Metallogenic evolution of the Ossa-Morena Zone. J. Iber. Geol. 30, 143–181.

Uemoto, T., Ridley, J., Mikucki, E., Groves, D.I., Kusakabe, M., 2002. Fluid chemical evolution as a factor in controlling the distribution of gold at the Archean Golden Crown lode gold deposit, Murchison province, Western Australia. Econ. Geol. 97 (6), 1227–1248. https://doi.org/10.2113/gsecongeo.97.6.1227.

Vallance, J., Cathelineau, M., Boiron, M.C., Fourcade, S., Shepherd, T.J., Naden, J., 2003. Fluid–rock interactions and the role of late Hercynian aplite intrusion in the genesis of the Castromil gold deposit, northern Portugal. Chem. Geol. 194 (1–3), 201–224. https://doi.org/10.1016/S0009-2541(02)00278-4.

Valle Aguado, B., Azevedo, M.R., Schaltegger, U., Martínez Catalán, J.R., Nolan, J., 2005. U-Pb zircon and monazite geochronology of Variscan magmatism related to syn-convergence extension in Central Northern Portugal. Lithos 82 (1-2), 169–184. https://doi.org/10.1016/j.lithos.2004.12.012.

Voisey, C.R., Willis, D., Tomkins, A.G., Wilson, C.J.L., Micklethwaite, S., Salvemini, F., Bougoure, J., Rickard, W.D.A., 2020. Aseismic refinement of orogenic gold systems. Econ. Geol. 115, 33–50. https://doi.org/10.5382/econgeo.4692.

Whitney, D.L., Evans, B.W., 2010. Abbreviations for names of rock-forming minerals. Amer. Miner. 95 (1), 185–187. https://doi.org/10.2138/am.2010.3371.

Wilkinson, J.J., 2001. Fluid inclusions in hydrothermal ore deposits. Lithos 55 (1-4), 229–272. https://doi.org/10.1016/S0024-4937(00)00047-5.

Wyman, D.A., Cassidy, K.F., Hollings, P., 2016. Orogenic gold and the mineral systems approach: resolving fact, fiction and fantasy. Ore Geol. Rev. 78, 322–335. https://doi.org/10.1016/j.oregeorev.2016.04.006.

Yavuz, F., Kumral, M., Karakaya, N., Karakaya, M.Ç., Yildirim, D.K., 2015. A Windows program for chlorite calculation and classification. Comput. Geosci. 81, 101–113. https://doi.org/10.1016/j.cageo.2015.04.01.

Zane, A., Weiss, Z., 1998. Aprocedure for classifying rock-forming chlorites based on microprobe dataUna procedura per la classificazione delle cloriti sulla base di dati microchimici. Rend. Lincei Sci. Fis. Nat. Ser. 9 (1), 51–56.

Zhang, W., Williams-Jones, A.E., Leng, C.-B., Zhang, X.-C., Chen, W.T., Qin, C.-J., Su, W.-C., Yan, J.-H., 2019. The origin of CH4-rich fluids in reduced porphyry–skarn Cu–Mo–Au systems. Ore Geol. Rev. 114, 103135. https://doi.org/10.1016/j.oregeorev.2019.103135.